

THERMAL-MECHANICAL ANALYSIS OF TARGETS FOR HIGH VOLUME
PRODUCTION OF MOLYBDENUM-99 USING LOW-ENRICHED URANIUM

A Thesis

presented to

the Faculty of the Graduate School

at the University of Missouri – Columbia

In Partial Fulfillment

of the Requirement for the Degree

Master of Science

By

KYLER K. TURNER

Dr. Gary Solbrekken, Thesis Supervisor

MAY 2009

The undersigned, appointed by the dean of the Graduate School, have examined the thesis entitled

THERMAL-MECHANICAL ANALYSIS OF TARGETS FOR HIGH VOLUME PRODUCTION OF MOLYBDENUM-99 USING LOW-ENRICHED URANIUM

Presented by Kyler K. Turner

A candidate for the degree of Masters of Science

And hereby certify that in their opinion it is worthy of acceptance.

Dr. Gary Solbrekken

Dr. Sherif El-Gizawy

Dr. Stephen Montgomery-Smith

ACKNOWLEDGEMENTS

I would like to thank Dr. Gary Solbrekken for his guidance during the life of this project. The infinite patience, input, and believe in me he has displayed over the last two years has been instrumental in making this work possible. Further, I would like to thank my mother and aunt for guiding me into the field of engineering and science and for pushing me both personally and academically throughout my life. I would also like to thank my father for always believing in me. Of course I can not forget to thank the rest of my family such as my brother, aunts, uncles and grandparents for everything they have done for me in the past. Finally I would like to thank my fellow colleagues Colin Graham, Jeff Scott, and Matt Mullens for their help on this project.

TABLE OF CONTENTS

| | |
|--|------|
| ACKNOWLEDGEMENTS | ii |
| LIST OF FIGURES..... | v |
| LIST OF TABLES | xi |
| NOMENCLATURE | xii |
| ABSTRACT..... | xiii |
| Chapter | |
| 1. INTRODUCTION AND PURPOSE..... | 1 |
| Forward..... | 1 |
| History and Background..... | 1 |
| Technetium-99m..... | 3 |
| Purpose of the Study..... | 5 |
| 2. TARGET DESIGN APPROACHES | 7 |
| Cylindrical Target Design..... | 9 |
| Plate Target Design..... | 11 |
| 3. CYLINDRICAL TARGET DESIGN MODELING..... | 13 |
| Analytical Models..... | 14 |
| Numerical Model..... | 20 |
| 4. CYLINDRICAL TARGET DESIGN RESULTS AND DISCUSSION..... | 25 |
| Analytical Model..... | 25 |
| Numerical Model..... | 29 |
| Interfacial Heating..... | 34 |

| | |
|--|-----|
| 5. PLATE TARGET DESIGN MODELING..... | 38 |
| Analytical Model..... | 38 |
| Numerical Model..... | 40 |
| Experimental Setup..... | 43 |
| 6. PLATE TARGET DESIGN RESULTS AND DISCUSSION..... | 57 |
| Analytical Model..... | 57 |
| Numerical Model..... | 59 |
| Experimental Setup..... | 76 |
| Plate Target Numerical and Experimental Comparison..... | 79 |
| 7. CONCLUSIONS..... | 81 |
| 8. RECOMMENDATIONS..... | 83 |
| 9. APPENDIX..... | 84 |
| 1. Matlab Code | |
| A. Analytical Code for the Cylindrical Target..... | 84 |
| B. M-file used to find Stress Values for Madhusudana’s work..... | 87 |
| 2. Algor Plate Procedure..... | 90 |
| 3. Plate Numerical Model Results Partially Constrained with Gas Pressure..... | 100 |
| 4. Plate Experiment Results..... | 102 |
| 10. REFERENCES..... | 109 |

LIST OF FIGURES

| Figure | Page |
|--|------|
| 1. Dimensions and Cross Sectional view of the 20 g LEU annular target..... | 9 |
| 2. Plate target configuration..... | 11 |
| 3. Example of plate target pillowing..... | 12 |
| 4. Cylinder physical properties..... | 15 |
| 5. Heat transfer resistance network for the cylindrical target..... | 18 |
| 6. 2-D sketch of the cylinder ends..... | 20 |
| 7. 3-D assembly of the combined cylinders as a solid and wire frame model..... | 21 |
| 8. Automatic mesh generating settings..... | 22 |
| 9. Image showing the physical boundary conditions applied to the target..... | 24 |
| 10. Cut away diagram of the three different heating situations..... | 26 |
| 11. Temperature as a function of radius..... | 26 |
| 12. Radial stress as a function of target thickness for the outside and inside surface heating condition with interface location..... | 27 |
| 13. Temperature distribution of the inner surface heating condition..... | 29 |
| 14. Temperature distribution of the outer surface heating condition..... | 30 |
| 15. Radial stress distribution for inner surface heating..... | 31 |
| 16. Radial stress distribution for outer surface heating..... | 31 |
| 17. Location of interface length..... | 33 |
| 18. Plot of the stresses in the radial direction at the interface for Inside and outside surface heating..... | 33 |

| | |
|--|----|
| 19. Temperature distribution as function of radius for the inner, interfacial and outer heating conditions..... | 35 |
| 20. Temperature distribution of the interfacial heating condition..... | 35 |
| 21. Radial stress as a function of target thickness for the interfacial heating condition..... | 36 |
| 22. Radial stress distribution for interfacial heating..... | 36 |
| 23. Analytical model beam assumed infinitely long in the Y direction and no weld on the edges..... | 38 |
| 24. Completed plate target mesh in Algor..... | 41 |
| 25. Plate Target model in the thermal analysis..... | 42 |
| 26. Plate Target model in the structural analysis..... | 43 |
| 27. Heater that has experienced burnout..... | 44 |
| 28. External connection point heater failure..... | 45 |
| 29. Heater with flatted wire and aluminum foil heat spreaders..... | 46 |
| 30. Diagram of electrical power source and heater..... | 47 |
| 31. Heater with Thermocouple locations and heating wire outline..... | 48 |
| 32. Electrical connections..... | 48 |
| 33. Fully assembled plate..... | 49 |
| 34. Schematic of the flow loop..... | 50 |
| 35. Image of the completed flow loop..... | 50 |
| 36. Image of the completed flow loop..... | 51 |
| 37. Test section dimensions in inches..... | 51 |
| 38. Extender arms in the test section with plate..... | 53 |

| | |
|---|----|
| 39. Close up view of the extender arms..... | 53 |
| 40. Lower and upper plate holders..... | 54 |
| 41. Slot adjustment system..... | 54 |
| 42. Internal data wire connections and power supply connection..... | 55 |
| 43. Test section pass-throughs for the data wiring and the power supply..... | 55 |
| 44. Complete data acquisition system..... | 56 |
| 45. Digital Multimeter and Connection Board..... | 56 |
| 46. Analytical beam illustration..... | 57 |
| 47. Plate model analytical results with a beam length of 30mm and varying beam thickness..... | 58 |
| 48. 1.0 mm thick beam deflection as a function of the length along the X axis with varying heat flux from 1kW to 50kW..... | 58 |
| 49. Numerical model plate edge boundary conditions | |
| 50. Fully constrained at $h = 20,000 \text{ W/mK}$ | 61 |
| 51. Partially constrained at $h = 20,000 \text{ W/mK}$ | 61 |
| 52. Only Z constrained at $h = 20,000 \text{ W/mK}$ | 62 |
| 53. Fully constrained at $h = 10,000 \text{ W/mK}$ | 62 |
| 54. Partially constrained $h = 10,000 \text{ W/mK}$ | 63 |
| 55. Only Z axis constrained $h = 10,000 \text{ W/mK}$ | 63 |
| 56. Only Z axis constrained $h=10,000 \text{ W/mK}$ with a uniform heat flux..... | 64 |
| 57. Fully Constrained at a 5psi gas pressure..... | 65 |
| 58. Fully Constrained at 5psi and no $L=0.5\text{mm}$ data..... | 66 |
| 59. Fully Constrained at a 10psi gas pressure..... | 66 |

| | |
|--|----|
| 60. Fully Constrained at 10psi and with no 0.5mm plate thickness data..... | 67 |
| 61. Only Z axis constrained at a 5psi gas pressure..... | 67 |
| 62. Only Z axis constrained at 5psi and with no 0.5mm plate thickness data..... | 68 |
| 63. Only Z axis constrained at a 10psi gas pressure..... | 68 |
| 64. Only Z axis constrained at 10psi and with no 0.5mm plate thickness data..... | 69 |
| 65. Combine thermal and gas pressure effects for 2.0mm thickness at $h=10,00W/mK$ | 70 |
| 66. Fully constrained deflection in the Z direction contour plot..... | 71 |
| 67. Partially constrained deflection in the Z direction contour plot..... | 71 |
| 68. Fully constrained deflection in the Z direction contour plot..... | 71 |
| 69. Fully constrained Von Mises stress gradient..... | 72 |
| 70. Partially constrained Von Mises stress gradient..... | 72 |
| 71. Only Z axis constrained Von Mises stress gradient..... | 73 |
| 72. Experiment three thermocouple three thermal resistance..... | 77 |
| 73. Experiment four thermocouple three thermal resistance..... | 77 |
| 74. Experiment five thermocouple three thermal resistance..... | 77 |
| 75. Experiment six thermocouple three thermal resistance..... | 78 |
| 76. Kapton before and after testing..... | 79 |
| 77. Algor simulation of the experimental test plates..... | 80 |
| A1. Part in Inventor..... | 91 |
| A2. 2D Mesh..... | 92 |
| A3. Heat Flux surface selection..... | 93 |
| A4. Mesh extrusion changes..... | 94 |

| | |
|--|-----|
| A5. Mesh surface selection of bottom surface..... | 95 |
| A6. Completed plate target mesh in Algor..... | 96 |
| A7. Plate Target model in the thermal analysis..... | 97 |
| A8. Changing the analysis type..... | 98 |
| A9. Plate Target model in the structural analysis..... | 99 |
| B1. Partially constrained results with a 5psi gas pressure..... | 100 |
| B2. Partially constrained results with a 5psi gas pressure and with no 0.5mm plate thickness data..... | 100 |
| B3. Partially constrained results with a 10psi gas pressure..... | 101 |
| B4. Partially constrained results with a 10psi gas pressure and with no 0.5mm plate thickness data..... | 101 |
| C1. Experiment 3 thermocouple 1 results..... | 102 |
| C2. Experiment 3 thermocouple 2 results..... | 102 |
| C3. Experiment 3 thermocouple 3 results..... | 102 |
| C4. Experiment 3 thermocouple 4 results..... | 103 |
| C5. Experiment 3 thermocouple 5 results..... | 103 |
| C6. Experiment 4 thermocouple 1 results..... | 103 |
| C7. Experiment 4 thermocouple 2 results..... | 104 |
| C8. Experiment 4 thermocouple 3 results..... | 104 |
| C9. Experiment 4 thermocouple 4 results..... | 104 |
| C10. Experiment 4 thermocouple 5 results..... | 105 |
| C11. Experiment 5 thermocouple 1 results..... | 105 |
| C12. Experiment 5 thermocouple 2 results..... | 105 |
| C13. Experiment 5 thermocouple 3 results..... | 106 |

| | |
|---|-----|
| C14. Experiment 5 thermocouple 4 results..... | 106 |
| C15. Experiment 5 thermocouple 5 results..... | 106 |
| C16. Experiment 6 thermocouple 1 results..... | 107 |
| C17. Experiment 6 thermocouple 2 results..... | 107 |
| C18. Experiment 6 thermocouple 3 results..... | 107 |
| C19. Experiment 6 thermocouple 4 results..... | 108 |
| C20. Experiment 6 thermocouple 5 results..... | 108 |

LIST OF TABLES

| Table | Page |
|--|------|
| 1. Location and boundary condition information for the thermal mode..... | 22 |
| 2. Location and boundary condition information for the structural mode..... | 23 |
| 3. Model surface boundary conditions..... | 25 |
| 4. Model surface temperature results..... | 30 |
| 5. Inner surface heating condition comparison with percent difference..... | 32 |
| 6. Outer surface heating condition comparison with percent difference..... | 32 |
| 7. Comparison of cylinder interface results..... | 34 |
| 8. Summary of the numerical plate boundary conditions..... | 60 |
| 9. Von Mises stress results when only constrained along the Z axis at 50kW..... | 74 |
| 10. Von Mises stress results when fully constrained at 20kW..... | 74 |
| 11. Von Mises stress results when only constrained along the Z axis at 20kW..... | 74 |
| 12. Von Mises stress results when fully constrained at 20kW..... | 75 |
| 13. Yield and tensile strengths of possible cladding at factor of safety of 1.2..... | 75 |
| 14. Maximum power and maximum temperature reached before failure..... | 76 |
| 15. Comparison of experimental and numerical experiments of the plate..... | 80 |

LIST OF NOMENCLATURE

| | | | |
|-------|--|----------------------|---|
| C | Celsius | Greek | |
| E | Young's Modulus | α | coefficient of thermal expansion |
| g | gram | Δ | difference |
| h | heat transfer coefficient | ν | Poisson's ratio |
| H | microhardness | θ | surface slope |
| K | Kelvin | σ | effective rms surface roughness |
| k | thermal conductivity | Subscripts | |
| m | meters | i | inner |
| Pa | Pascal | o | outer |
| P | pressure | r | radius |
| q'' | heat flux | Abbreviations | |
| R | thermal resistance | ANSTO | Australian national nuclear research and development organization |
| s | seconds | FEA | finite element analysis |
| T | temperature | GTRI | global threat reduction initiative |
| TC | thermocouple | HEU | highly enriched uranium |
| u | total interference between the cylinders | IND | improvised nuclear device |
| u_A | expansion due to temperature gradients | LEU | low enriched uranium |
| u_B | expansion due to contact resistance | MURR | University of Missouri Research Reactor |
| u_C | initial interference | NRC | Nuclear Regulatory Commission |
| V | volts | RERTR | Reduced Enrichment for Research and Test Reactors Program |
| W | watts | | |

Abstract

Techenetium-99m is diagnostic radioactive medical isotope that is currently used 30,000 times a day in the United States. All supplies of techenetium-99m's parent isotope molybdenum-99 currently originate from nuclear reactor facilities located in foreign countries and use highly enriched uranium (HEU). The University of Missouri Research Reactor (MURR) is exploring the feasibility of high volume molybdenum-99 production at its facility.

Current molybdenum-99 production uses HEU in a powder dispersion target. The powder dispersion method, conventionally used for fuel rods and plates, combines fine particles of aluminum and HEU that are bonded into a rigid plate during irradiation. In accordance with the Global Threat Reduction Initiative all uranium used in future molybdenum-99 production will use low enriched uranium (LEU). Unfortunately LEU has a much low fissionable density than HEU which makes the dispersion process economically unviable. A design approach to increase the LEU density is to use a target that is based on LEU foil. The foil design places a LEU foil between either two concentric annular aluminum cylinders or two aluminum plates which are pressed and welded together to produce a structure that allows for easy removal and processing. The drawback of these designs is the thermal contact resistance between the LEU and aluminum cladding during irradiative heating is very sensitive to the target design, manufacture, and irradiation holder. This thesis explores those thermal-mechanical design issues for both the cylindrical target design and the plate target design. Analytical, numerical and experimental studies are used to assess the mechanical deformation for these structures and its effect on the target's thermal contact resistance.

Chapter 1: Introduction and Purpose

Foreword

The first techniques used to diagnose illnesses in patients were performed by physical examination. This technique is limited however since the examiner can not truly see what is taking place inside the patient without performing surgery and in many cases it is neither practical nor safe to attempt. Modern medicine has solved this problem by developing non-invasive internal examination techniques such as technetium-99m diagnostic therapy. One of the most commonly practiced techniques in the world today. Technetium-99m diagnostic therapy is used nearly 30,000 times a day (Miller, 2008) in the United States as a non-invasive cancer diagnostic technique. Currently the United States' supply of technetium-99m's parent isotope, molybdenum-99, is entirely supplied by foreign countries. It is for this reason the University of Missouri Research Reactor (MURR) is attempting to become the United States' sole domestic supplier of molybdenum-99, which will naturally lead to a domestic supply of technetium-99m.

History and Background

In 1895 the German physicist Wilhelm Konrad Roentgen made a monumental discovery. He found through experimentation, that when crystals of barium platinocyanide were placed near a highly evacuated electrical discharge tube the crystals became luminescent. Continued experimentation showed that when an object was placed between the crystals and the tube. The object would block the invisible radiation that was being given off by the crystals, further the amount of radiation blockage depended greatly on the density of the object. Roentgen named this invisible radiation X-rays after the variable used in math for an unknown amount. The name stuck and now most English

speaking countries use the term x-rays in their common culture. The same year Roentgen made his discovery he also produced the first the medical x-ray image in history when he produced an image of his wife's hand (Williams and Zolle, 1976 and 2007). It was the first time in history that a non-invasive technique had been used to examine the internal conditions of the body. Consequently Roentgen won the 1901 Nobel Prize in Physics for his monumental discovery.

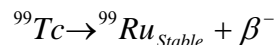
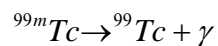
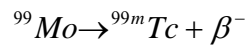
Work continued on naturally occurring radioactive materials for nearly 35 years after Roentgen's discovery. Notable work done during this time includes the work of Marie Curie, who helped identify many new radioactive elements and also coined the term "radioactivity" (Williams, 1976) Ernest Rutherford also did notable work during this time period. He determined the behavior of the radiation emitted from many of the new radioactive elements and found that radiation could be broken into several different types. These types of radiation would later be called alpha particles, beta particles, and gamma rays. During this time period all radiation research was done using naturally occurring radioactive elements. It was not until the experiments of Cockcroft and Walton during the 1930's that the first man made radioactive isotopes were produced (Zolle, 2007).

In 1932 Cockcroft and Walton produced the first man made neutron deficient isotopes using a charged particle accelerator. Seven years later the first recognized observation of fission was recorded by Hahn and Strassman. In their experiment they bombarded uranium with neutrons and observed the splitting of the uranium atom and the energy it gave off (Zolle, 2007). In 1938 for the first time in history a radioactive isotope was injected into a living organism. Dr. Robley D. Evans of the Massachusetts General Hospital and members of the Massachusetts Institute of Technology injected a rabbit with

Iodine-138 to observe the uptake of the isotope into thyroid gland, though at this time a scanner had not been developed to measure the radiation given off by the Iodine. In 1950 the first localized radiation scanner was developed and designed specifically for the study Iodine-138 uptake in the thyroid gland. Shortly after the first whole body scanner was invented by Donner Laboratory in 1952. In the 1960's as the technology continued to advance the area of nuclear medicine had developed to the point that it was now considered a medical specialty in its own right. (Williams, 1976).

Technetium-99m

Technetium-99m is one example of the many different medical isotopes that were created during the early days of man-made isotope production. Technetium-99m is the product of molybdenum-99 decay, has the atomic number 43, has a half-life of about six hours and is in a metastable state (Sonzogni). The nuclear decay equations below show the complete decay chain of molybdenum-99 into its stable form of Ruthenium-99,



where Mo is molybdenum, Tc is technetium, Ru is ruthenium, γ is a gamma ray and β^{-} is a beta particle. Technetium was initially discovered in 1937 by Carlo Perrier and Emilio Segre while exposing a molybdenum-99 strip with 8MeV deuterons. In 1965 Brookhaven National Lab produced the first molybdenum-99 / technetium-99m generator, which allowed the collection or “milking” of the technetium-99m from molybdenum-99 decay (Zolle and Miller, 2007 and 2008). Technetium-99m's six hour

half-life limits the distance that the isotope can travel before the activity of the isotope becomes too low to be used. This means that the hospitals wanting to use technetium-99m have to be built near a nuclear reactor producing technetium-99m or vice versa. The technetium-99m generator increased the amount of time available before administration had to take place. Increasing the useable time took advantage of the naturally longer half life of molybdenum-99. When the generator leaves its production facility, i.e. a nuclear reactor, the isotope is nearly all molybdenum-99. Molybdenum-99's half life of 65 hours, or about 2 and half days, allows the molybdenum-99 to exist for a much longer time period than technetium-99m (Miller, 2008).

The parent daughter relationship between molybdenum-99 and technetium-99m is a non-equilibrium relationship meaning, that the daughter's half-life is shorter than the parent's half-life. Their non-equilibrium relationship allows molybdenum-99 to undergo the milking process once a week. [Column chromatography](#) is used to separate the two isotopes during the milking process. This process separates the isotopes into negatively charged particles of TcO_4^- and MoO_4^{2-} . The single negative charge on the TcO_4^- adheres to the alumina in the generator far less than the double negative charge on the MoO_4^{2-} . A saline solution is used to flush the free floating TcO_4^- from the generator, which produces a saline solution that is full of technetium-99m (Zolle and Miller, 2007 and 2008). When technetium-99m is injected into a human the body it gathers in areas of high metabolism such as a cancerous tumor. A gamma camera detects the strength of gamma rays emitted by the technetium-99m in the patient. An area of high gamma ray concentration suggests the possibility of a tumor.

Technetium-99m from a medical stand point is nearly ideal for use as radiopharmaceutical. First, the molybdenum-99 / technetium-99m generator is easy to transport and store without over exposure. Shielding required for the average activity transported is on the order of 2 cm of lead. Second, the half life of six hours is quite short; minimizing the dose to the patient receives. On average a person that has been injected with the technetium-99m will return to a background radiation reading within 4 days. Third, technetium-99m only gives off gamma rays limiting the exposure to the patient (Miller, 2008). These advantages are why technetium-99m's use as a diagnostic medical tracer is 85% of the total medical isotope procedures in the United States (Zolle, 2007).

Purpose of the Study

MURR is attempting to become the sole domestic supplier of molybdenum-99. Current molybdenum-99 supplies come from nuclear reactors located in Canada, the Netherlands, South Africa, and Belgium. The foreign location of these reactors has created a great amount of concern among persons in the medical community. Technetium-99m is used so frequently that any slowdown in production will have a great effect on global supplies. This fear was recently realized when the Petton Reactor located in the Netherlands and the NRU Reactor in Canada, were shut down because of mechanical problems. The recent shutdowns have alerted the medical and nuclear communities in United States to the real dangers associated with not having a domestic molybdenum-99 supply.

Currently all molybdenum-99 production is based on highly enriched uranium (HEU) or uranium that contains at least 20% U-235. HEU's high concentration of U-235

makes it a great choice for high volume molybdenum-99 production but it also creates many problems. HEU is the primary fuel source for uranium based nuclear weapons which obviously has created a great amount of concern in the United States and the international community. The Global Threat Reduction Initiative (GTRI) was created in 2004 and “works to identify, secure, remove and/or facilitate the disposition of high risk vulnerable nuclear and radiological materials (i.e. HEU) around the world, as quickly as possible, that pose a threat to the United States and the international community (NNSA Office of Global Threat Reduction)”. The production of molybdenum-99 using HEU falls under the initiative and it is for this reason MURR is exploring molybdenum-99 production based on low enriched uranium (LEU).

MURR is just beginning to explore high volume production of molybdenum-99 using LEU. One of the main obstacles is the development of a target that is cost effective. A cylindrical target that uses LEU foil has been designed by Argonne National lab. However, the cost effectiveness of the cylindrical design in a high volume production environment is in question.

The purpose of the current research is to evaluate the thermal mechanical behavior of the cylindrical and plate target geometries. One of the MURR technical requirements is that the LEU foil temperature may not exceed one half the melting temperature of the lowest melting point material in the target. For our reference target the aluminum cladding will limit this to 330°C. The thermal contact resistance is the metric which governs the LEU temperature. Analytical, numerical and experimental studies are carried out to estimate the thermal contact resistance and to assess the risk of failure in the targets.

Chapter 2: Target Design Approaches

Reactors throughout the world that have been producing molybdenum-99 for many years, production as mentioned previously starts by bombarding either HEU or LEU with neutrons from a nuclear reactor. The neutron bombardment creates a nuclear fission reaction within the uranium which produces a large amount of fission products including molybdenum-99 and heat. The purpose of the target is to contain the fission products for later processing and to dissipate heat from the uranium. This must be done while keeping the LEU foil below 330°C and maintaining the target surface temperature below the saturation temperature of the cooling fluid. The conduction within, and the convection of the heat from the target are two great challenges in the molybdenum-99 production process.

The traditional process used for molybdenum-99 production throughout the world is a powder dispersion target. In this process HEU is mixed in powder form with aluminum powder (Solbrekken, 2008). The two powders are then heated and compressed between two aluminum plates to create a monolithic plate. The monolithic nature of the plate ensures that there is no gas gap between the uranium and the aluminum creating a low thermal contact resistance through the target. The molybdenum-99 is collected by dissolving the entire plate, resulting in expensive liquid waste.

In the new target design, LEU will be used instead of HEU which has a much lower concentration of U-235. The lower concentration of U-235 means that the previously mentioned powder dispersion method will not work, as it does not supply an adequate U-235 density in the finished target. A foil comprised of LEU supplies a much higher density of U-235 than the powder. The foil, which is not unlike household

aluminum foil, is wrapped in nickel foil and placed between aluminum cladding. The nickel foil recoil barrier ensures that the LEU foil does not bond to the aluminum cladding during irradiation. After irradiation the aluminum cladding is cut open to retrieve the only the LEU foil, which is then dissolved retrieving the molybdenum-99. This process, known as the modified process, reduces the amount of costly liquid waste. This design strategy, unlike the powder dispersion design, unfortunately this does not create a monolithic structure. The laminated structure implies that there will be a significant thermal contact resistance between the layers of uranium, nickel and aluminum. Questions about the thermal contact resistance were the primary driver behind cylindrical target design development. It is believed that the cylindrical target will maintain a low thermal contact resistance but it is unclear whether it is the most cost effective design. Since there have been no studies conducted in the cylindrical target design these questions must still be answered. An alternative plate target design is under investigation because it is believed to be the more cost effective design in a high volume production environment.

Establishing a production facility at MURR for molybdenum-99 will require a reactor license amendment to be granted by the NRC. The required modification to the reactor design must be documented to demonstrate the safety of the process. The safety requirements for the target design include keeping the material temperature below a half of the melting temperature of aluminum and ensuring no fission products leak from the target. Two primary design concepts are considered here

Cylindrical Target Design

The annular target design consists of two concentric aluminum cylinders that are welded at their ends. A reference annular target design has been developed by Argonne National Lab through the RERTR program (Solbrekken, 2008). A sketch of their approach with nominal dimensions is shown in figure 1.

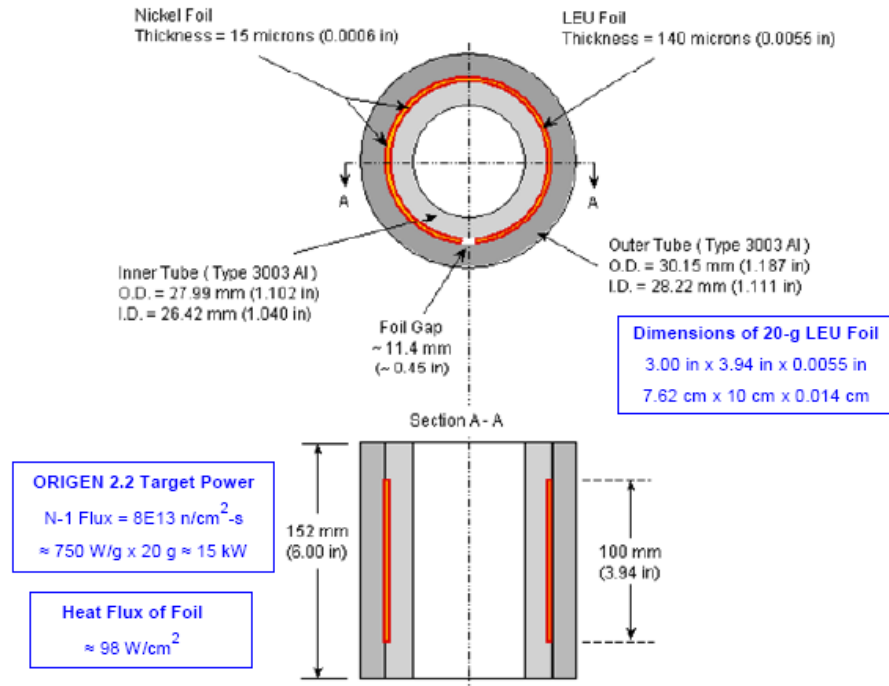


Figure 1. Dimensions and Cross Sectional view of the 20 g LEU annular target.

(Solbrekken, 2008)

The LEU foil along with a nickel recoil barrier is placed between two aluminum cylinders which are then drawn together using a plug die. The ends of the cylinders are welded together producing a completely sealed environment for the LEU foil.

The Argonne target has been evaluated by Aareva-Cerca for thermal and mechanical behavior during irradiation (Renhart, 2004). They showed a maximum temperature of 148.1 °C using very flat rolled LEU foil in perfect contact. They evaluated their thermal margin using the numeric code CFX and an experimentally determined

thermal contact resistance (Yeoh, 2004). There are two significant drawbacks with their thermal analysis that precludes it from being used here. First, the test methodology used to evaluate the thermal contact resistance does not effectively reproduce the usage conditions. Second, their analysis did not provide an envelope for the variation in the foil thickness and roughness. This later analysis is required to set the incoming material tolerances needed for high volume production. This thesis will address the test methodology questions and the purpose of a test design which will assist a foil design envelope study in the future. Numeric and analytic thermal mechanical models are used to develop the test bed concept.

The Argonne annular target was not designed with high volume production goals in mind. Therefore, there is no reason to believe that it is the most cost effective design. In fact, one can consider the annular target to be a special case of a more general plate design concept. The plate design can be curved to the point that its ends meet reproducing the cylindrical target. It is necessary to complete a technical design analysis of the plate target to allow an economic analysis.

Plate Target Design

The plate target structure consists of a LEU foil sandwiched between two nickel recoil barriers and two aluminum plates approximately 1mm thick. The aluminum plates are pressed and welded together on their edges. Figure 2 shows the configuration of the plate target design.

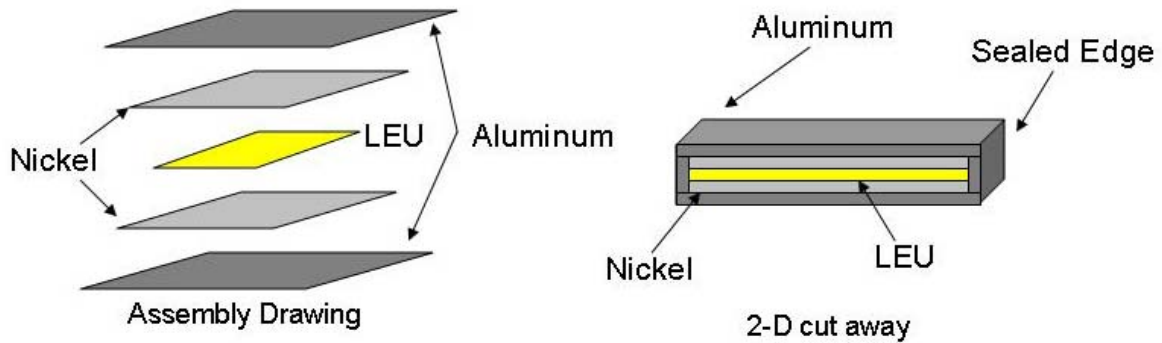


Figure 2. Plate target configuration

During irradiation a large amount of heat is generated within the LEU equal to about 750 W/g. Sufficient cooling must be provided by the reactor pool to remove the heat produced by the fission reaction.

One of the greatest areas of concern is the behavior of the plate target under heating. During heating the aluminum will tend to expand as its temperature increases. The non-uniform heating within the target will create a three dimensional temperature profile. The thermal expansion that develops due to the temperature distribution will likely cause pillowing. This behavior would open a gap between the LEU and the cladding possibly causing the LEU to overheat. An example of pillowing can be seen in figure 3.

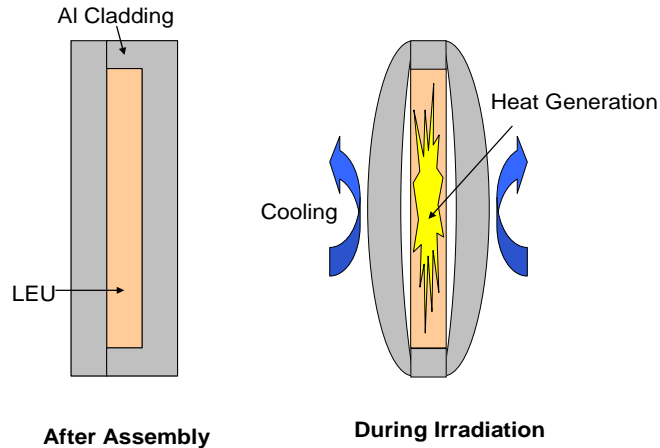


Figure 3. Example of plate target pillowing (Solbrekken and El-Gizawy, 2008)

The aim of the plate target investigation is to develop models that describe the behavior of the target under irradiation. Investigation of the plate target geometries was done by numeric and analytic models. In conjunction with the numerical and analytic models experimental data was collected for the flat plate target geometry using a flow loop developed to measure data on plate test vehicles. Unlike the cylindrical target which has been successfully used to process molybdenum-99 in the past, the plate target is a completely new design. The nature of a new design means that there are many unknowns including the behavior of the target while in use and how to evaluate the effectiveness of the target.

Chapter 3: Cylindrical Target Design Modeling

The LEU temperature will not only be limited by the convective cooling of the water but also by the ability of the thermal energy to conduct across the interfaces in the target. If there is not a sufficient amount of conduction through the cylinders then there will be an increase in the thermal resistance leading to an unacceptable rise in interfacial temperature. The temperature distribution through the cylinders will cause thermal expansion and stress to form. If the thermal expansion is too extensive, it could cause a gap to form between the cylinders, the LEU, and the nickel recoil barrier. The gap will in turn decrease the internal contact conductance of the target. It should be noted that the nickel recoil barrier is ignored during the study. Decreasing the interfacial thermal contact will in turn increase the thermal resistance through the cylinder. It is the thermal resistance of the cylinder that will be simulated numerically and analytically.

The thermal contact resistance of the cylinders can be found using the contact pressure and the stress at the interface of the joint, as suggested by equation 1 from Madhusudana (Madhusudana 1996 and 1998)

$$R = \frac{\Delta T}{q''} = \left(\left(1.13 \tan \Theta \left(\frac{k}{\sigma} \right) \left(\frac{P}{H} \right) \right)^{0.85} \right)^{-1} \quad (1)$$

Equation 1 relates the thermal contact resistance between the LEU foil and the aluminum cladding using the contact pressure at the interface of the cylinders. The contact pressure at the interface is combination of the pressure created during assembly and the pressure induced by thermal expansion. Assembly pressure can be found using a manufacturing assembly analysis and the thermal expansion can be super imposed on the contact pressure.

The goal of the cylindrical target model is develop an experimental approach to evaluate the thermal resistance. The thermal interface analysis completed by Areva-Cerca for ANSTO used a technique described briefly in a presentation given by Areva-Cerca (Areva-Cerca, 2007). The laser flash technique, based on the developments of Milosevic, Raynaud and, Maglic, applied heating to local spots on the interior of the target (Milosevic, Raynaud and Maglic, 2003) It is hypothesized here that interior heating will put the interface into an overly optimistic state compared with the application state. The models that follow are intended to evaluate this hypothesis and to propose a testing process.

Analytical Models

The first analytical model attempted was based on the work by Madhusudana. In an article Madhusudana develops a model that describes the heat flow across a joint formed by two concentric cylinders (Madhusudana, 1998). He finds that the contact pressure between the cylinders is highly dependent on the direction of the energy flow. It was believed that the method used by Madhusudana could be modified and applied to the cylindrical target. Thus, in an attempt to apply the joint model to the processing target, a reproduction of the derivation and results from Madhusudana was done.

The pressure that develops in a cylindrical joint as result of the interface between the cylinders can be described by the mechanical interference (u). The total interference is a combination of the u_A , u_B , and u_C . u_A is due to thermal expansion of the cylinders, u_B is the differential expansion caused by the thermal contact resistance at the joint interface, and u_C is due to assembly. Equation 2 gives the relationship between

interference, radius, and heat flow direction. The definitions of the radii and the heat flow direction can be seen in figure 4.

$$\frac{u_A + u_B + u_C}{b} = \frac{p}{E_i} \left[\frac{E_i}{E_o} \left[\frac{c^2 + b^2}{c^2 - b^2} + \nu_o \right] + \left[\frac{b^2 + a^2}{b^2 - a^2} - \nu_i \right] \right] \quad (2)$$

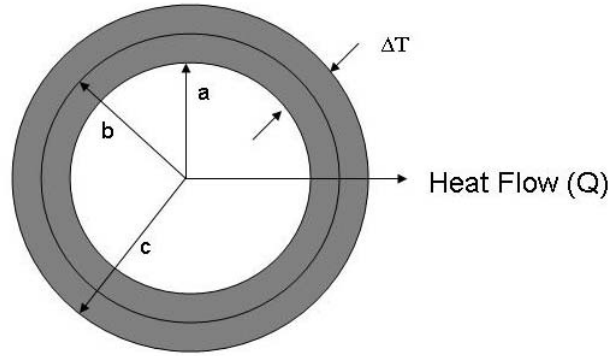


Figure 4. Cylinder physical properties

The interference caused by the heat flow u_A is found by describing the radial displacement of both the inner and outside cylinders. The relationship of the total heat flow interference is $u_A = u_{Ai} - u_{Ao}$ and solving for u_A yields equation 3

$$\frac{u_A}{b} = \frac{b\alpha_i\Delta T_i}{2\ln(b/a)} \left(\frac{\alpha_o k_i}{\alpha_i k_o} \right) \left[1 - \frac{2c^2}{c^2 - b^2} \ln(c/b) \right] \quad (3)$$

The total interference due to the thermal contact resistance is represented by u_B .

This total resistance is a combination of $u_{Bi} - u_{Bo}$ which is equal to equation 4

$$u_B = b[(T_a - \Delta T_i)(\alpha_i - \alpha_o) + \alpha_o\Delta T] \quad (4)$$

where T_a is the temperature of the inner cylinders surface and $\Delta T = \frac{Q}{2l\pi bh}$. Finding the

effective heat transfer coefficient (h) was done by separating h into the solid spot (h_s)

and gas gap (h_g) conductance components. Combining the ΔT equation with equation 4

gives equation 5.

$$\frac{u_B}{b} = (\alpha_i - \alpha_o)(T_a - \Delta T_i) + \alpha_o \left(\frac{k_i}{b \ln(b/a)} \right) \left[\frac{1}{(0.55 \tan \theta (k/\sigma))} \right] \quad (5)$$

The assembly interference u_c is assumed to be known. Solving for the total interference assumes that the values for u_c range from 0 m to 0.0005 m. The derivation was used to solve a multitude of information about the cylinder including interfacial contact pressure and interfacial thermal contact conductance under varying input conditions. Combing the different interface u values and solving for the contact pressure p gives equation 6.

$$p = \left(\frac{\left[\frac{u_A + u_B + u_C}{b} \right]}{\left[\frac{E_i}{E_o} \left[\frac{c^2 + b^2}{c^2 - b^2} + \nu_o \right] + \left[\frac{b^2 + a^2}{b^2 - a^2} - \nu_i \right] \right]} \right) E_i \quad (6)$$

Derivation of a second model was attempted because Madhusudana's model could not be replicated. Instead of using previous work, a model was developed from basic stress equations. The derivation begins with a general equation which gives the radial stress of long circular cylinder as a function of radius and can be seen in equation 7 (Ugural and Fenster)

$$\sigma_r(r) = \frac{E}{1+\nu} \left[\frac{-(1+\nu)\alpha}{(1-\nu)r^2} \int_a^r Trdr + \frac{c_1}{1-2\nu} - \frac{c_2}{r^2} \right] \quad (7)$$

where a is the inner radius of the cylinder, r is the location along the radius and c_1/c_2 are the constants of integration. Assuming that the cylinder has a central circular hole the boundary conditions $(\sigma_r)_{r=a} = (\sigma_r)_{r=b} = 0$ are applied and the constants of integration

are $c_1 = \frac{(1+\nu)(1-2\nu)\alpha}{(1-\nu)(b^2 - a^2)} \int_a^b Trdr - \nu\varepsilon_z$ and $c_2 = \frac{(1+\nu)a^2\alpha}{(1-\nu)(b^2 - a^2)} \int_a^b Trdr$. Where a is the

cylinder's inner radius and b is the cylinder's outer radius.

The target was assumed to be a solid cylinder with a central circular hole meaning that the two cylinders are perfectly bonded at their interface. Using this assumption and starting with equation 8 (Ugural and Fenster) a model for the temperature depended stresses as a function of radial position and temperature in the cylinder can be found.

$$\sigma_r(r) = \frac{E}{1-\nu} \left[-\frac{\alpha}{r^2} \int_a^r rTdr + \frac{(r^2 - a^2)\alpha}{r^2(b^2 - a^2)} \int_a^b rTdr \right] \quad (8)$$

The general integration of $\int_y^x rTdr$ will describe the temperature of the cylinder as a function of radius. The derivation of the general equation starts by first describing the temperature as a function of radius $T(r)$. $T(r)$ will differ depending on the heating and cooling conditions applied to the cylinder. A $T(r)$ equation was developed for both the inside heating condition and the outside heating condition. The heat transfer resistance network (Incropera and Dewitt, 2005) in figure 5 was used to produce an equation describing the temperature as function of radius for both heating conditions. The inside heating condition equation can be seen in equation 9 and outside heating condition can be seen in equation 10.

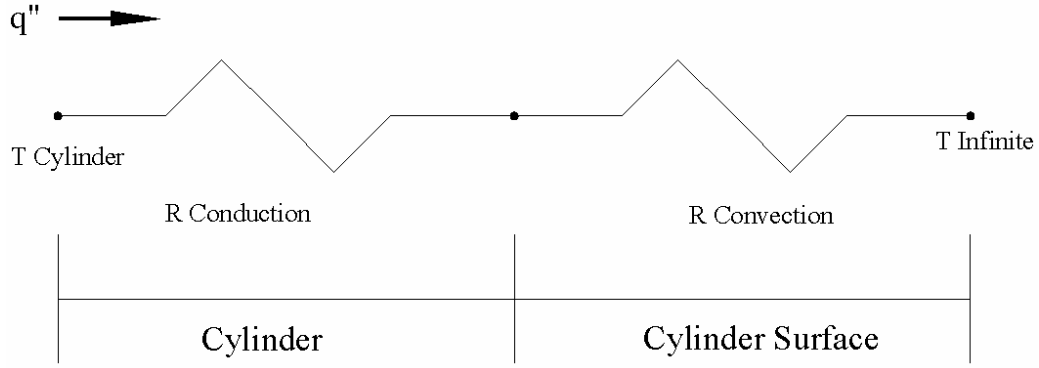


Figure 5. Heat transfer resistance network for the cylindrical target

$$T(r) = T_{\infty} + \frac{q'' a}{k} \left[\ln\left(\frac{b}{r}\right) + \frac{k}{hb} \right] \quad (9)$$

$$T(r) = T_{\infty} + \frac{q'' b}{k} \left[\ln\left(\frac{a}{r}\right) + \frac{k}{ha} \right] \quad (10)$$

Equation 9 and 10 is then used in $\int_y^x r T r dr$ and integrated using the appropriate limits of integration. The integration of the two equations can be seen below for both the inside heating condition and the outside heating condition.

$$(Inside) \int_a^r r T r dr = \int_a^r r \left(T_{\infty} + Q \left[\ln\left(\frac{b}{r}\right) + \frac{k}{hb} \right] \right) dr \quad \text{where } Q = \frac{q'' a}{k} \quad (11)$$

$$(Outside) \int_b^r r T r dr = \int_b^r r \left(T_{\infty} + Q \left[\ln\left(\frac{a}{r}\right) + \frac{k}{ha} \right] \right) dr \quad \text{where } Q = \frac{q'' b}{k} \quad (12)$$

Simplifying gives

$$(Inside) \int_a^r \left(T_{\infty} + Q \ln b + \frac{Qk}{hb} \right) r dr - \int_a^r Q r \ln r dr \quad (13)$$

$$(Outside) \int_r^b \left(T_{\infty} + Q \ln a + \frac{Qk}{ha} \right) r dr + \int_r^b Q r \ln r dr \quad (14)$$

And integrating gives

$$(Inside) \left(T_{\infty} + Q \ln b + \frac{Qk}{hb} \right) \frac{(r^2 - a^2)}{2} - \frac{Q}{2} \ln \left(\frac{r^{r^2}}{a^{a^2}} \right) = \int_a^r r T r dr \quad (15)$$

$$(Outside) \left(T_{\infty} + Q \ln b + \frac{Qk}{ha} \right) \frac{(y^2 - x^2)}{2} + \frac{Q}{2} \ln \left(\frac{b^{b^2}}{r^{r^2}} \right) = \int_r^b r T r dr \quad (16)$$

Applying equation 13 and 14 to the equation 8 yields equation 17 and 18 which gives the radial stress in the cylinder as function of temperature and radius

$$\sigma_r(r)(Inside) = \frac{E}{1-\nu} \left[-\frac{\alpha}{r^2} \left[\left(T_{\infty} + \frac{q''a}{k} \ln b + \frac{\left(\frac{q''a}{k} \right) k}{hb} \right) \frac{(r^2 - a^2)}{2} - \frac{\left(\frac{q''a}{k} \right)}{2} \ln \left(\frac{r^{r^2}}{a^{a^2}} \right) \right] + \frac{(r^2 - a^2)\alpha}{r^2(b^2 - a^2)} \left[\left(T_{\infty} + \frac{q''a}{k} \ln b + \frac{\left(\frac{q''a}{k} \right) k}{hb} \right) \frac{(b^2 - a^2)}{2} - \frac{\left(\frac{q''a}{k} \right)}{2} \ln \left(\frac{a^{a^2}}{b^{b^2}} \right) \right] \right] \quad (17)$$

$$\sigma_r(r)(Outside) = \frac{E}{1-\nu} \left[-\frac{\alpha}{r^2} \left[\left(T_{\infty} + \frac{q''a}{k} \ln b + \frac{\left(\frac{q''b}{k} \right) k}{ha} \right) \frac{(b^2 - r^2)}{2} + \frac{\left(\frac{q''b}{k} \right)}{2} \ln \left(\frac{r^{r^2}}{b^{b^2}} \right) \right] + \frac{(r^2 - a^2)\alpha}{r^2(b^2 - a^2)} \left[\left(T_{\infty} + \frac{q''a}{k} \ln b + \frac{\left(\frac{q''a}{k} \right) k}{hb} \right) \frac{(b^2 - a^2)}{2} + \frac{\left(\frac{q''a}{k} \right)}{2} \ln \left(\frac{a^{a^2}}{b^{b^2}} \right) \right] \right] \quad (18)$$

Numerical Model

The numerical model was developed as a way to validate the results from the analytical model and explore the effects of interfacial heating. Pro-Engineer/Pro-Mechanica used to develop the numerical model. The numerical model was done by first creating a solid model of the target in the Pro-engineer modeling environment.

First a 2-D sketch of the cylinder layout was created in the sketcher window. Since there are multiple pieces in the target only one part is drawn at a time. An example of the sketch can be seen in figure 6.

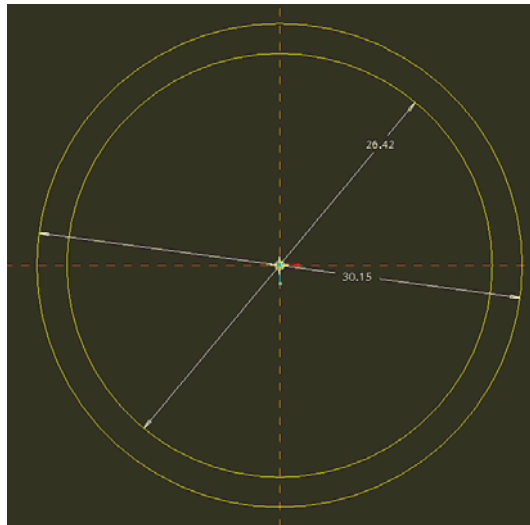


Figure 6. 2-D sketch of the cylinder ends

Next the 2-D object was extruded into a 3-D object, which is done using the extrusion tool. Completing the extrusion finishes the first piece of the cylinder. When the second part is done and saved the parts are ready for assembly. Combining the cylinders is done in an assembly drawing which is accessed the same way as a new part. An image of the assembled cylinders as a solid and wire frame model can be seen in figure 7.

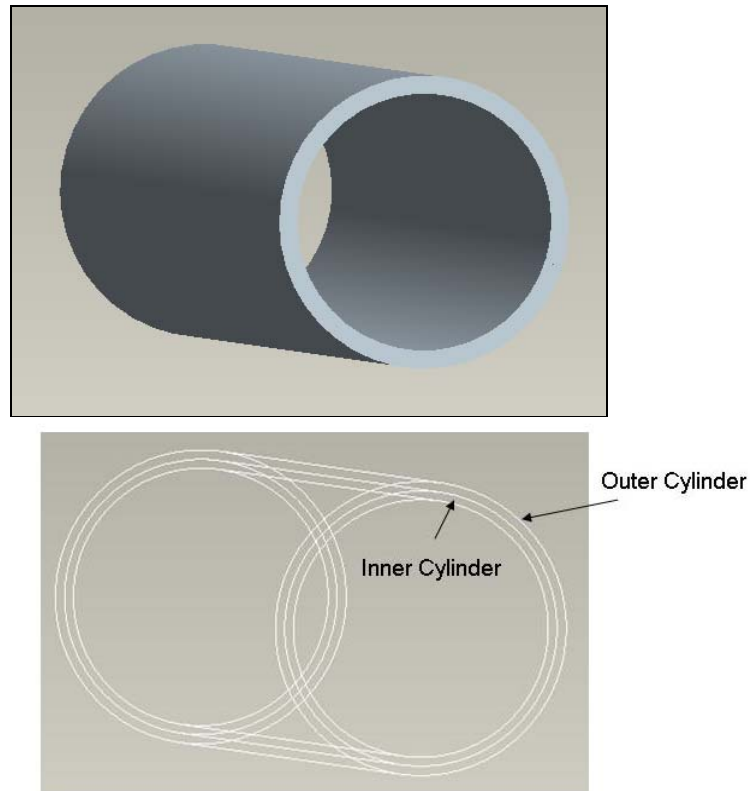


Figure 7. 3-D assembly of the combined cylinders as a solid and wire frame model

Performing a thermal-mechanical analysis in Pro-Mechanica requires a multiple step process which includes a thermal analysis, which will obtain the temperature distribution data, and a structural analysis which will find the effects of the temperature distribution. The thermal analysis was done in the thermal mode and the mechanical analysis was done in the structural mode.

Table 1 shows the boundary condition's location on the cylindrical target and the settings for the inside, outside and interfacial heating conditions.

Table 1. Location and boundary condition information for the thermal mode

| <i>Heating Condition</i> | <i>Inside</i> | <i>Outside</i> | <i>Interface</i> | <i>Cylinder Ends</i> |
|--------------------------|-----------------|-----------------|------------------|----------------------|
| Inside | 1,000,000 watts | h= 21740 @ 323K | N/A | Insulated |
| Outside | h=29306 @ 323K | 1,000,000 watts | N/A | Insulated |
| Interfacial | h=17522 @ 323k | h=17522 @ 323K | 1,000,000 watts | Insulated |

After applying the boundary conditions the automatic mesh generation settings were modified. The default settings were not sufficient enough for this analysis. Figure 8 shows what settings were changed and their new values.

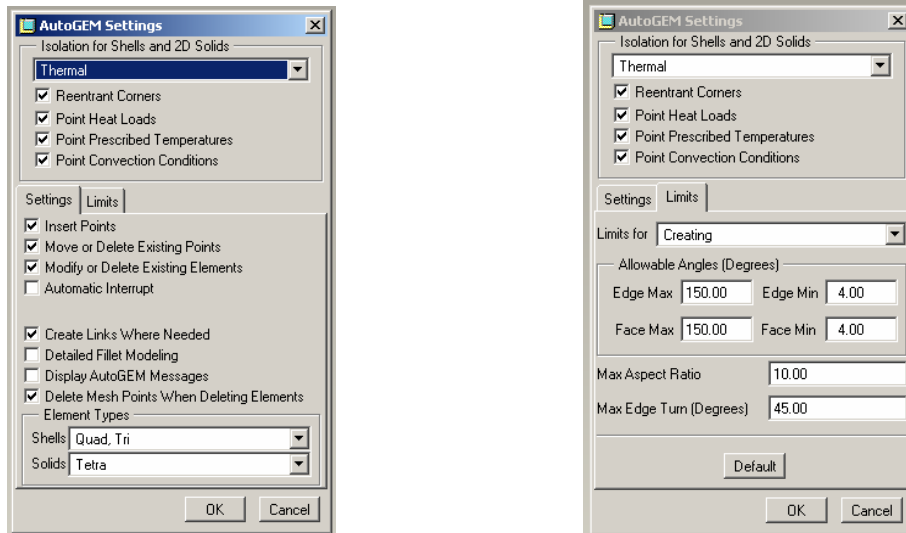


Figure 8. Automatic mesh generating settings

Aluminum 6061 was chosen as the reference targets material. The settings used during the steady state thermal analysis were single pass adaptive, a convergence percent of 0.001 and a reference temperature of 323K or 50°C.

The temperature distribution produced by the thermal analysis was then transferred to the structural mode. In the structural mode the temperature distribution was applied to the model using the MEC/T function. Next, the physical boundary conditions were applied to the model. A new polar coordinate system was created making the application of the boundary conditions much easier. Table 2 and figure 9 show the physical boundary conditions applied to the target. It should be noted that the physical boundary conditions were the same for all three heating conditions and that no rotation was allowed during the analysis. One of the target's ends is fully constrained because a FEA analysis will not run unless there is some amount of fixed constraint applied to the model

Table 2. Location and boundary condition information for the structural mode

| <i>Component</i> | <i>Inside Surface</i> | <i>Outside Surface</i> | <i>Interface</i> | <i>Cylinder End 1</i> | <i>Cylinder End 2</i> |
|------------------|-----------------------|------------------------|------------------|-----------------------|-----------------------|
| R | Free | Free | N/A | Free | Static |
| θ | Free | Free | N/A | Free | Static |
| Z | Free | Free | N/A | Free | Static |

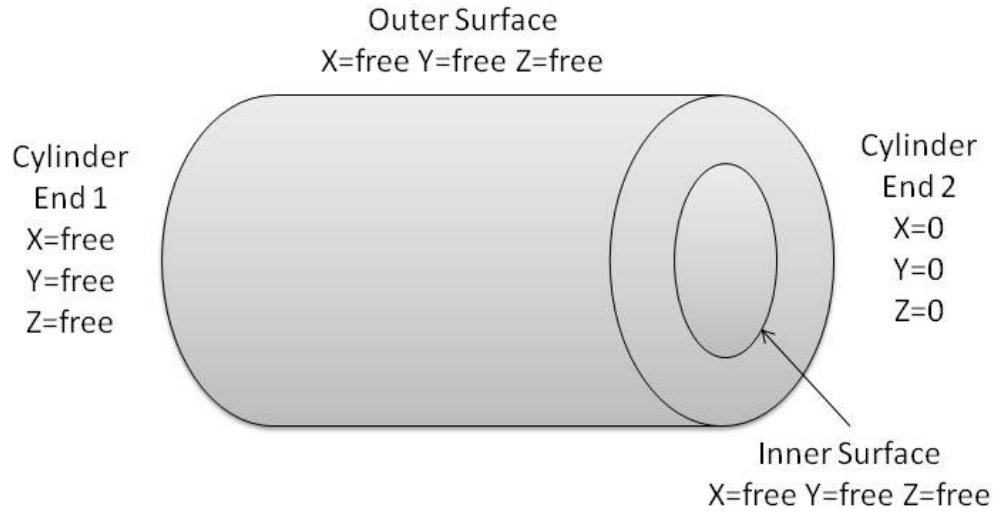


Figure 9. Physical boundary conditions applied to the target

After applying all of the boundary conditions a static analysis was performed to find the thermal mechanical behavior of the target. It should be noted that the mechanical properties were assumed to temperature independent. The settings used during the static analysis were multi pass adaptive with a poly order setting of min 1 and max 6 and a convergence percent setting of 0.001.

Chapter 4: Cylindrical Target Design Results and Discussion

Analytical Model

An analytic model of the cylindrical reference design was developed to investigate the thermal stresses that would form in the target which would be used to determine a correct testing methodology. The inside and outside surface heating conditions were investigated because they could be experimental tested. The end goal was to compare the results from these two conditions and validate their results against a numerical model which then would be used to investigate the interfacial heating condition.

The analytic model assumed that the two cylinders were perfectly bonded at their interface creating a single annular cylinder. The equations developed in chapter 3 were used to analyze the radial stress as a function of target thickness through the single annular cylinder. The target thickness is defined as the distance from the inside surface of the inner cylinder to the outside surface of the outer cylinder. The boundary conditions used in all models can be seen in table 3 and their positions on the target can be seen in figure 10.

Table 3. Model surface boundary conditions

| | <i>Inner Surface</i> | <i>Interfacial Surface</i> | <i>Outer Surface</i> | <i>Cylinder Ends</i> |
|--------------------------------------|-----------------------------------|----------------------------|-----------------------------------|-------------------------------|
| Inner Heating Condition | $q''=100 \text{ W/cm}^2$ | N/A | $h=21740 \text{ W/m}^2 \text{ K}$ | $h=0 \text{ W/m}^2 \text{ K}$ |
| Interfacial Heating Condition | $h=17522 \text{ W/m}^2 \text{ K}$ | $q''=100 \text{ W/cm}^2$ | $h=17522 \text{ W/m}^2 \text{ K}$ | $h=0 \text{ W/m}^2 \text{ K}$ |
| Outer Heating Condition | $h=29305 \text{ W/m}^2 \text{ K}$ | N/A | $q''=100 \text{ W/cm}^2$ | $h=0 \text{ W/m}^2 \text{ K}$ |

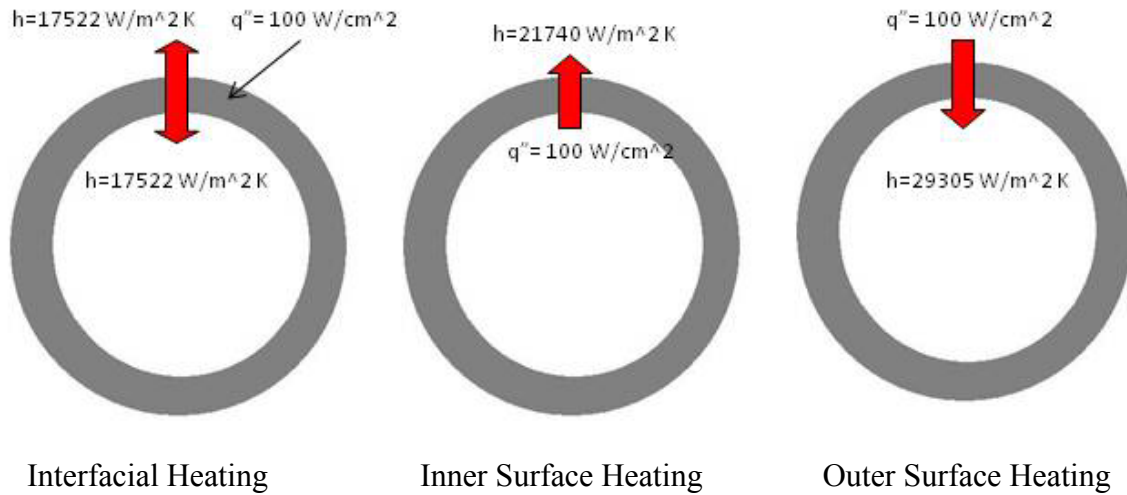


Figure 10. Cut away diagram of the three different heating situations

The temperatures as a function of radius can be seen in figure 11 and the radial stress as function of the radius can be seen in figure 12. The Matlab code used to produce the plots can be seen in Appendix 1 section A and B.

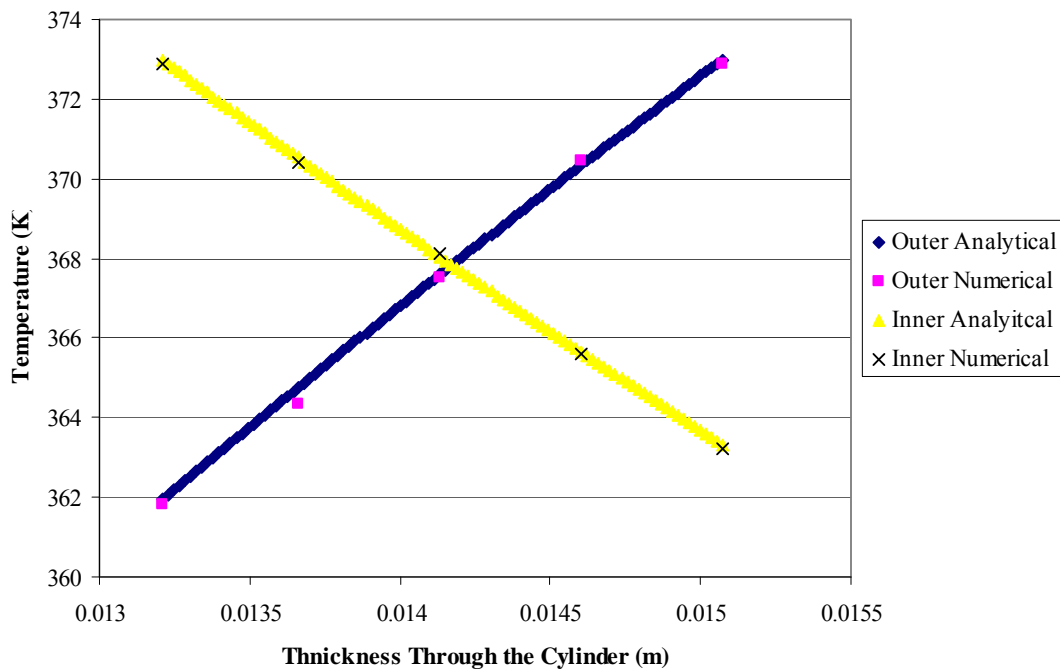


Figure 11. Temperature as function of radius

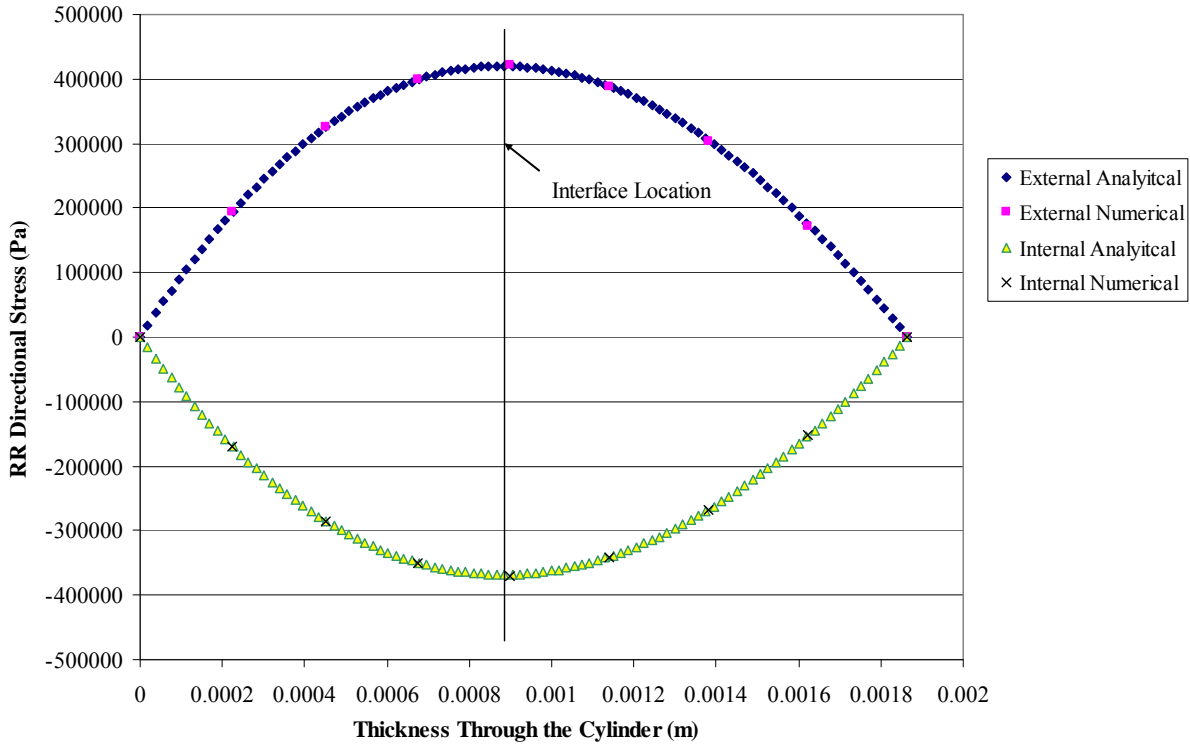


Figure 12. Radial stress as a function of target thickness for the outside and inside surface heating condition with interface location

The results show that the radial stress at the surfaces for both conditions is zero and that as the interface of the cylinders is approached there is an increase in the absolute radial stress. A negative radial stress represents a compression force while a positive radial stress implies a tensile force. A compressive force at the interface implies that there will be an increase in the interfacial pressure due to interior heating which will decrease the thermal contact resistance.

In a pair of concentric cylinders that do not have a bonded interface. A tensile force would imply that the cylinder surfaces will have the tendency to separate from each other. A separation of the surfaces from a thermal perspective will increase the thermal contact resistance. It should be noted that if a gap were to occur at the interface the radial stress at the interface would become zero.

The data from the two heating conditions should have been symmetric however this is not the case. The results for the external surface heating have an absolute value greater than the absolute value of the internal surface heating condition. Different surface areas of the inner and outer cylinder surfaces are the reason the trends are not symmetric. The different surface areas affect the amount of energy that is expelled by the target creating different temperature gradients. The temperature gradients are what drive the expansion and stress in the target thus different gradients will produce different stress values.

Numerical model

The goal of the numerical model was to validate the analytical model and explore interfacial heating as seen in the real target. Contour plots from Pro-Mechanica of the radial temperature distribution at a given cylinder cross-section for the inner and outer surface heating conditions can be seen in figures 13 and 14. A summary of the temperatures including the interfacial heating condition is provided in table 4.

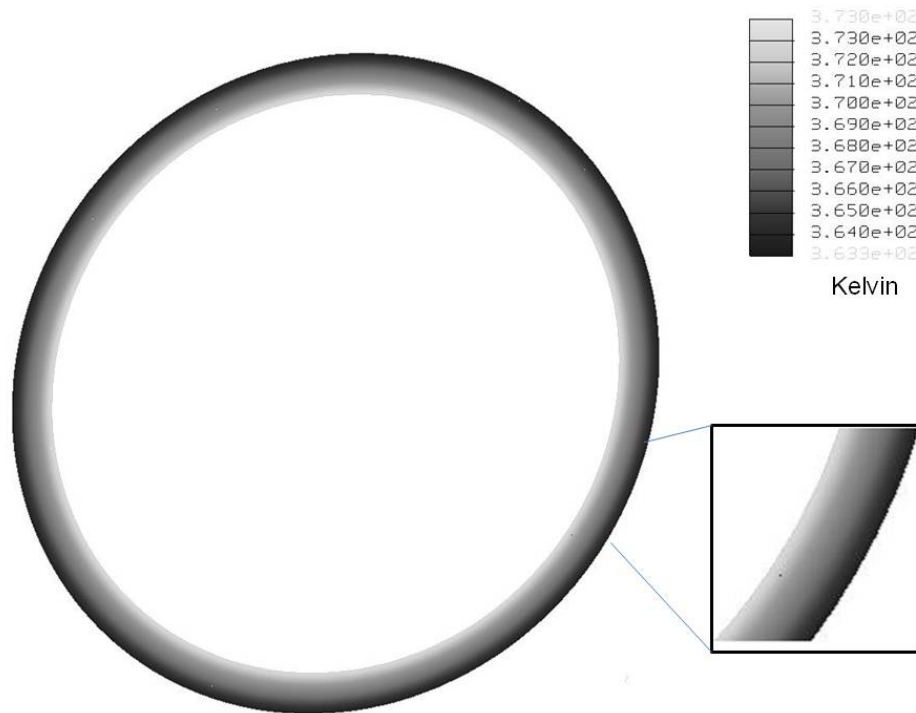


Figure 13. Temperature distribution of the interior surface heating condition

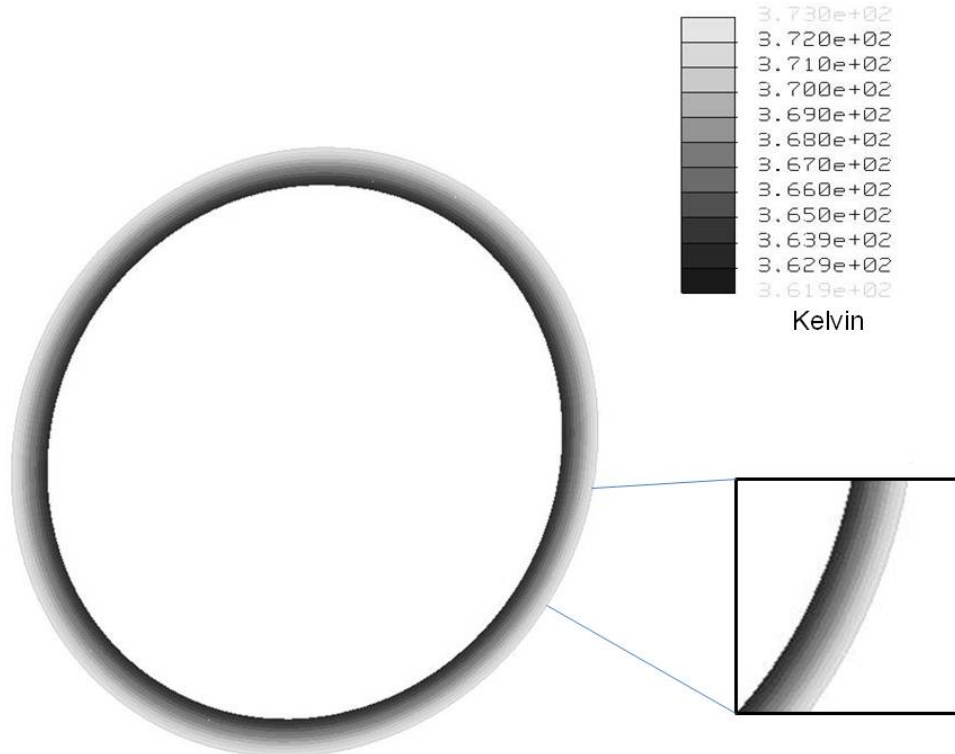


Figure 14. Temperature distribution of the outer surface heating condition

Table 4. Model surface temperature results

| | <i>Inner Surface</i> | <i>Interfacial Surface</i> | <i>Outer Surface</i> | <i>Cylinder Ends</i> |
|--------------------------------------|----------------------|----------------------------|----------------------|----------------------|
| Inner Heating Condition | 99° C | 96° C | 91° C | N/A |
| Interfacial Heating Condition | 79° C | 81° C | 77° C | N/A |
| Outer Heating Condition | 90° C | 94° C | 99° C | N/A |

The temperature distribution data was transferred from the thermal mode into the structural mode within Pro-Mechanica. The structural mode was used to find the mechanical deformation and stress due to thermal expansion.

The radial stress distribution for the inner and outer surface heating can be seen in figures 15 and 16 respectively.

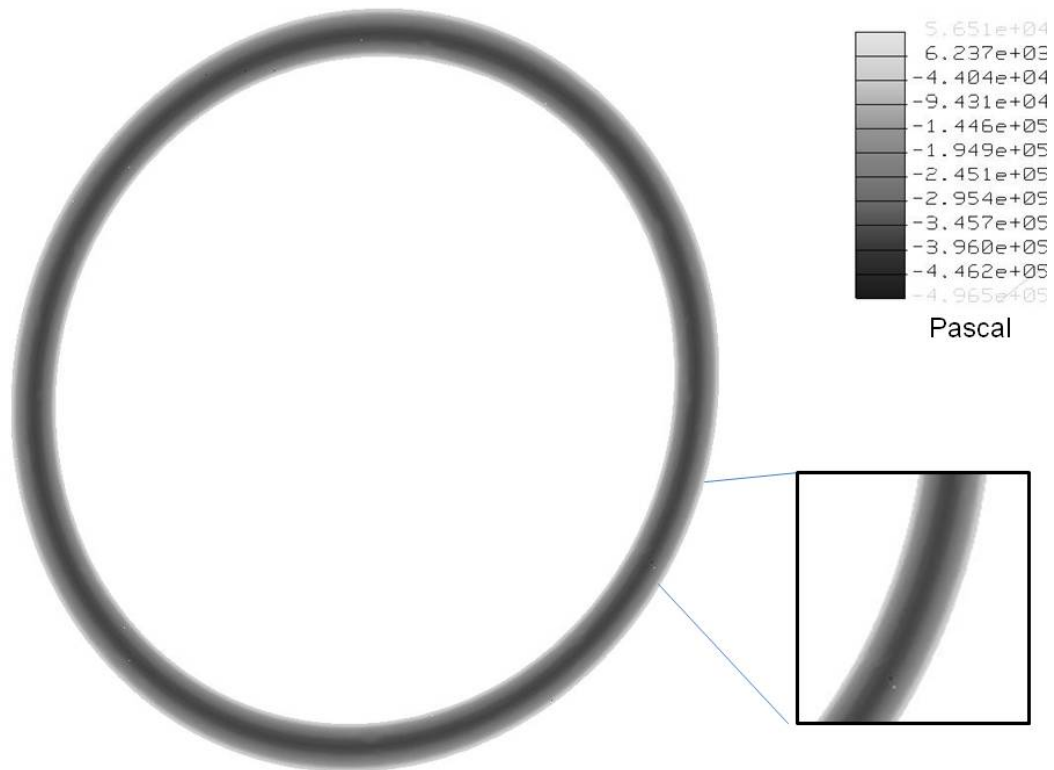


Figure 15. Radial stress distribution for inner surface heating

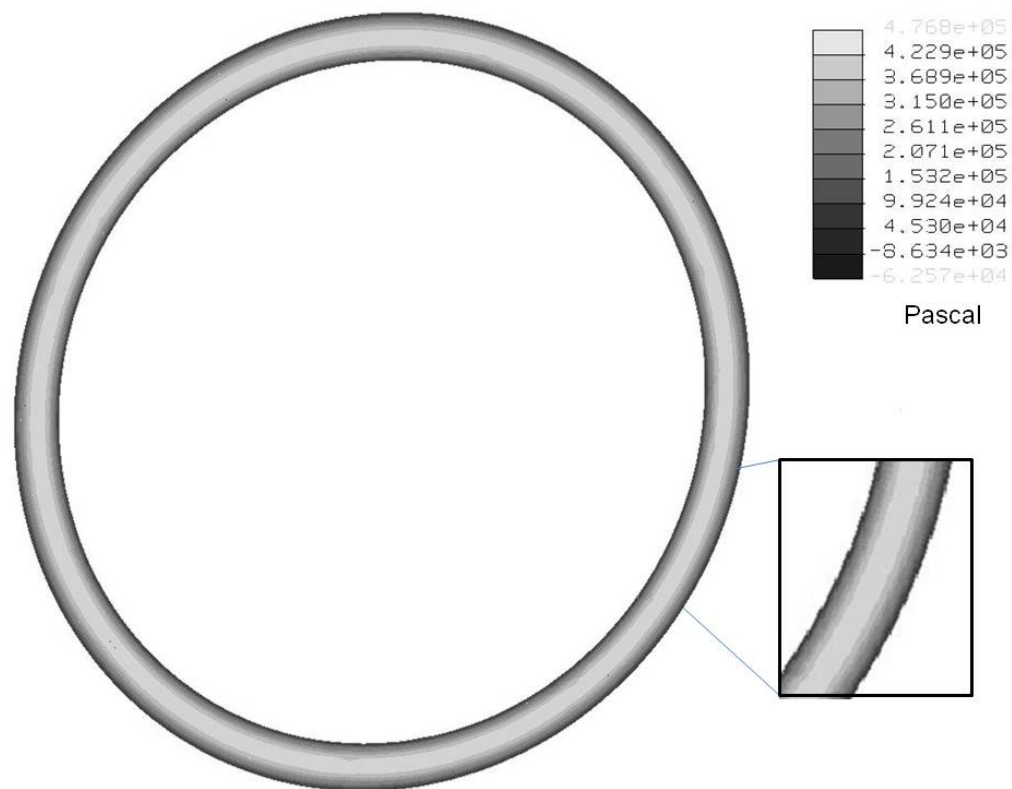


Figure 16. Radial stress distribution for outer surface heating

A comparison of the thermal and mechanical results from the analytic and numeric models is shown in tables 5 and 6 and figure 12.

Table 5. Inner surface heating condition comparison with percent difference

| <i>Thickness Distance (mm)</i> | <i>Analytical Results (Pa)</i> | <i>Numerical Results (Pa)</i> | <i>Percent Difference(%)</i> |
|------------------------------------|------------------------------------|-----------------------------------|----------------------------------|
| 0 | 0 | 0 | 0 |
| 0.225 | -169356 | -182036 | 7.5 |
| 0.45 | -284604 | -285702 | 0.4 |
| 0.675 | -349380 | -350266 | 0.3 |
| 0.9 | -369908 | -368026 | 0.5 |
| 1.14 | -342367 | -338638 | 1.1 |
| 1.38 | -367512 | -270162 | 1.0 |
| 1.62 | -151155 | -154787 | 2.4 |
| 1.87 | 0 | 0 | 0 |

Table 6. Outer surface heating condition comparison with percent difference

| <i>Thickness Distance (mm)</i> | <i>Analytical Results (Pa)</i> | <i>Numerical Results (Pa)</i> | <i>Percent Difference (%)</i> |
|------------------------------------|------------------------------------|-----------------------------------|-----------------------------------|
| 0 | 0 | 0 | 0 |
| 0.225 | 207736 | 193556 | 7.3 |
| 0.45 | 326037 | 325107 | 0.3 |
| 0.675 | 399716 | 398889 | 0.2 |
| 0.9 | 419984 | 422121 | 0.5 |
| 1.14 | 386447 | 388771 | 0.6 |
| 1.38 | 308303 | 303592 | 1.6 |
| 1.62 | 176640 | 172328 | 2.5 |
| 1.87 | 0 | 0 | 0 |

The percent difference between all of the compared values is below ten percent and even smaller at the location of the interface. The similar results between the models provide the confidence to use the numerical model to evaluate interfacial heating.

The radial stress as a function the target's thickness was not the only radial stresses investigated. The radial stress along the length of the bonded cylinder interface in figure 17 was also investigated.

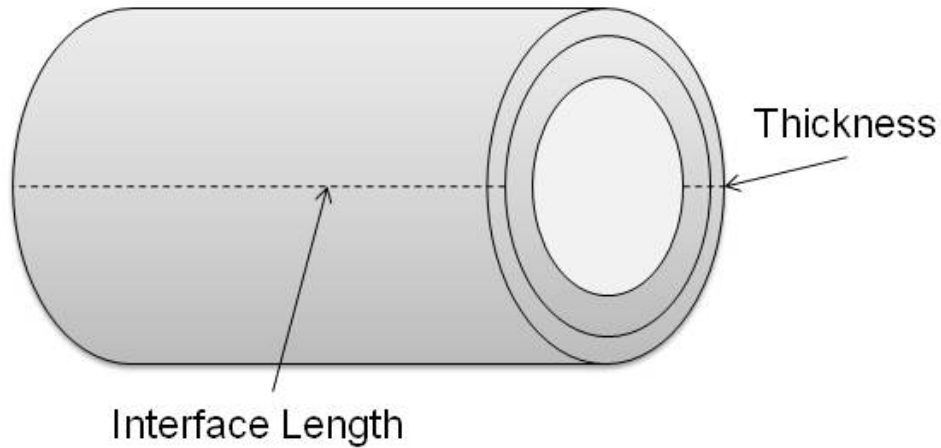


Figure 17. Location of the interface length

The results in figure 18 show the radial stress along the length of the cylinder's interface. Examination of the plot shows that there are many data points that are within the same range of each other and that the stress is constant until about 0.13 m along the interface. The deviation is caused by the fully constrained boundary condition that was necessary for numeric convergence.

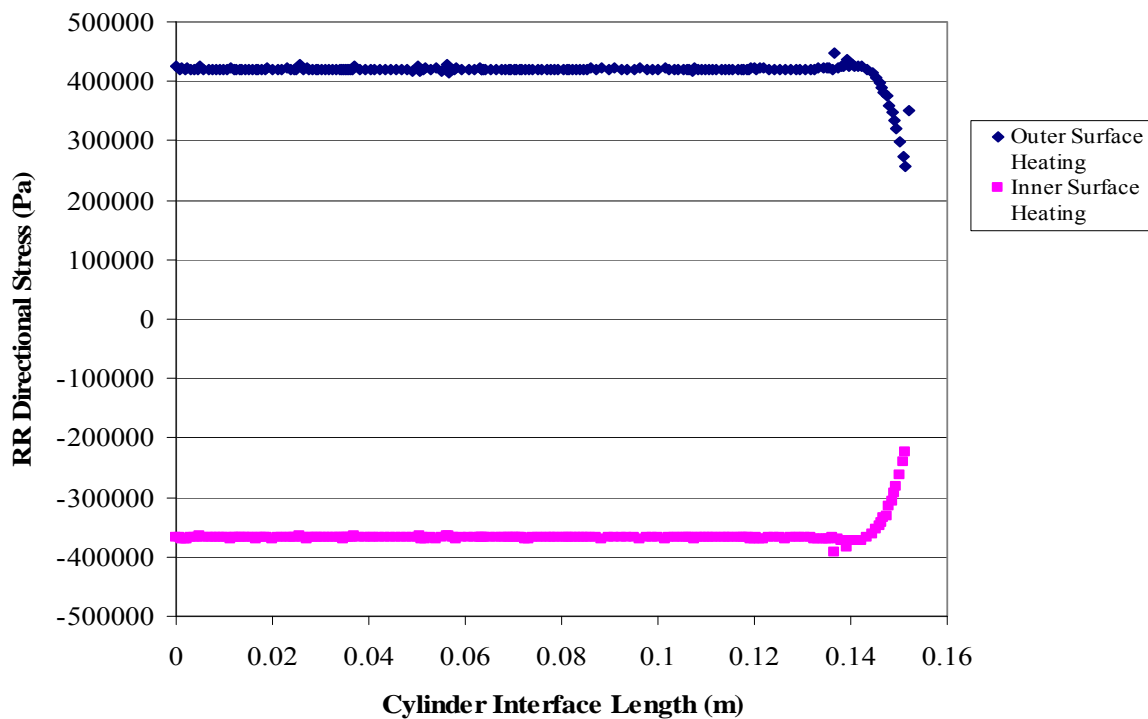


Figure 18. Plot of the stresses in the radial direction at the interface for inside and outside surface heating

Averaging the data from for the inner and outer surface heating gives the values seen in table 7. The slight fluctuations in the plot along the length are caused by a standard of deviation in the analysis. It should be noted that the models were all run at near the computing capacity of the computers available in the lab. A comparison of analytical and numerical inner and outer surface heating interface results again adds confidence to the models.

Table 7. Comparison of stress at the interface location

| | <i>Inside Surface Heating</i> | <i>Outside Surface Heating</i> |
|-------------------------------|-------------------------------|--------------------------------|
| Analytical | -368101 Pa | 420069 Pa |
| Numerical | -368024 Pa | 420525 Pa |
| Percent Difference (%) | 0.02 | 0.1 |

Interfacial Heating

Recall that the primary goal of the numerical study is to provide direction in establishing a measurement methodology for the next phase of the target development. This means the interfacial heating must be compared to the inner and outer heating experimental configurations. Figure 19 compares the temperature distributions of the inner, interfacial and outer heating conditions and figure 20 gives the numeric temperature contour plot. A plot of the radial stresses as a function of the target thickness compared to the inner and outer surface heating can be seen in figure 21 and the interfacial heating stress contour plot can be seen in figure 22.

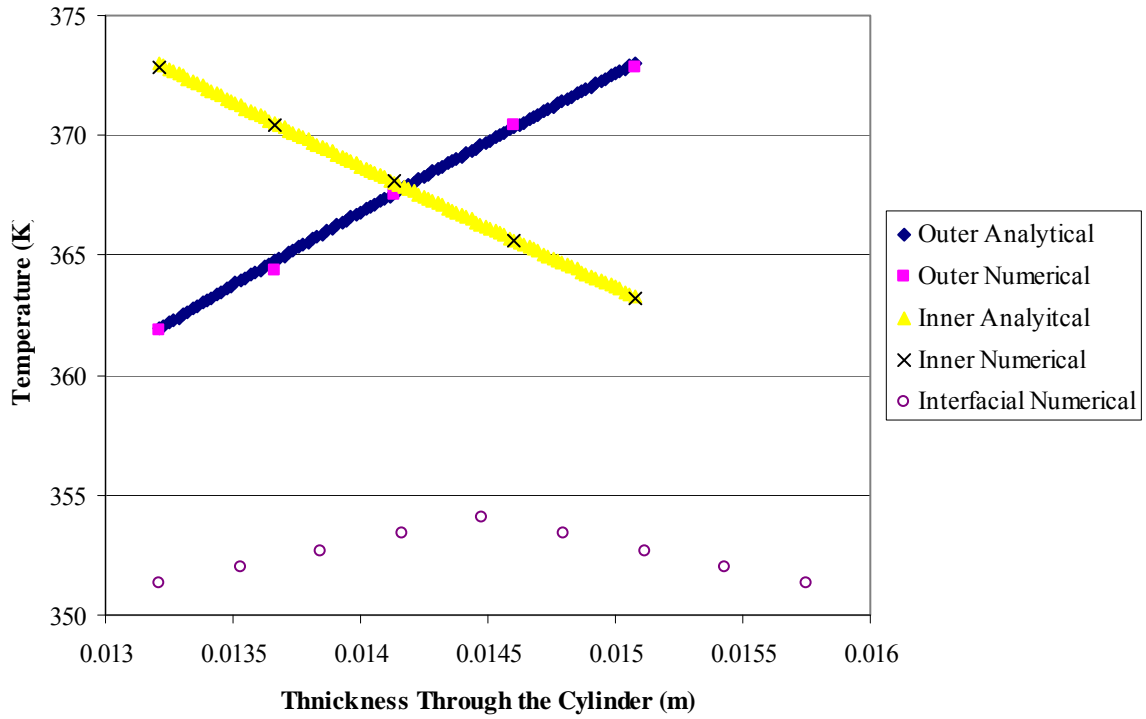


Figure 19. Temperature distribution as function of radius for the inner, interfacial and outer heating conditions

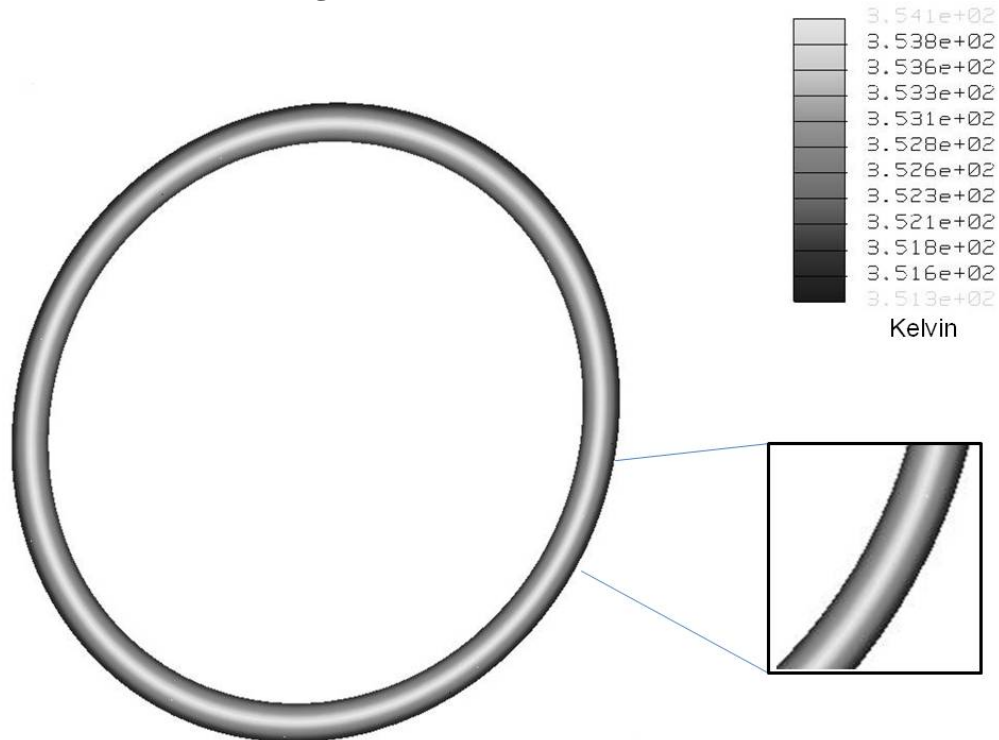


Figure 20. Temperature distribution of the interfacial heating condition

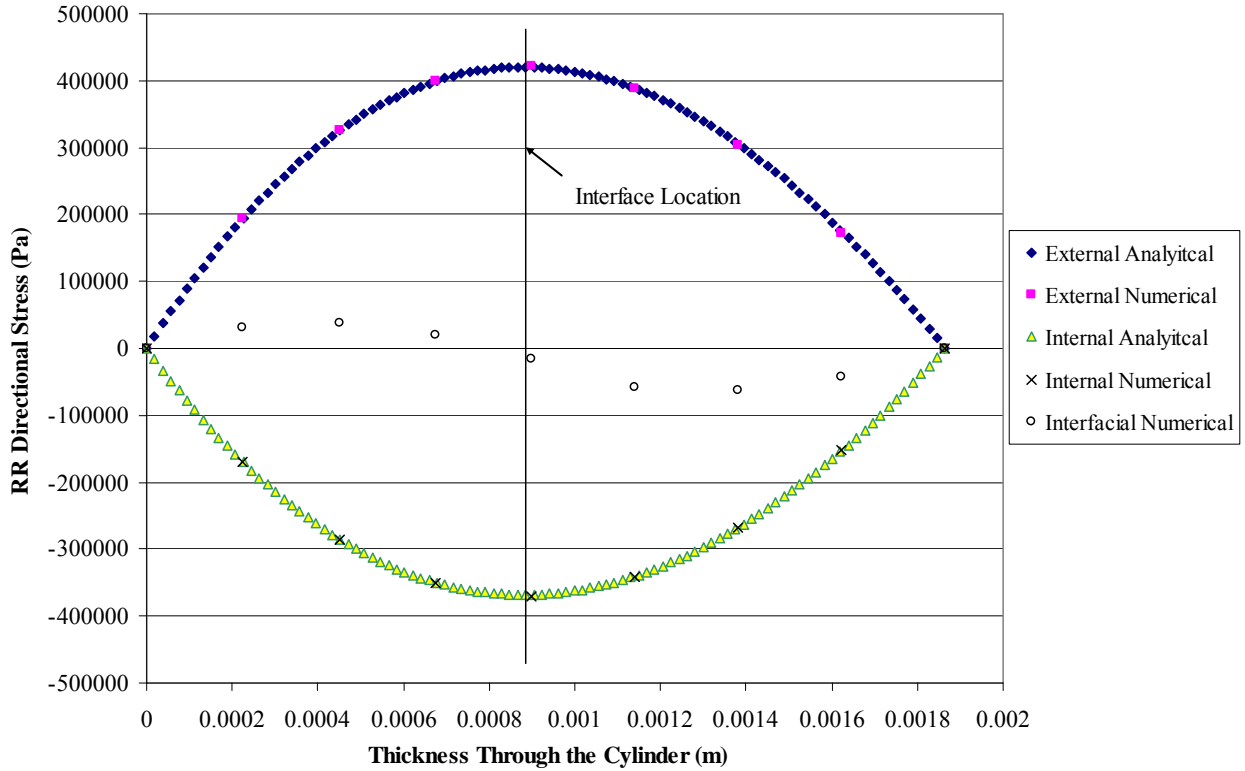


Figure 21. Radial stress as a function of target thickness for the interfacial heating condition

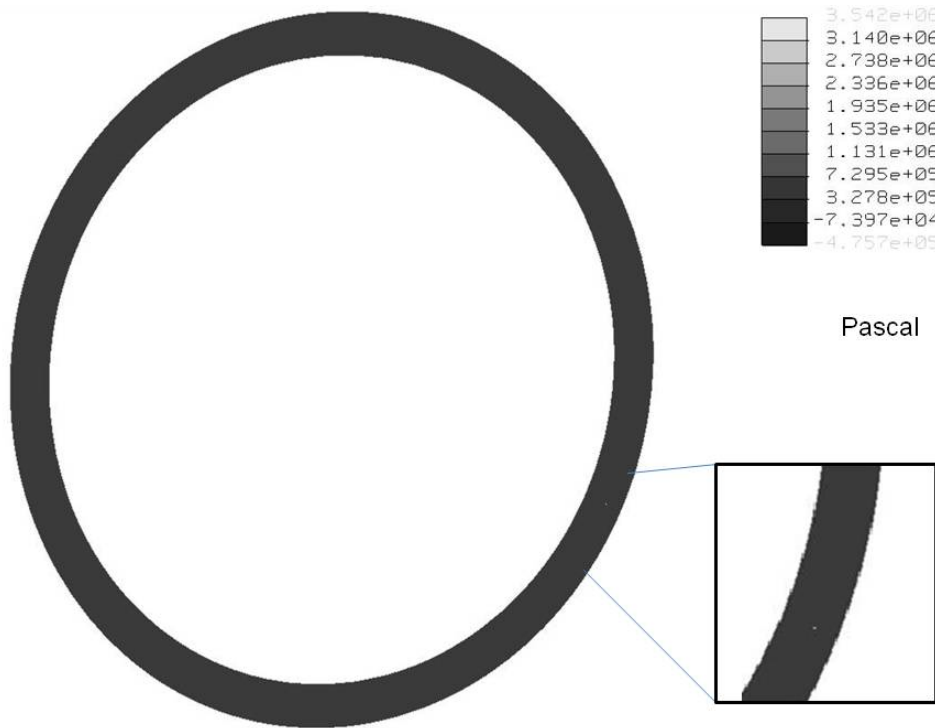


Figure 22. Radial stress distribution for interfacial heating

Figure 19 shows that the interfacial heating condition produces a much different temperature distribution than either the inner and outer surface heating cases. The distribution is slightly higher on the inner surface because this surface area is smaller than the outer surface. Figure 21 shows that the interfacial radial stress is zero at the inner and outer surfaces. However, unlike the inner and outer heating cases, there is an interior point at which the stress is zero. The stress located between the inner surface and the zero point is a positive tensile stress and the stress from this point to the outer surface is a negative compressive stress.

The three heating condition results clearly show that the outside surface heating condition produces the greatest amount of tension at the cylinder interface. The tensile force will correspond to an increase in the thermal contact resistance and a reduction in the contact pressure. When the inner heating and the interfacial heating stresses are compared, it is clear that the inner heating condition will put the cylinder interface in an overly optimistic state. If it is found that the target can survive a tensile force from an external applied heat load then the target should be able to survive the interfacial heating condition produced by the LEU during irradiation in the reactor.

Chapter 5: Plate Target Design Modeling

There is no known systematic study that has been completed on a plate target geometry based on a removable LEU foil. Studies have been completed on U-10Mo foil in a plate configuration used as fuel (Rest, Hofman, Konovalov, and Maslov, 1998). However the U-10Mo fuel target is designed to produce bonding between the aluminum cladding and the LEU foil which would be difficult to separate post irradiation. The goal of the current study is to evaluate the thermal contact resistance and mechanical stresses for a plate that can be used to produce molybdenum-99. Numeric and experimental studies are completed to provide an initial assessment of the plate geometry and to provide tools for further analysis.

Analytical Model

A preliminary analytical model was developed to explore the effects of a temperature gradient on a simple structure and to give insight into natural plate bending behavior. The model (Boley and Weiner, 1960) assumed a uniform thermal load applied over the entire plate surface, no edges were welded and the plate was infinitely long. Consider the beam in figure 23 with a thickness of $2h$, a length (L) and a unit length of (b) where L is much larger than h . The temperature is only a function of the depth (z) where $T=T(z)$ creating a one dimensional temperature distribution. The plate is assumed to be simply supported.

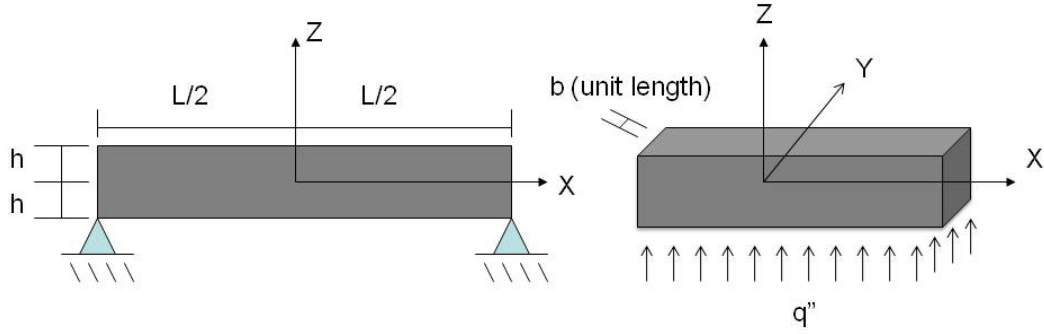


Figure 23. Analytical model assumed infinitely long in the Y direction and no weld on the edges

Using the previously made assumptions it is reasonable to assume that the stresses in the beam will be as follows $\sigma_{zz} = \sigma_{xz} = \sigma_{yz} = \sigma_{zy} = 0$ and $\sigma_{xx} = \sigma_{yy} = f(z)$. The stresses that are a function of z can be expressed by equation 19.

$$\sigma_{xx} = \sigma_{yy} = -\alpha ET + C_1 + C_2 x \quad (19)$$

The constants C_1 and C_2 are determined by σ_{xx} equals zero at the edges of the plate,

thus $\sigma_{xx}(z) = 0$. Applying this to equation 19 gives equation 20.

$$\sigma_{xx} = \alpha E \left[-T + \frac{1}{2h} \int_{-h}^h T dz + \frac{3z}{2h^3} \int_{-h}^h T z dz \right] \quad (20)$$

Simplifying and assuming that $z = \pm h$ gives stress along the x-axis

$$\sigma_{xx} = -\alpha ET + \frac{(bN_T)}{A} + \frac{z(bM_T)}{I} \quad (21)$$

where $A=2bh$, $I = \frac{2h^3 b}{3}$, $N_T = \alpha E \int_{-h}^h T dz$, and $M_T = \alpha E \int_{-h}^h T z dz$. Applying the thermo elastic stress-strain relationships the strain in the ZZ direction is equal to equation 22.

$$\varepsilon_{zz} = -\frac{\nu}{E} \left(\frac{(bN_T)}{A} + \frac{z(bM_T)}{I} \right) + \alpha T \left(\frac{1+\nu}{E} \right) \quad (22)$$

Finally, equation 22 is used with the strain-displacement relationships to produce equation 23.

$$w = -\frac{(bM_T)}{2EI}x^2 - \frac{\nu}{E}\left[\frac{(bN_T)}{A}z + \frac{z^2}{2I}(bM_T)\right] + \alpha\left(\frac{1+\nu}{E}\right)\int_0^z Tdz \quad (23)$$

Equation 23 can be used to find the Z axis displacement at any point through the thickness of the beam and at any point along its length (Boley and Weiner, 1960).

Numerical Model

A numerical model of the plate target was developed to explore the effects of internal heating on the thermal contact resistance for the plate geometry. In the cylindrical target numerical model, Pro-Engineer / Pro-Mechanica was used to produce the simple contact conditions in the target i.e. a bonded contact condition. The complex contact conditions in the plate target could not be simulated in Pro-Engineer / Pro-Mechanica thus a new modeling and analysis software package was found. Algor was chosen for the plate target because it could simulate the proper contact conditions and produce a finer mesh with much greater ease. The following procedure is a summary of a full procedure which can be found in appendix 2.

Modeling and analysis in Algor is similar to the process used in Pro-Mechanica. The geometry used in Algor was created in Inventor which was used to produced a model that had the length and width dimensions of the plate. The thickness of the plate is not important at this juncture since this will later be specified in Algor. The Inventor geometry was then transferred into Algor and an initial rough mesh was created. The purpose of the rough mesh was to produce selection points for the creation of a two-dimensional four point mesh. The four-point mesh method can be used to create a perfectly symmetric mesh. When completed the four point mesh creates a single surface that is the length and width of the completed plate target. The single surface must be

broken into two different surfaces to apply the thermal load to appropriate interior surface area. Breaking the large surface into two distinct surfaces is done by modifying the attributes of the selected mesh lines.

Extruding the two-dimensional mesh into a three dimensional mesh was done by copying the existing mesh and moving it in the Z direction the thickness of a single plate. During this procedure the two meshes are joined to each other by mesh elements which create a three dimensional object representing a single plate. Repeating the copying and move process in the opposite Z direction produces the other plate in the target. An image of the completed mesh can be seen in figure 25.

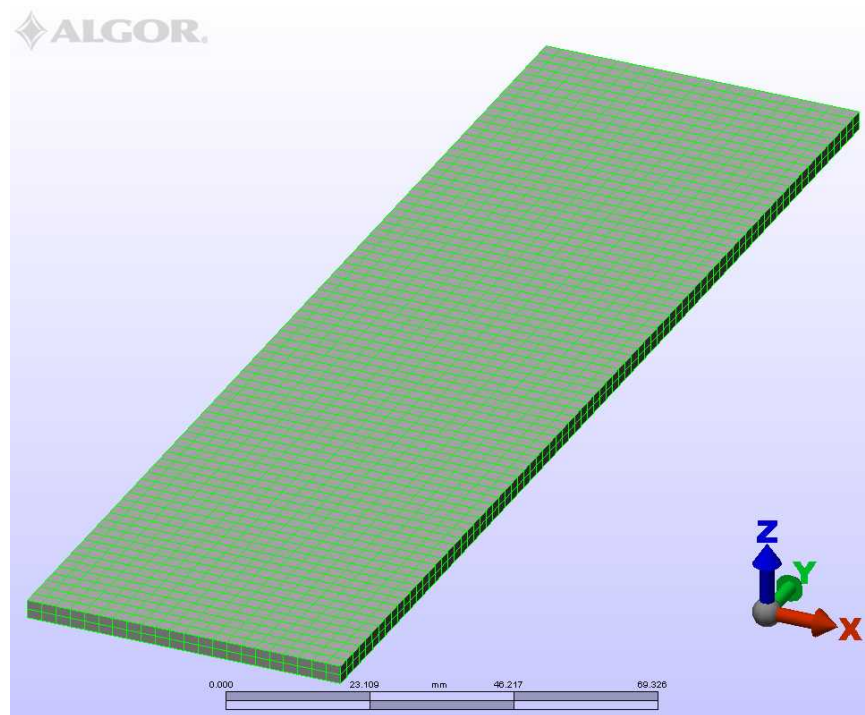


Figure 24. Completed plate target mesh in Algor

Analyzing the effects of the thermal load on the plate target was done in much of the same way as the annular target. First thermal boundary conditions were applied including the internal heat flux and the external convection coefficient. The global contact

condition for the static stress study was set to surface contact, which meant that the two surfaces could only move away from each other and not move into each other. The edges of the plates were set to welded meaning that they are only bonded at the point where they are in contact. A static stress analysis with linear materials was used to find the mechanical effects of the thermal load on the target. The temperature distribution data was applied to the model using the analysis parameters. Examples of the completed thermal and structural models with their boundary conditions can be seen in figures 25 and 26.

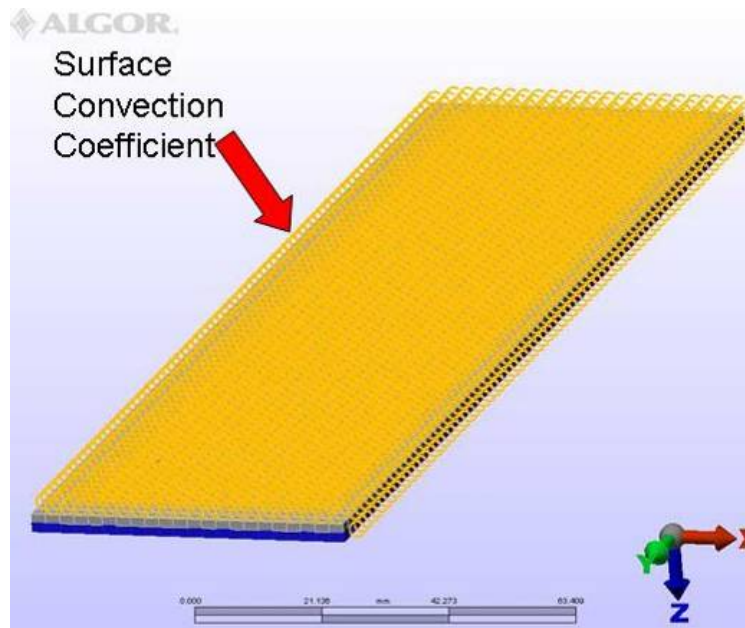


Figure 25. Plate Target model in the thermal analysis

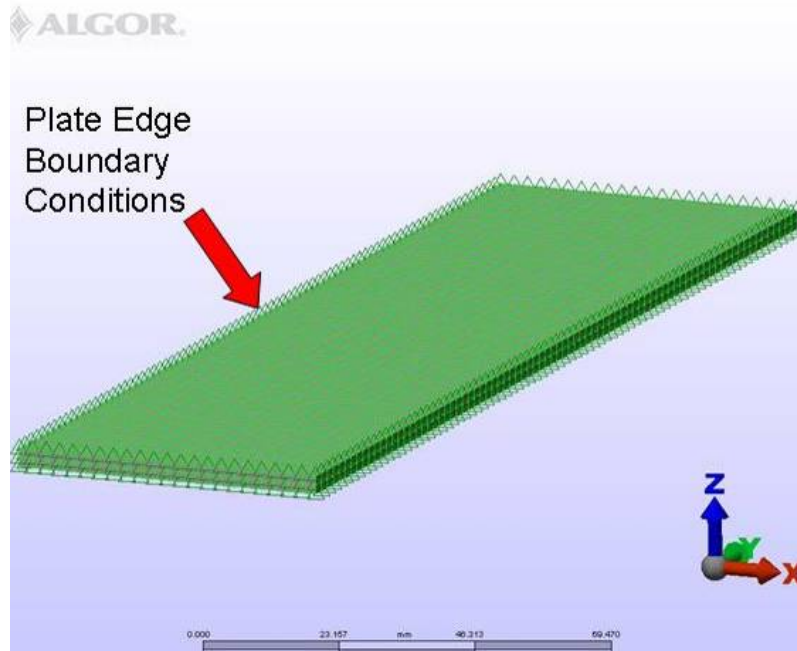


Figure 26. Plate Target model in the structural analysis

A parametric study was done using the previously outlined procedure. The study examined the effects of varying external heat transfer coefficient, internal heat flux, thickness of the individual aluminum plates, internal fission gas pressure and the plate target edge boundary conditions.

Experimental setup

The aim of the experimental test plate was provide initial evidence of pillowing due to thermal deformation and to validate the plate numerical model. In the reactor 30 kW could be generated during the fission of the LEU. However current laboratory electric service limits the maximum electric heater power to 5 kW. A heater placed between aluminum plates was used to simulate the LEU heat source. The aluminum plates were welded on three edges and a portion of the fourth edge. Heating the plate target internally without adversely affecting the behavior of the plates during testing created one of the greatest challenges in the development of the experimental setup.

A search began for a commercial heater that was nearly as thin as the LEU foil and able to deliver 5 kW of energy. The conclusion of the search found that a useable commercial heater did not exist and that a custom heater would need to be created. Tungsten wire with a diameter of 0.005” or 0.127 mm was initially chosen as the resistive heating element. Electrical shorting between the tungsten and the aluminum plates was prevented by placing the wire between Kapton film. The Kapton film was chosen because of its high operating temperature of 400 °C, its dielectric properties (500 volts for every 0.001”) and high thermal conductivity (0.12 W/mK) relative to other plastics. The materials were combined and a heater was created for testing. Initial shake down testing found that under an electric load the tungsten wire would burn out and fail. Upon examination it was noticed that the Kapton around the wire had melted causing an electrical short and oxidation of the wire. An example of a burnt out heater can be seen in figure 27.

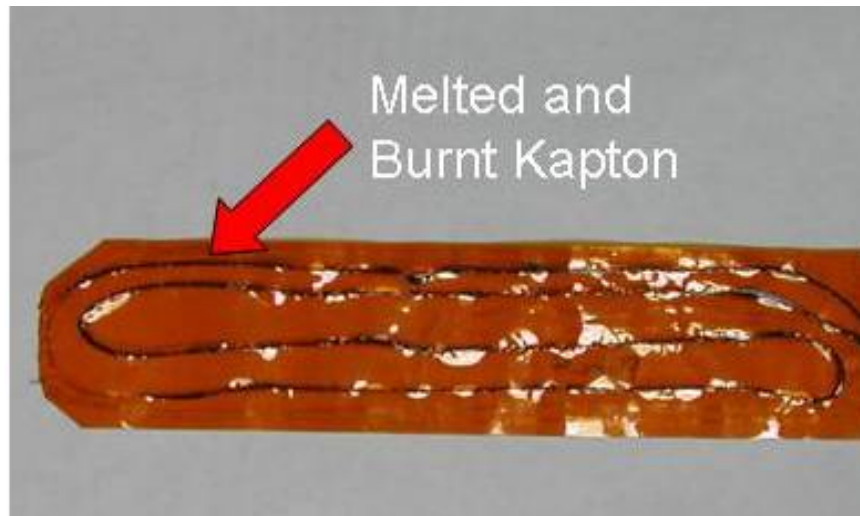


Figure 27. Heater that has experienced burnout

The melting of the Kapton occurred because of the inability of the tungsten wire to spread the heat flux effectively. Oxidation occurred because of the tungsten's reaction with air pockets in the heater.

In an effort to counteract these problems a nickel chrome wire with a diameter of 0.255 mm consisting of 80% nickel and 20% chrome was chosen to replace the tungsten wire. The Ni80 wire had several advantages compared to the tungsten wire. One was that it had a larger surface area than the tungsten wire thus it could spread the heat flux over a larger area. Another was that the Ni80 alloy is highly resistant to oxidation. A heater was again constructed and tested several times producing an increase in the energy input. Burnout again prevented the heaters from reaching 5 kW. Examination of the failed heaters showed that some of the heaters failed due to the internal melting of the Kapton and others failed when the external power and data wire leads shorted with the cooling water. An example of an external lead failure can be seen in figure 28.

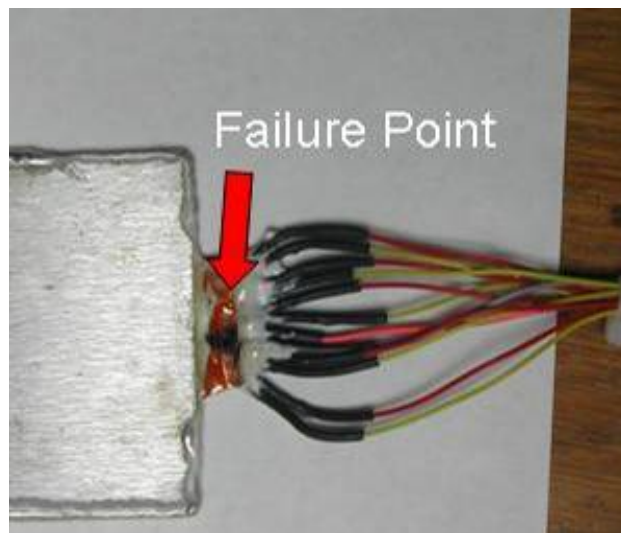


Figure 28. External connection point heater failure

The next set of heaters used several techniques to counteract the Ni80 wire failure mechanisms. First the Ni80 wire was flattened using a press to help increase the surface

area of the wire and increase heat spreading. Next, thin slices of aluminum foil were placed on the external wire leads which helped spread the heat over broader area thus helping prevent external burnout. An example of a used heater with the flattened wire and the aluminum foil heat spreaders can be seen in figure 29.

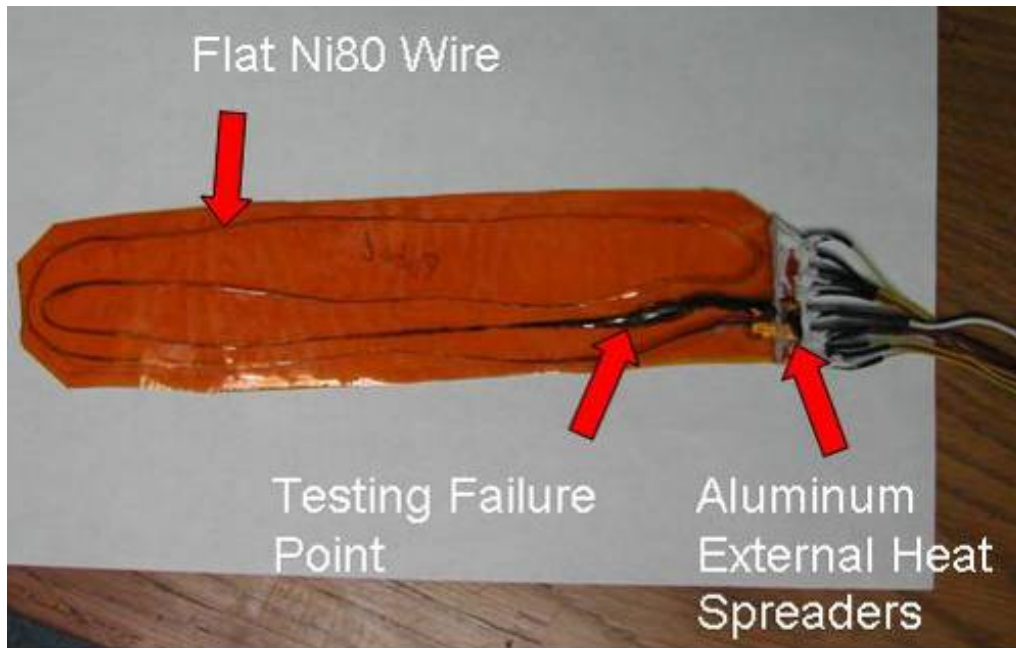


Figure 29. Heater with flattened wire and aluminum foil heat spreaders

The new techniques were applied to the heaters tested. The improved design saw an increase in the input energy up to 2.4 kW still short of the maximum allowable of 5 kW. The heater wire failed inside of the target because of divots in the wire that were created during the pressing process. Initial pressing of the wire was done using a press that could only process about an inch of wire per run. This process created divots in the wire. When placed in between the Kapton the divots would form air pockets that would reduce the thermal conductance between the wire and Kapton thus leading to burnout. In an effort to rid the wire of the divots, pre-made wire sets were made and sent to Y-12 where they

have a 100 ton press large enough process all of the wire at once. They have not been returned to this date.

A 240V electrical energy source located in the laboratory was chosen as the voltage source for the heater. The 240 V source was connected to the heater through a variac which was used to control the voltage input into the heater. The return wire was then connected to shunt resistor which was used to measure current. A diagram of the power source and heater can be seen in figure 30.

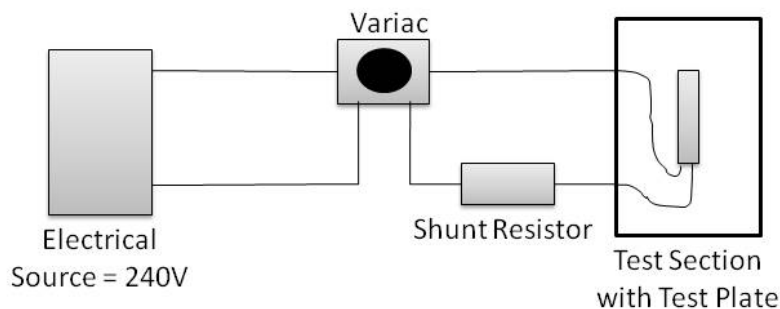


Figure 30. Diagram of electrical power source and heater

Temperature measurements from thermocouples placed near the heater wire in the Kapton film were the main technique used to detect separation in the target. The thermocouples used were bare wire type K thermocouples with a wire diameter of 0.003". A spike in the temperature indicates a reduction in thermal conduction, which likely means that the plates are separating from the heater.

Five thermocouples were placed inside the heater; their locations included the four corners and the center of the heater near the heater wire. An example of a finished heater before placing it between aluminum plates can be seen in figure 31 along with the thermocouple locations and an outline of the heating wire.

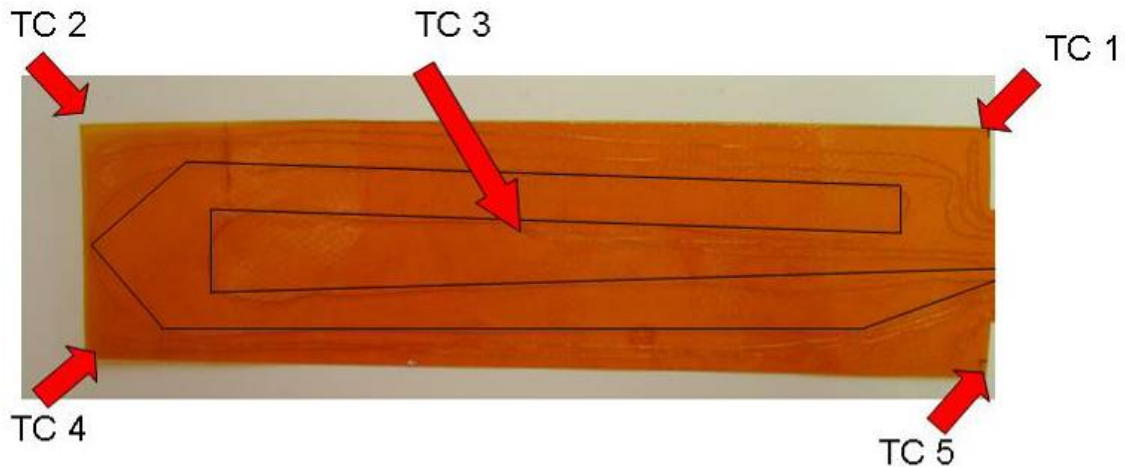


Figure 31. Heater with Thermocouple locations and heating wire outline

The thermocouples and power input wiring were covered with heat shrink which were then expoyed into place after soldering the lead wires. The Kapton encased heater was placed between two aluminum plates. The plates were clamped together using vice grips before they were TIG welded on three edges. A portion of the fourth edge was welded around thermocouple and power wire opening. Figure 32 shows an example of the electrical connections and the methods used to support them.

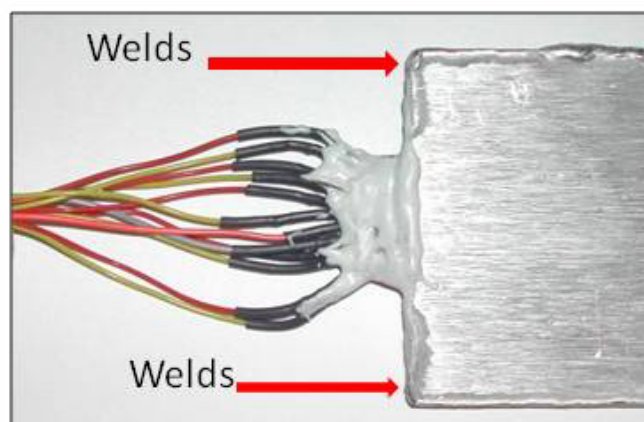


Figure 32. Electrical connections

A fully assembled example of the test plate can be seen in figure 33.

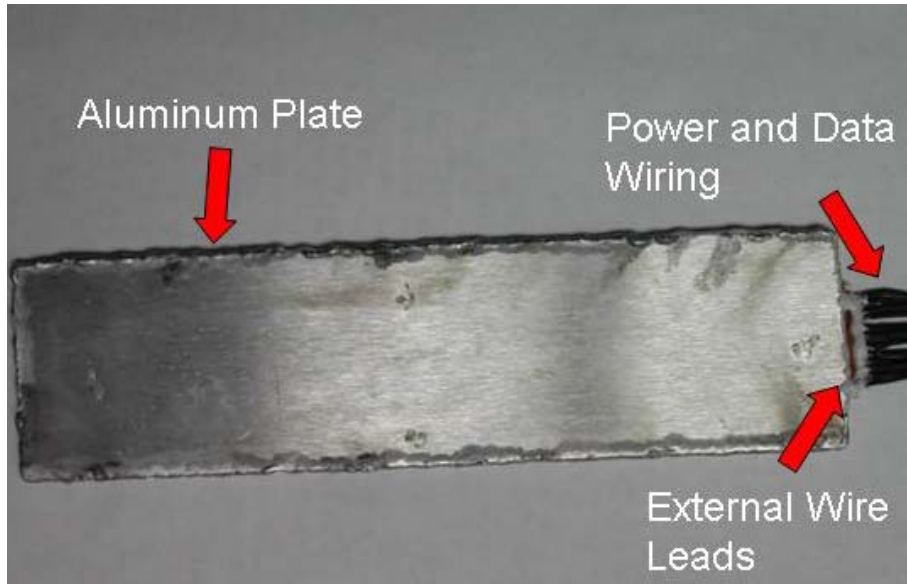


Figure 33. Fully assembled plate

The plate was tested in a custom designed and built flow loop. A modular design was created in which any part of the flow loop could easily be interchanged with new parts. The loop was also designed to supply enough cooling water to the target to remove at least 5kW. The design also collected accurate data and supplied power to the target in the test section without adversely affecting the cooling water flow. A schematic of the flow loop along with images of the finished loop and plate target test section can be seen in figures 34, 35 and 36 respectively. The dimensions of the test section used to hold the plate can be seen in figure 37.

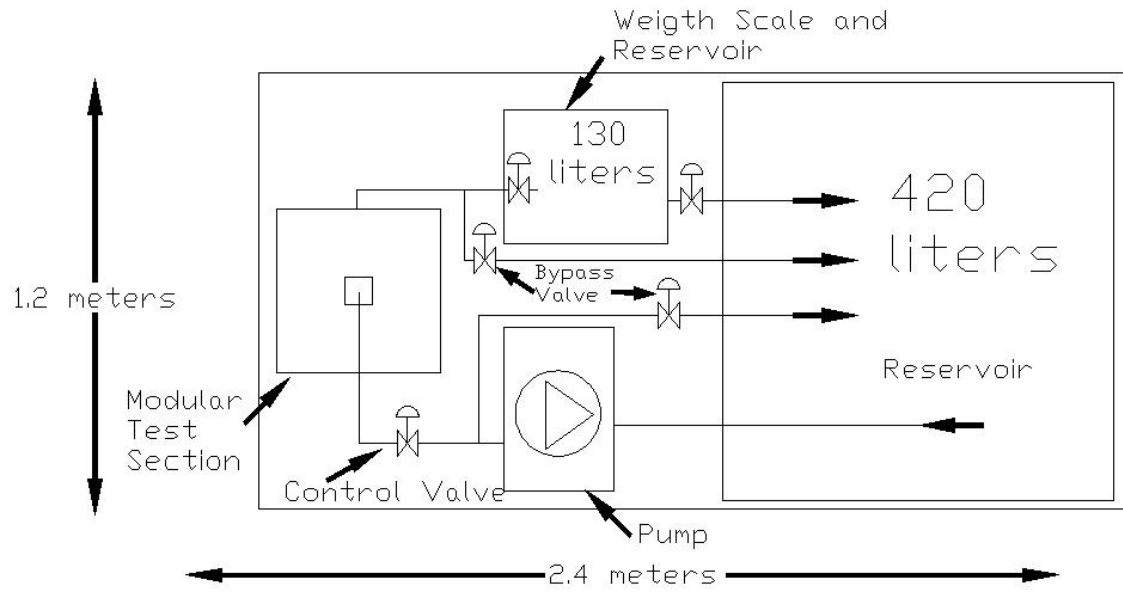


Figure 34. Schematic of the flow loop

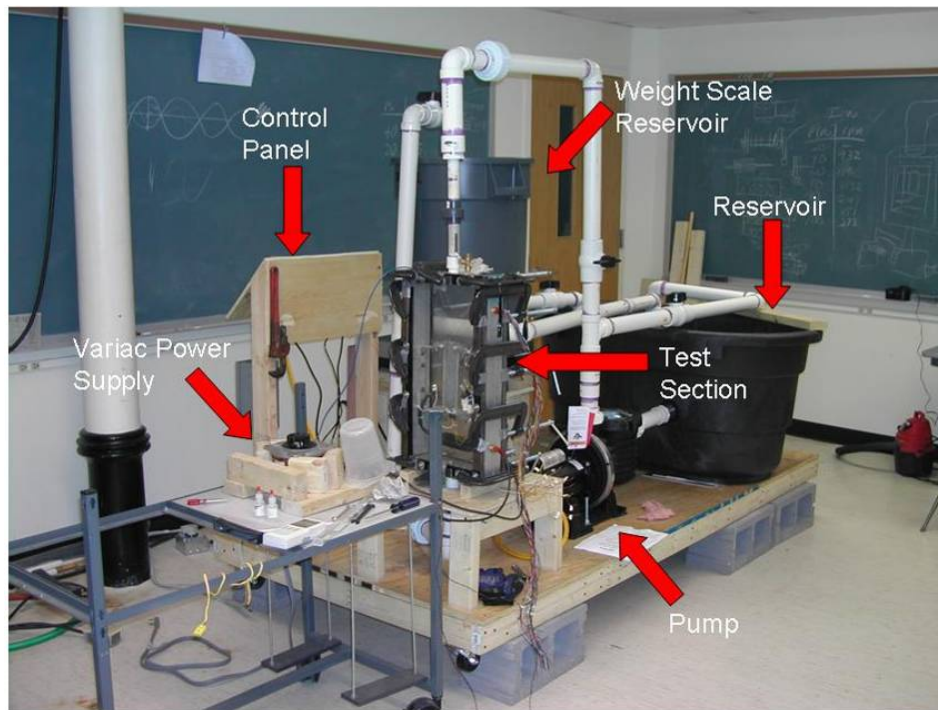


Figure 35. Image of the completed flow loop

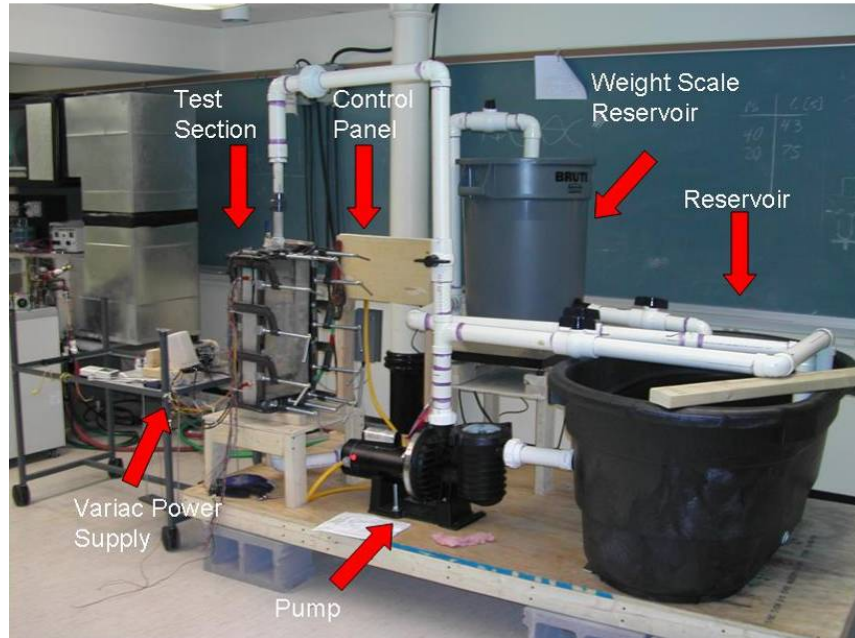


Figure 36. Image of the completed flow loop

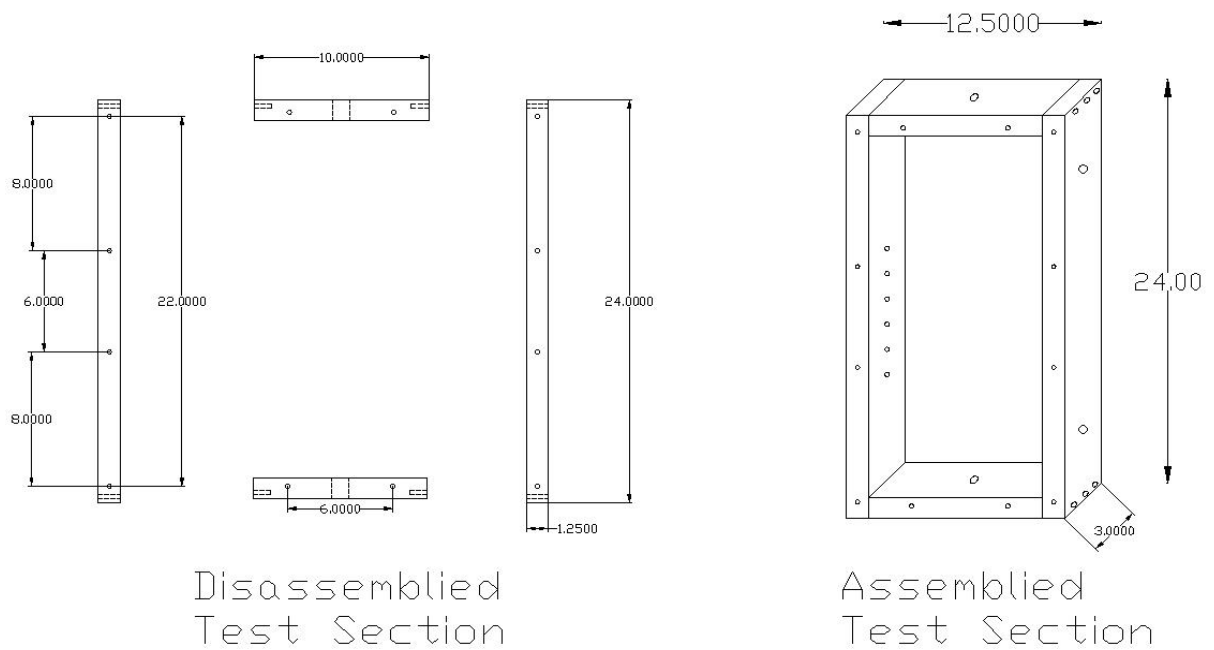


Figure 37. Test section dimensions in inches

The plate target test section was connected to the loop using PVC piping unions. The unions are not permanent connections and can be disconnected from the loop allowing the test section to be easily removed. The pump selected to provide the flow

through the loop was the Sta-Rite Max-E-Pro which was attached to a one and half horsepower motor capable of 3450 RPM using a single phase 240 V source. The path of the water through the flow loop begins in the reservoir and continues to the pump. Once it leaves the pump it can either travel back to the reservoir through the bypass valve used to control the amount of water passing through the test section or to the test section. Upon exiting the test section the water passes to either the reservoir or to the mass flow measurement tank. The mass flow measurement section used a weight scale and a 130 liter reservoir to find a mass flow rate. The weight scale used was a Transcell Technology scale that can measure up to 500 kg. The mass flow rate found during testing was approximately 2.6 kg/s.

The system was designed to collect data from the target while not restricting the deformation of the plates and without restricting the water flow around the target. Extender arms were fabricated to hold the test plate in the flow. These can be seen in figures 38 and 39 with the arms attach to the side walls of the test section.

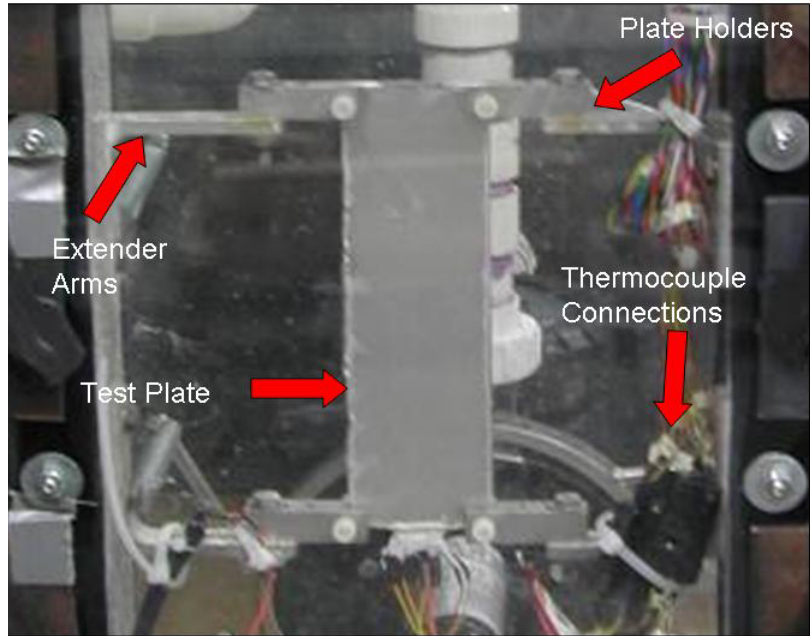


Figure 38. Extender arms in the test section with plate



Figure 39. Close up view of the extender arms

Attached to the extender arms were the plate holders. The holders were designed to prevent the plate from “chattering” plate in the flow while still allowing the plate target to grow freely. Nylon screws were used to hold the plate in place and were only lightly tightened as not to restrict any thermal deformation. Examples of the lower and upper holders can be seen in figures 40 and 41.

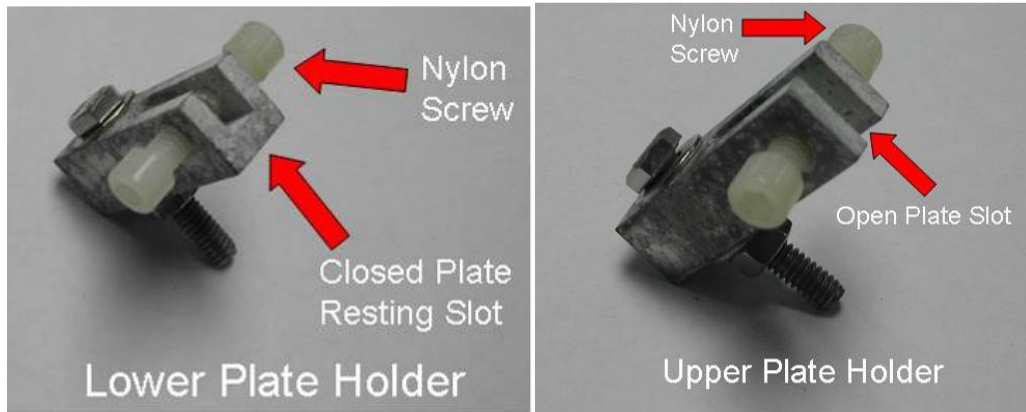


Figure 40. Lower and upper plate holders

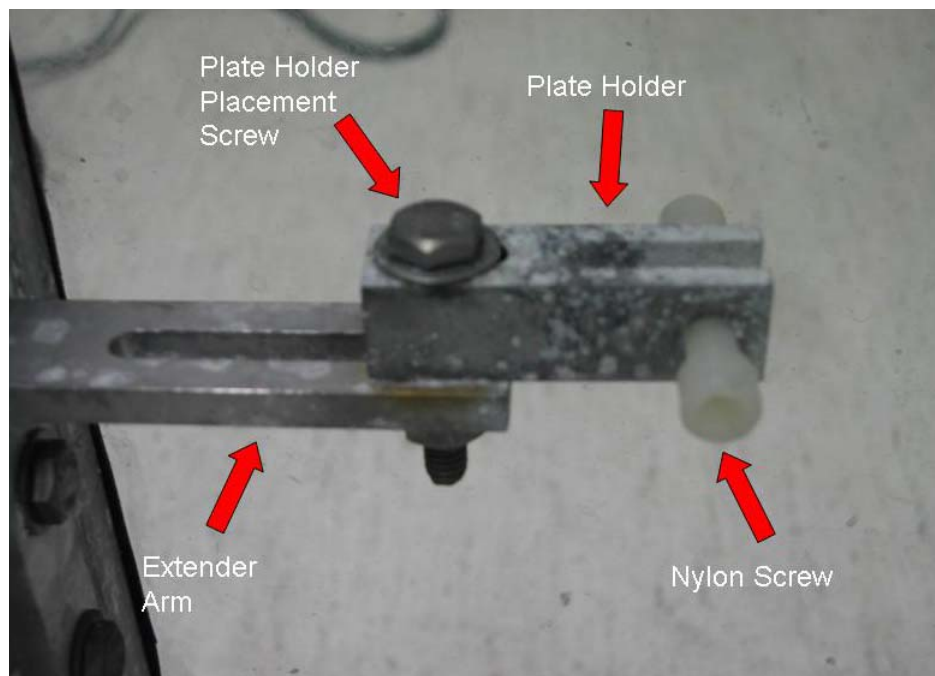


Figure 41. Slot adjustment system

The collection of the voltage measurements from the plate and the delivery of the voltage to the heater was one of the last challenges. Voltages from the thermocouples were passed from the plate to type K quick connectors located inside the test section. The connectors made the switching of plates efficient and easy. Liquid electrical tape was used to create a water tight seal around the connector which can be seen in figure 42.



Figure 42. Internal data wire connections and power supply connection

The voltage measurements and power delivery wires exit the test section through the test section pass-throughs. The signal wiring and the power supply wiring were separated to prevent any electromagnetic interference between the high current power supply wires and the signal wires. An image of the test section pass-throughs can be seen in figure 43.

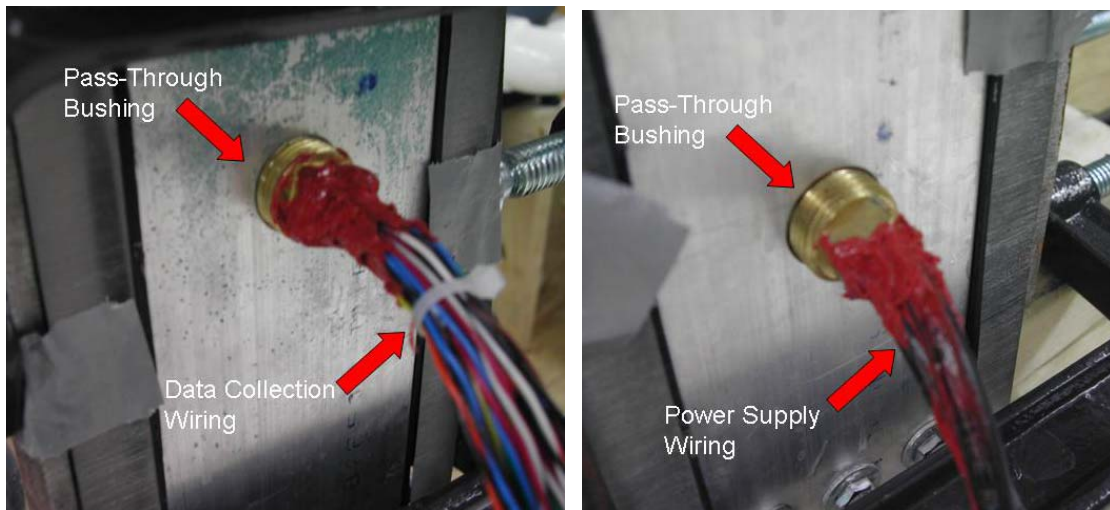


Figure 43. Test section pass-throughs for the data wiring and the power supply

Voltage measurements were collected using a Kiethley 2701 multi-meter and Excelinx was used to record the data in a spread sheet. The complete data acquisition system can be seen in figures 44 and 45.

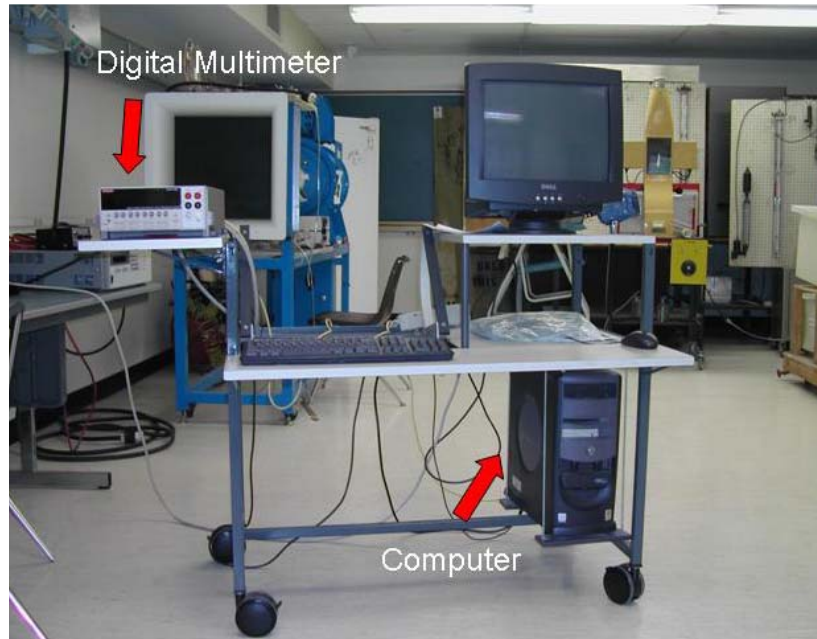


Figure 44. Complete data acquisition system

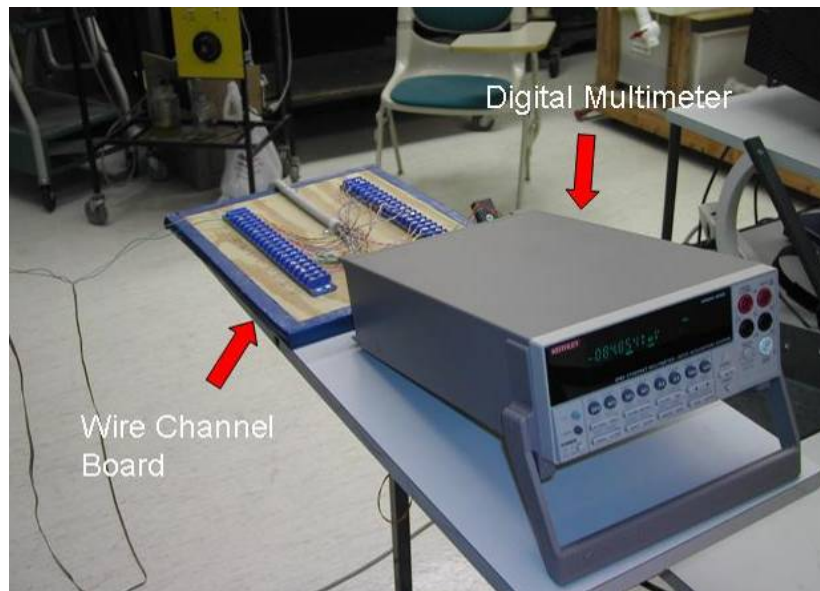


Figure 45. Digital Multimeter and Connection Board

Chapter 6: Plate Target Design Results and Discussion

Analytical Model

The goal of the analytical model is to investigate natural tendencies that develop in the target during heating. In the model a beam is subjected to a uniform heat flux on the lower surface of the beam. In this model the deflection of the beam is controlled by the difference in thermal expansion between the lower and upper surfaces. The model assumes that the ends of the beam are free to deform and the center of the beam is prevented from moving. Figure 46 shows the beam before and after the heat flux is applied and figures 47 and 48 show the deflection results.

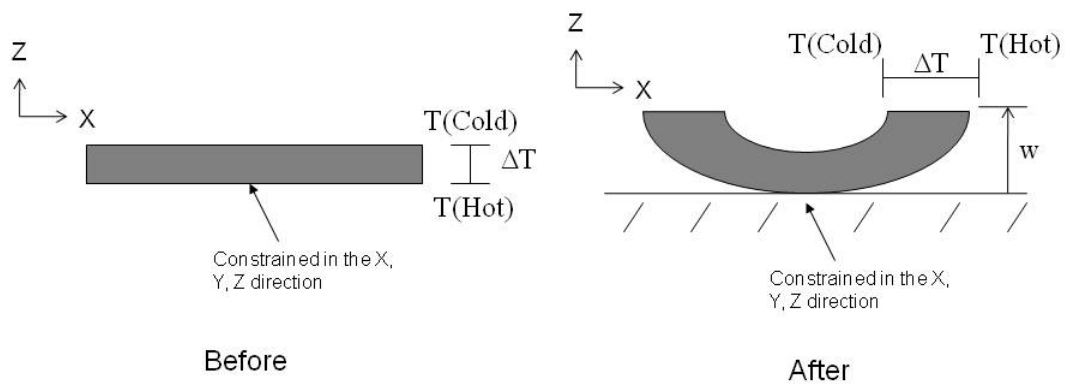


Figure 46. Analytical beam illustration

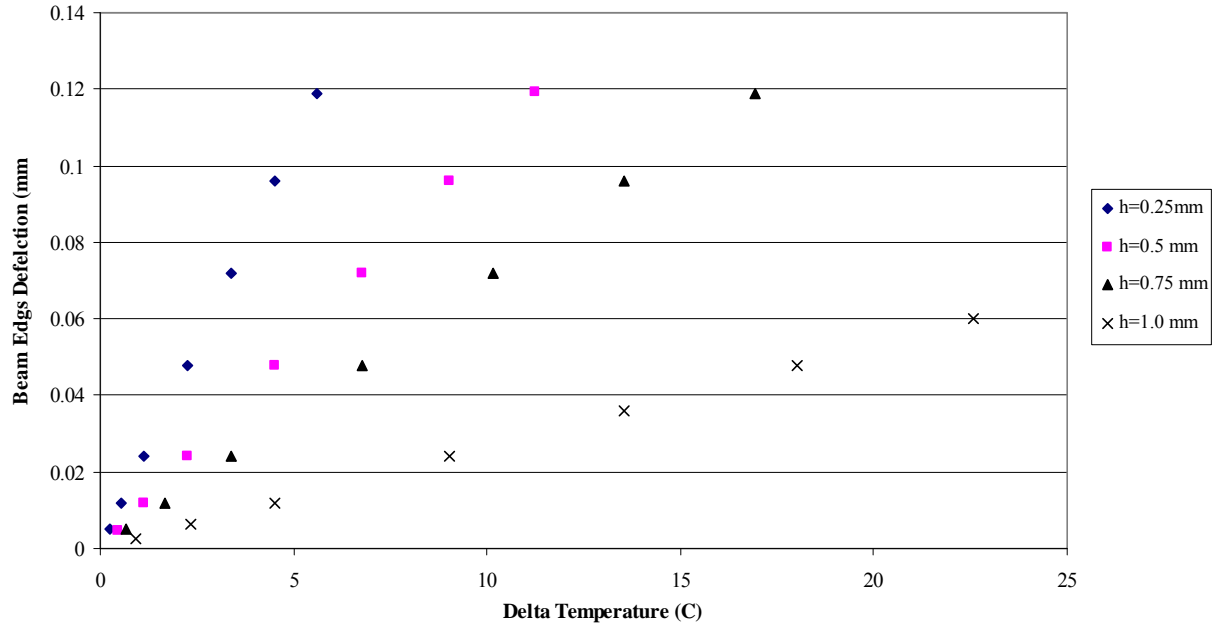


Figure 47. Plate model analytical results with a beam length of 30mm and varying beam thickness

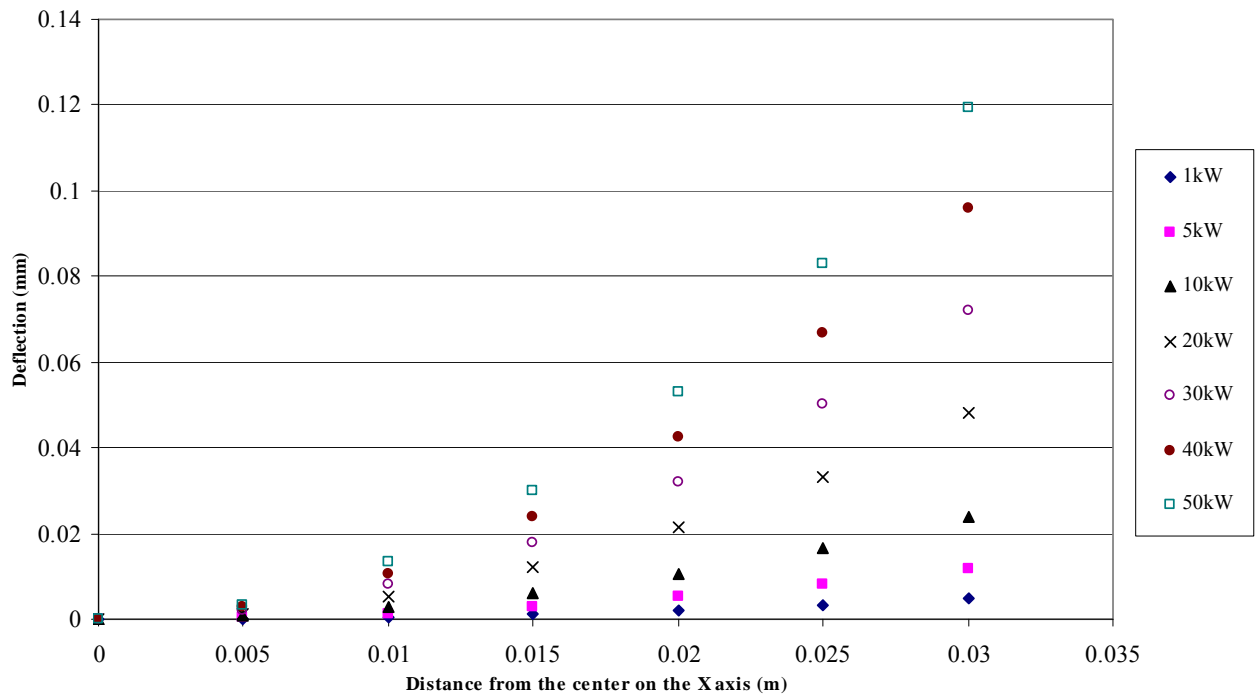


Figure 48. 1.0 mm thick beam deflection as a function of the length along the X axis with varying thermal load from 1kW to 50kW

Figure 47 shows the deflection increases in the beam as the temperature gradient

increases but decreases as the thickness increases. Figure 48 shows that the beam ends

have a greater deflection as the end of the beam is approached. This implies that the natural deformation state of the plate is not to pillow as suggested in figure 3. It is later shown that pillowing will occur when the edges of the plate are welded and constrained.

Numerical Model

The numerical model of the plate target was done to investigate plate target deformation for internal heating to reinforce the analytic trends and develop a performance map. Previous work indicated that 35 μ m of deflection would produce an unacceptable high thermal contact resistance (Solbrekken, El-Gizawy, and Allen). A parametric study was conducted using Algor. The parametric study includes the external heat transfer coefficient, the internal heat flux, the thickness of the individual aluminum plates, the internal fission gas pressure and the plate target edge constraint conditions. Aluminum 6061 with temperature independent mechanical properties was used during the investigation.

The external heat transfer coefficient was examined with varying internal heat flux and plate thicknesses. The two heat transfer coefficients used during the study were 20,000 W/mK and 10,000W/mK. The values were selected because they are representative of the range of values provide by the reactor coolant. Simulations were conducted at these two heat transfer coefficients while varying the internal heat flux at 1, 5, 10, 20, 30, 40, and 50 kW. The plate thickness was varied at 0.5, 1.0, 1.5, and 2.0 mm. The model edge boundary conditions i.e. its ability to move in the X, Y, and Z direction can be seen in figure 49 and table 8. It should be noted that the edges constrained only in Z direction simulate a weld between the two edges. The deflection of the plate center for

different plate thicknesses (L), heat fluxes, and heat transfer coefficients from the numerical simulations can be seen in figures 50 through 55.

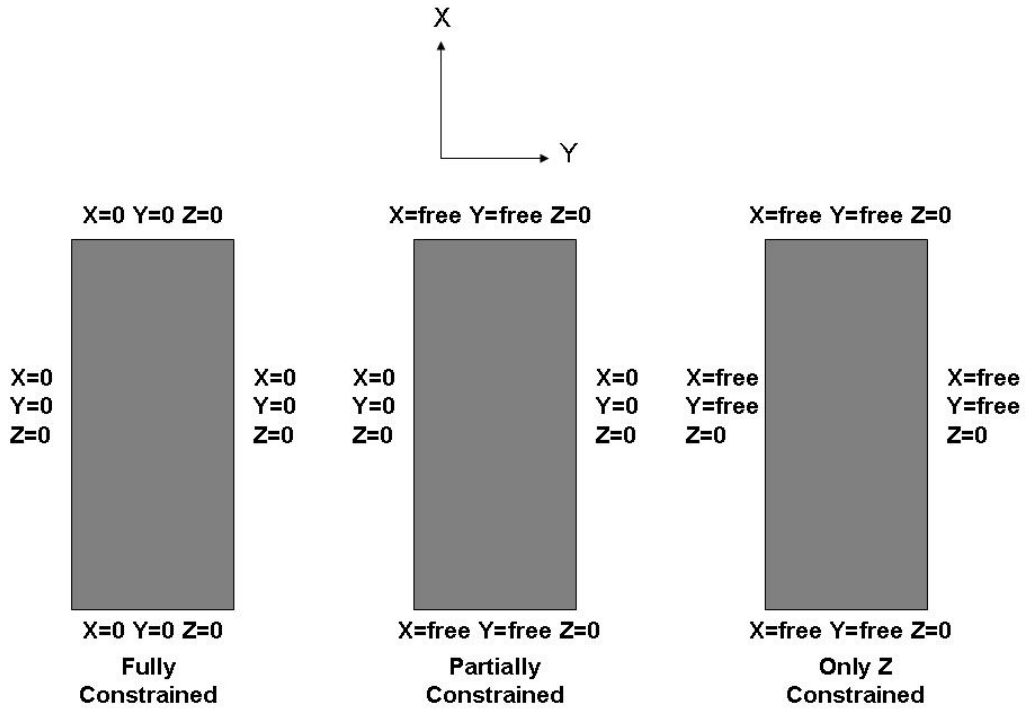


Figure 49. Numerical model plate edge boundary conditions

Table 8. Summary of numerical plate boundary conditions

| | <i>Left Edge</i> | <i>Right Edge</i> | <i>Upper Edge</i> | <i>Lower Edge</i> |
|------------------------------|-----------------------|-----------------------|-----------------------|-----------------------|
| Fully Constrained | $X=0, Y=0, Z=0$ | $X=0, Y=0, Z=0$ | $X=0, Y=0, Z=0$ | $X=0, Y=0, Z=0$ |
| Partially Constrained | $X=0, Y=0, Z=0$ | $X=0, Y=0, Z=0$ | $X=free, Y=free, Z=0$ | $X=free, Y=free, Z=0$ |
| Only Z Constrained | $X=free, Y=free, Z=0$ | $X=free, Y=free, Z=0$ | $X=free, Y=free, Z=0$ | $X=free, Y=free, Z=0$ |

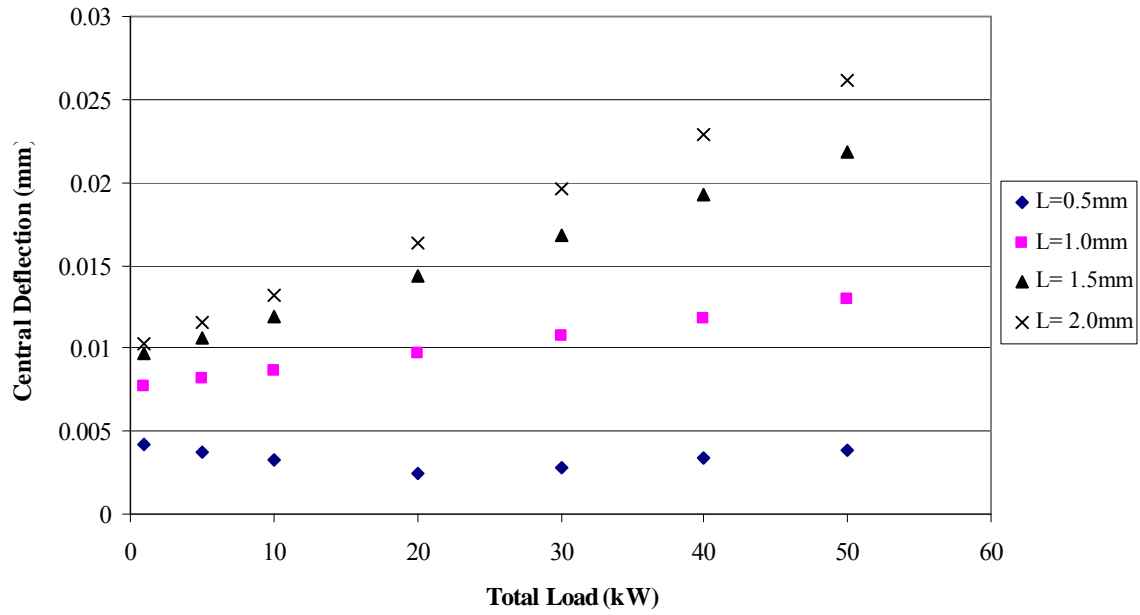


Figure 50. Fully constrained at $h = 20,000 \text{ W/mK}$

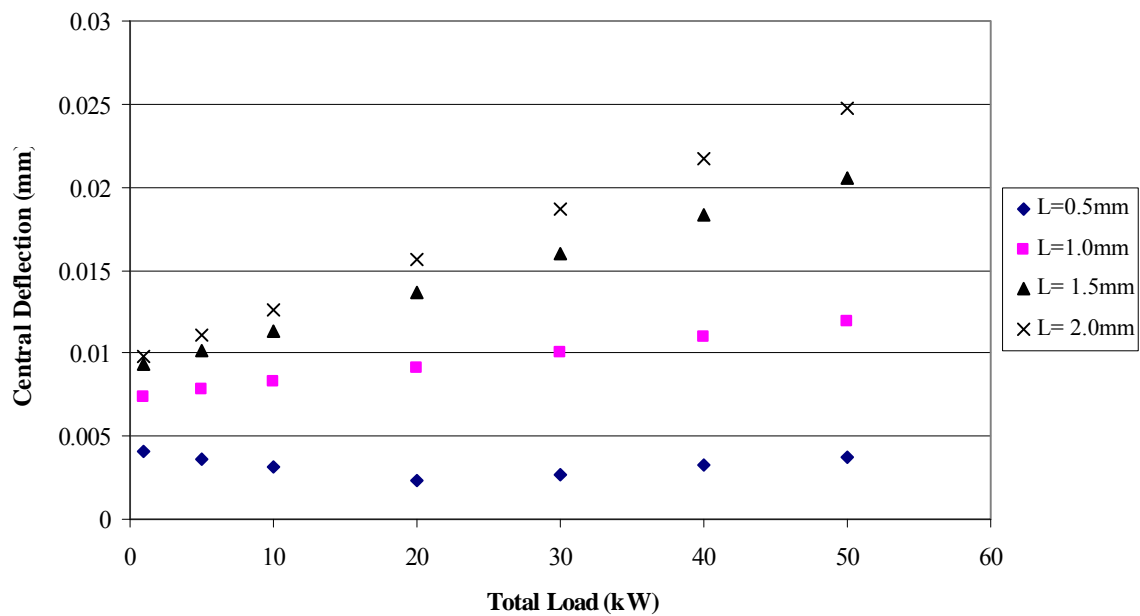


Figure 51. Partially constrained at $h = 20,000 \text{ W/mK}$

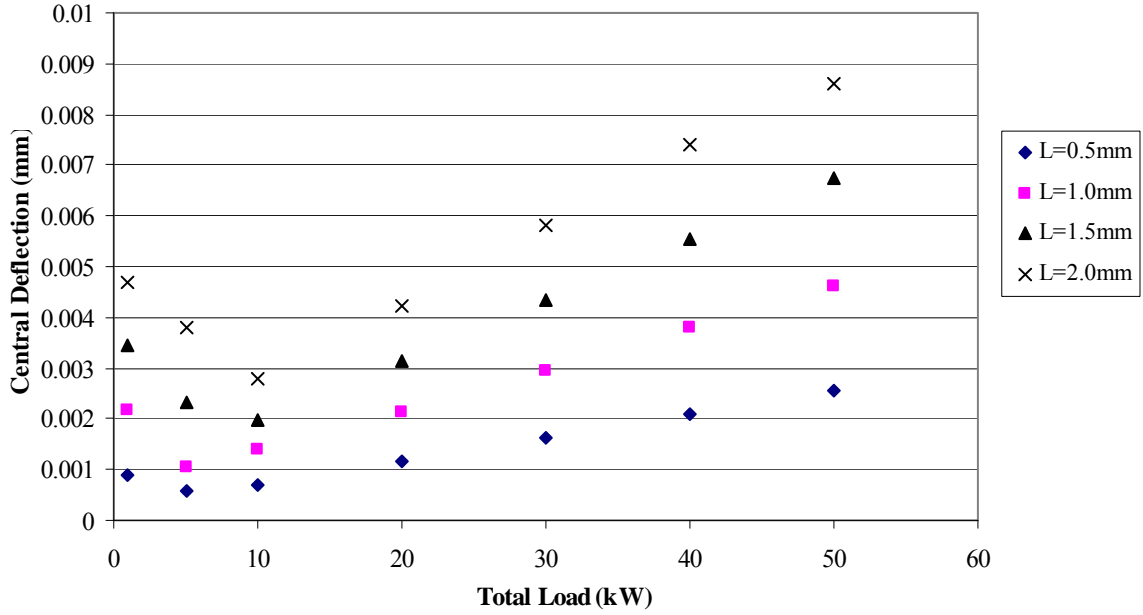


Figure 52. Only Z constrained at $h = 20,000 \text{ W/mK}$

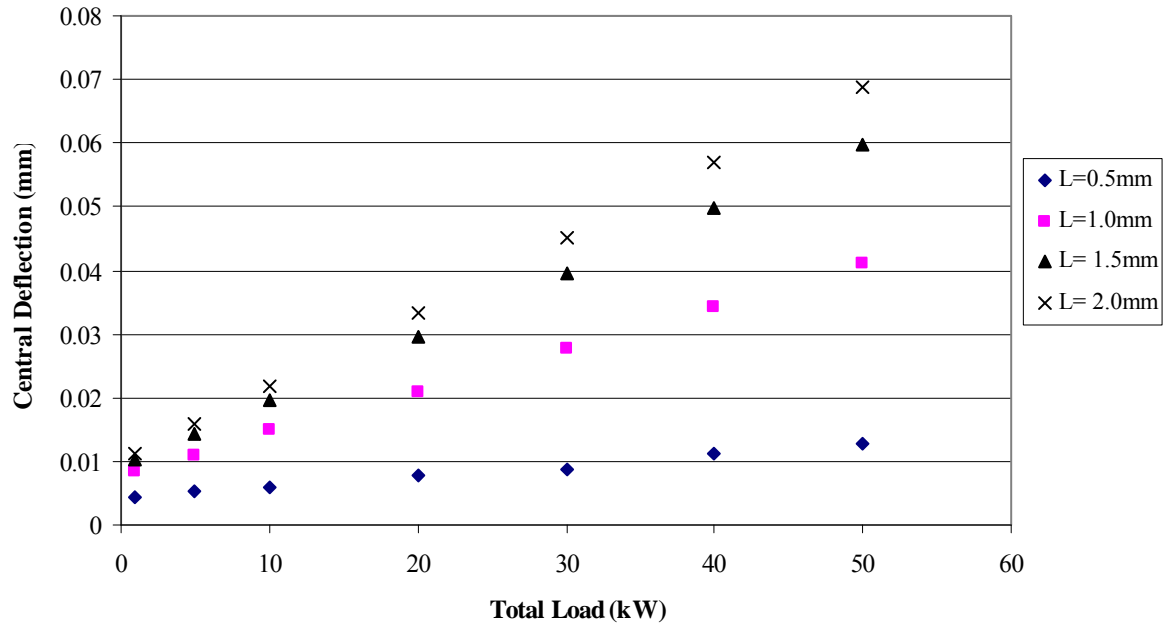


Figure 53. Fully constrained at $h = 10,000 \text{ W/mK}$

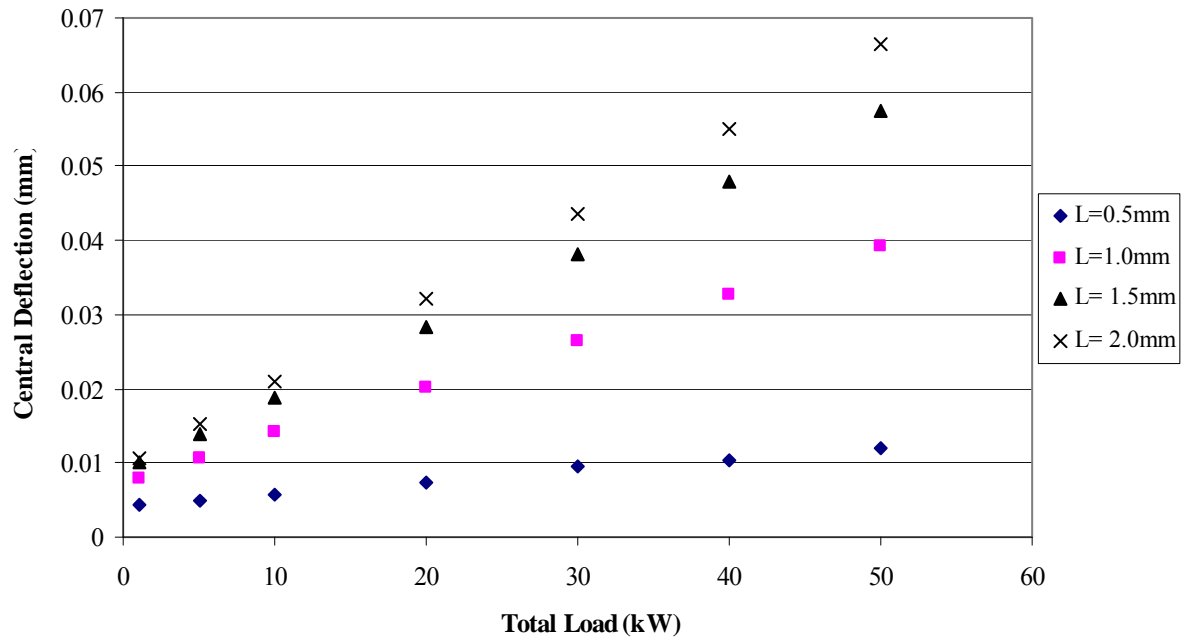


Figure 54. Partially constrained h = 10,000 W/mK

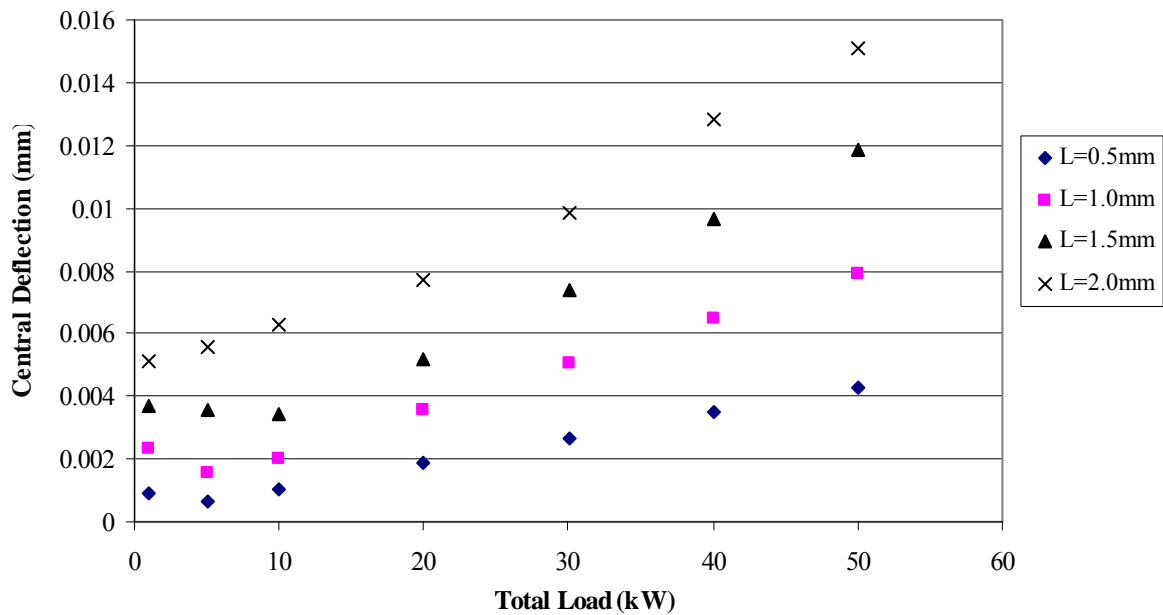


Figure 55. Only Z axis constrained h = 10,000 W/mK

In figures 50, 51, 53, and 54 the deflection at the center of the target increases as the thermal load increases and as the thickness of the plate increases. This direct correlation is seen in the studies that have at least two edges constrained. The Figures 52 and 55 show that when the edges are free to move in the XY plane the deflection first decreases

and then increases as the thermal load increases. The non-uniform heating of the internal surfaces of the plate creates a two dimensional temperature gradient through the target. Figure 56 shows the central deflection but instead of applying the heat flux on only a fraction of the internal plate the heat flux is applied to entire internal surface. The uniform heat flux eliminates the two dimensional temperature gradients through the target and creates a one dimensional temperature difference.

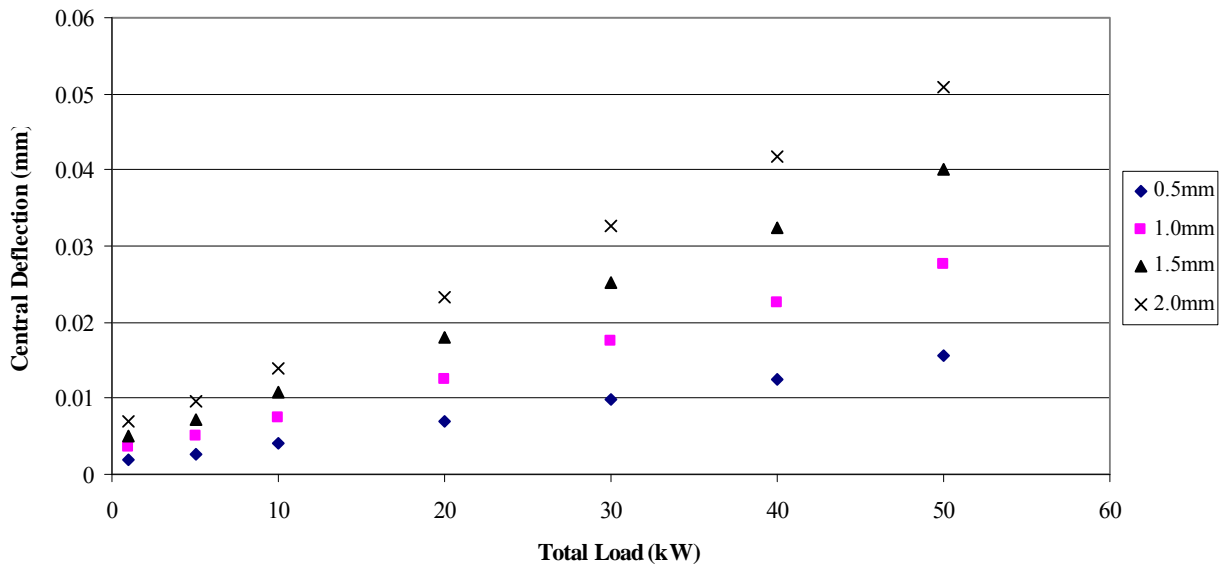


Figure 56. Only Z axis constrained $h=20,000\text{W/mK}$ with a uniform heat flux

Figure 56 shows the uniform heating data indicating that the trends in the deflections are linear with a one dimensional temperature distribution. The linear trends confirm that the dip seen in figures 52 and 55 was caused by the two dimensional temperature distributions.

The greatest amount of central deflection which is below the $35\ \mu\text{m}$ limit was seen in figure 53 with the fully constrained boundary condition. In the fully constrained condition the target can only deflect in the Z direction which means that the thermal expansion only contributes to Z axis deflection. In the other constraint conditions some

amount of X and Y deflection is allowed thus the deflection caused by the thermal expansion causes deflection in multiple directions.

The effects of a simulated fission gas pressure inside the target were unknown. During irradiation the uranium will produce gases such as radioactive radon and various radioactive noble gases. These gases will increase the force pressing on the internal walls of the plates. Gas pressures of 5 psi and 10 psi were used produce a wide performance map of the target's behavior. The pressures were applied to the internal walls of the plate and directed outward along the Z axis. The gas pressures were only applied to the 10,000 W/mK condition as it produced the greatest amount of deflection in the previous study.

The combined effects of the internal heat flux and the gas pressure for the fully constrained condition can be seen in figures 57 through 64.

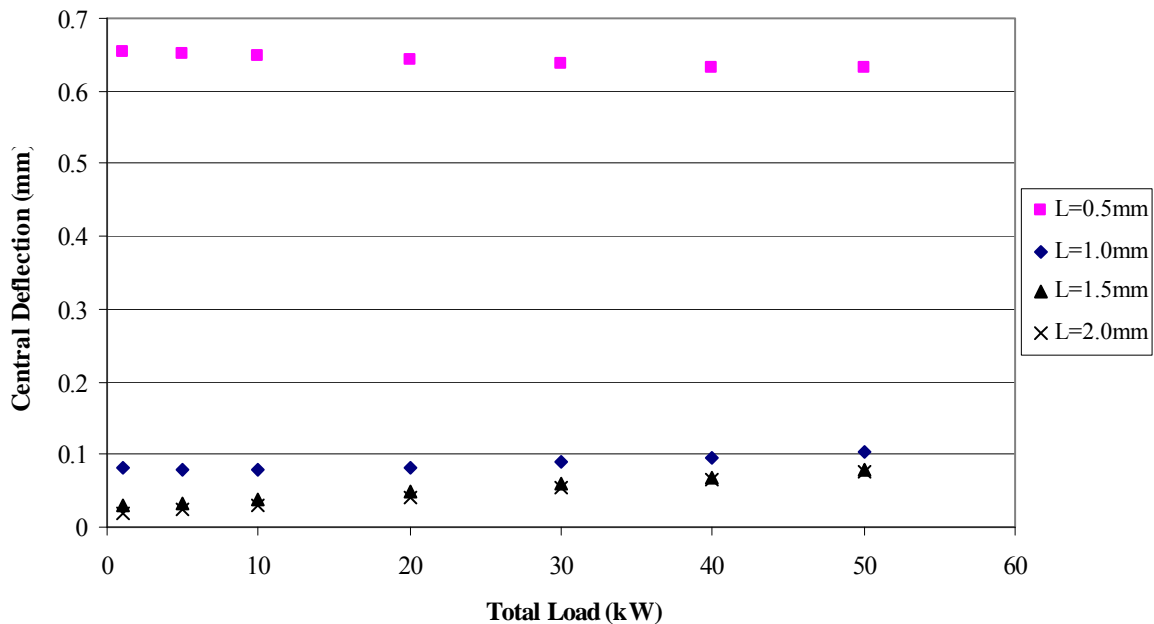


Figure 57. Fully Constrained at a 5psi gas pressure

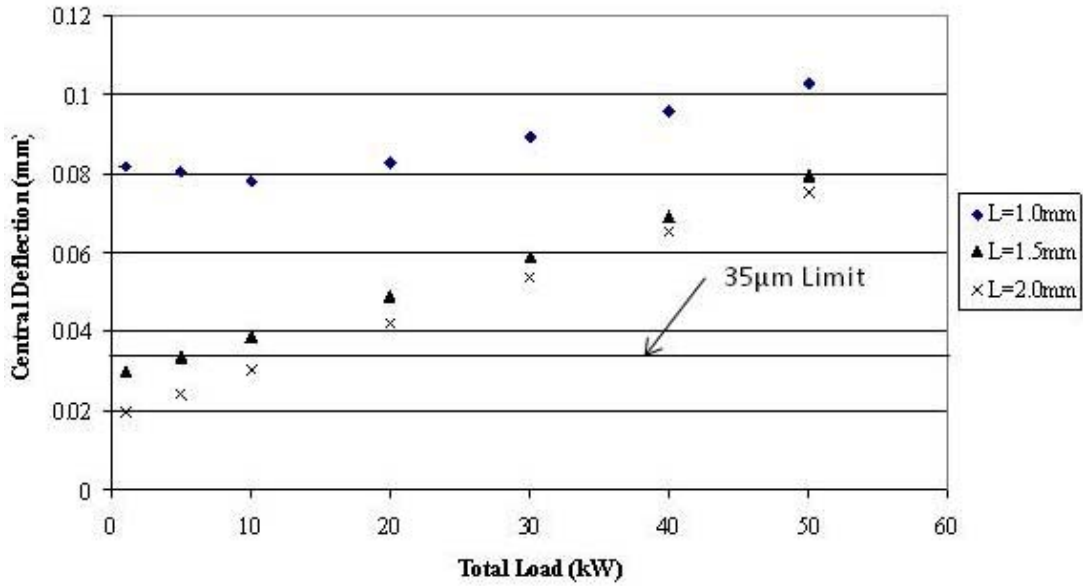


Figure 58. Fully Constrained at 5psi and with no 0.5mm plate thickness data

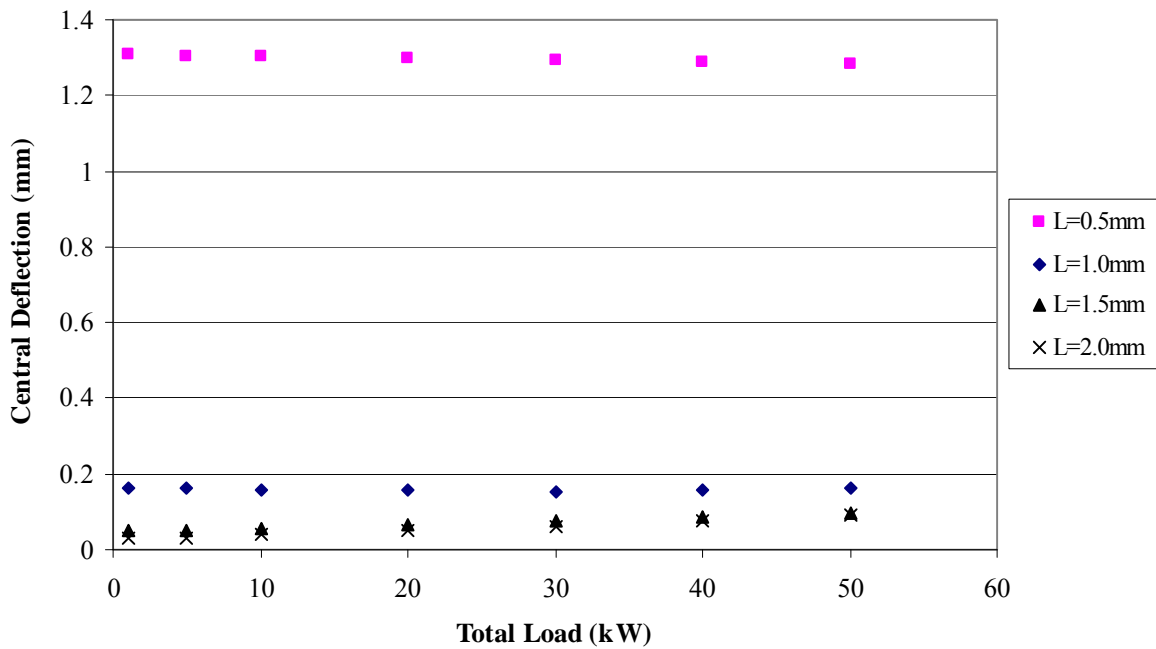


Figure 59. Fully Constrained at a 10psi gas pressure

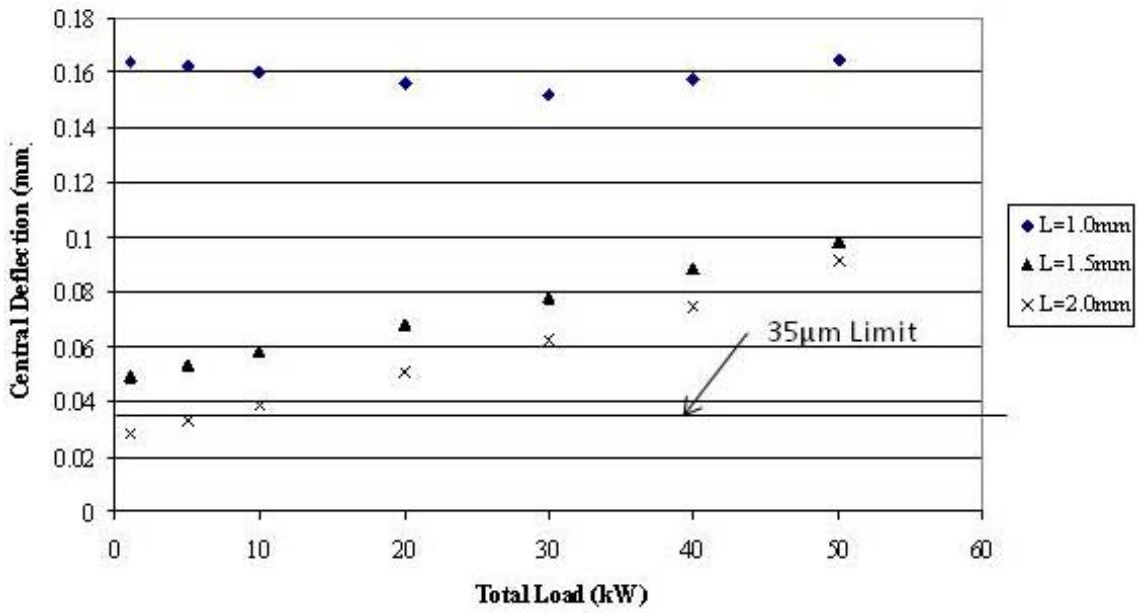


Figure 60. Fully Constrained at 10psi with no 0.5mm plate thickness data

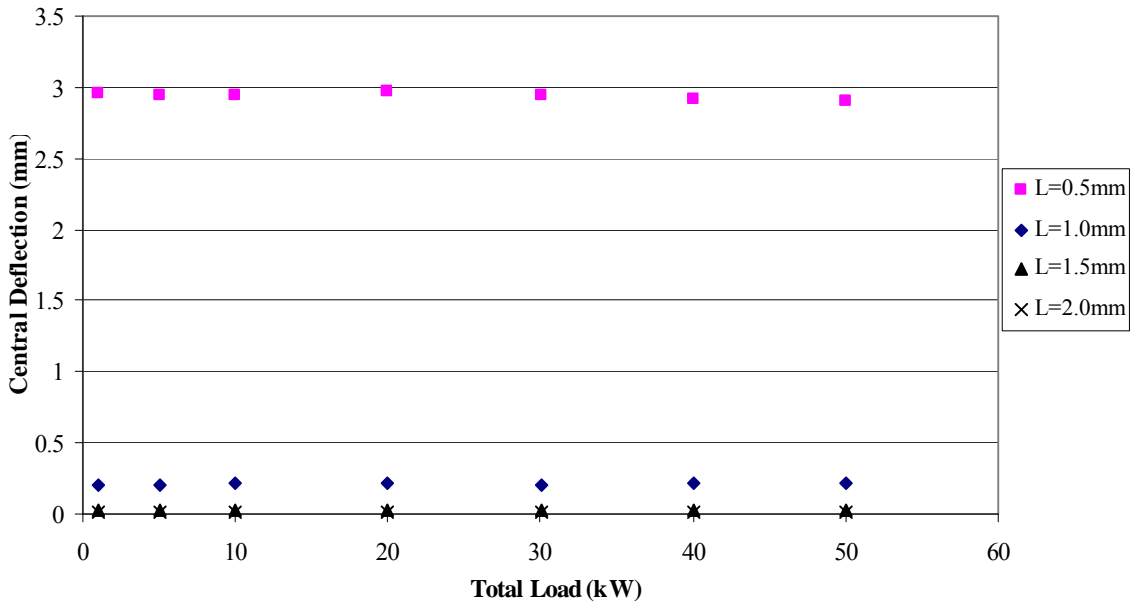


Figure 61. Only Z axis constrained at a 5psi gas pressure

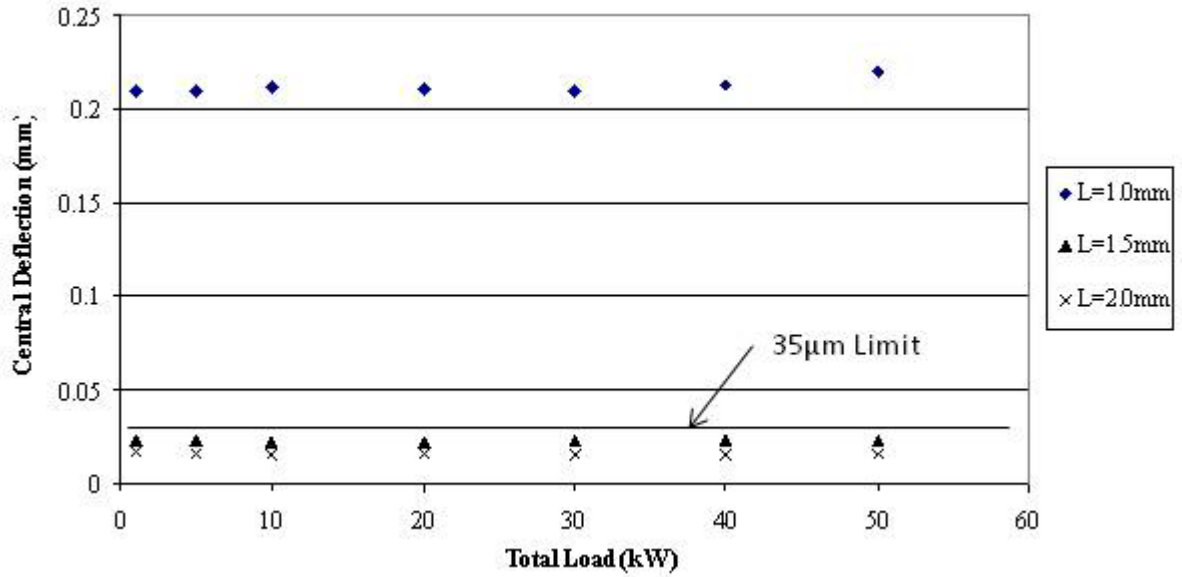


Figure 62. Only Z axis constrained at 5psi with no 0.5mm plate thickness data

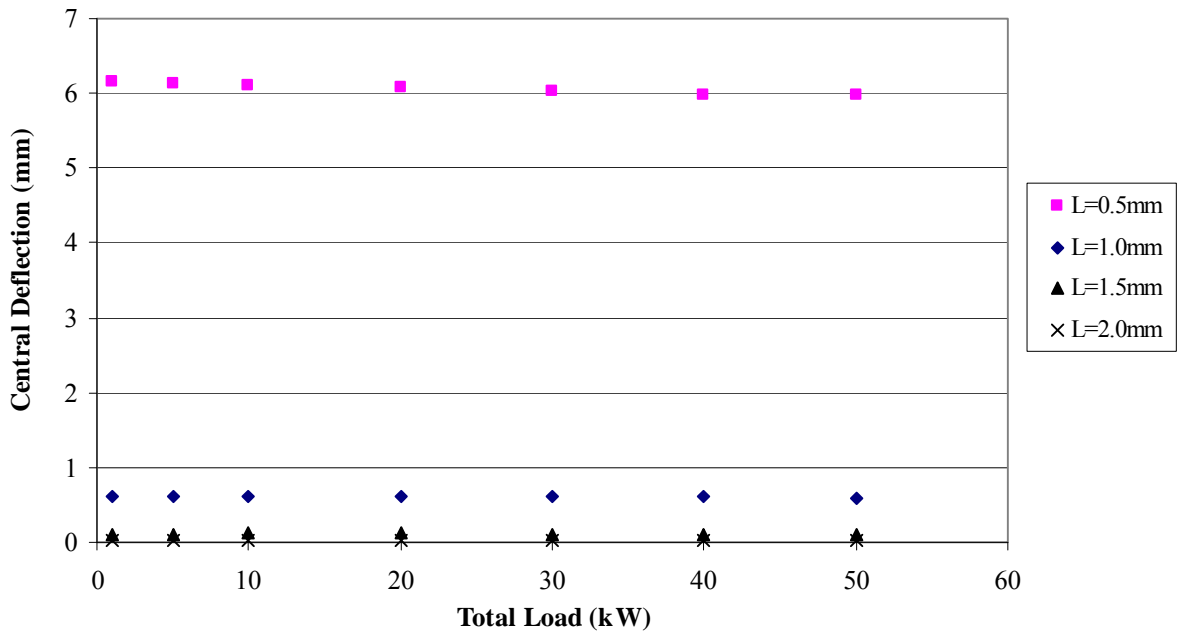


Figure 63. Only Z axis constrained at a 10psi gas pressure

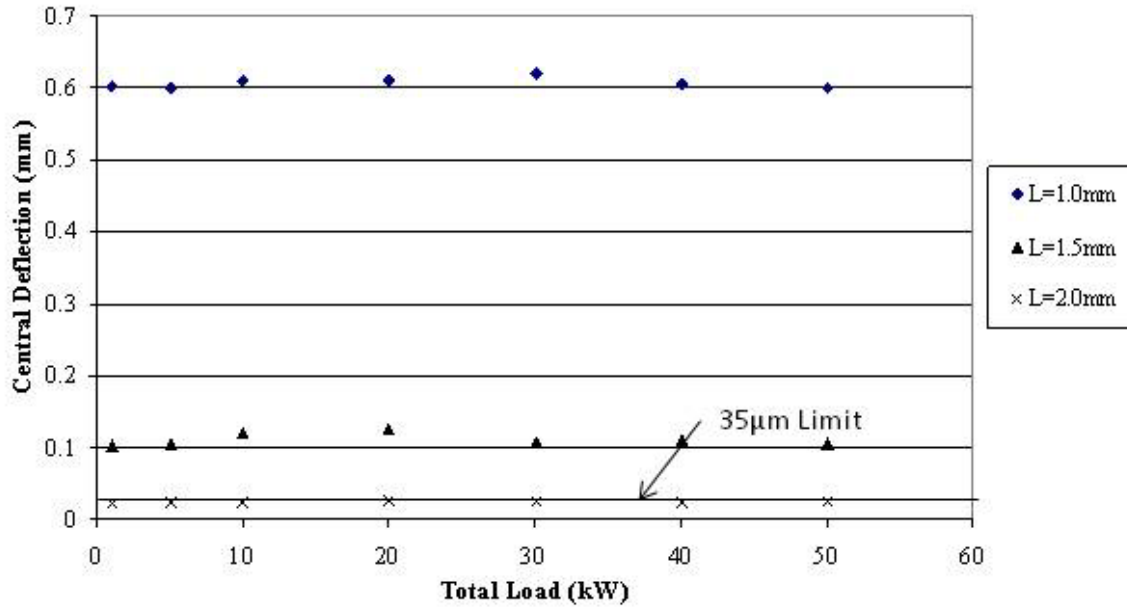


Figure 64. Only Z axis constrained at 10psi with no 0.5mm plate thickness data

In figures 57 and 59 the data for 0.5mm plate thickness is much greater than the other results and has a horizontal trend. The gas pressure overrides any effect the temperature distribution has on the deflection. An increase in the heat flux has little effect on the deflection thus creating the horizontal trend. Figures 58 and 60 are the results without the 0.5mm plate thickness data and amplify the data from the other thicknesses. The data indicates that the thermal distribution begins to affect the central deflection around a thickness 1.0mm. Figures 58 and 60 also show that heat flux has lower affect on the central deflection when the gas pressure is 10psi as compared to the 5psi results. The partially constrained boundary conditions displayed many of the same trends as the fully constrained and can be found in appendix 3. The results also show what conditions will surpass the 35µm limit as can be seen in figures 58, 60, 62, and 64. The contributions of the combined thermal and gas pressure effects can be seen in figure 65.

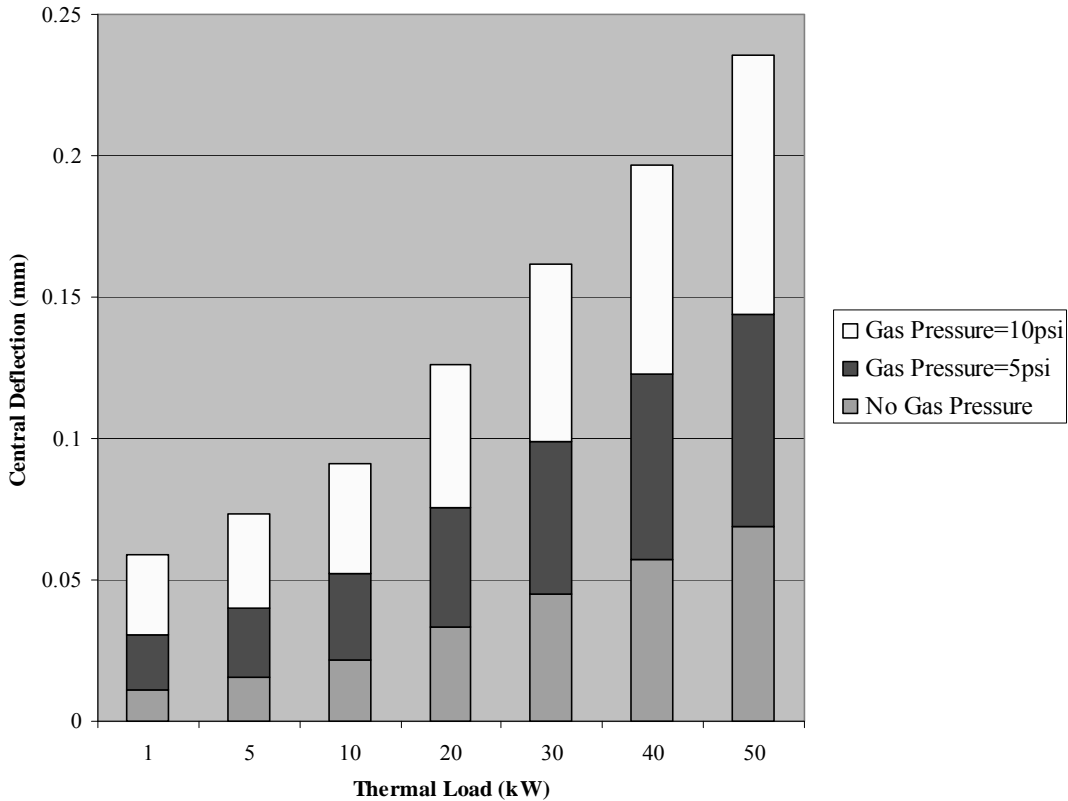


Figure 65. Combine thermal and gas pressure effects for 2.0mm thickness at $h=10,00W/mK$

Figure 65 indicates that the contributions of the temperature and gas pressures are linear.

Figures 57 through 64 indicate that fission gas pressure has a greater effect on the central deflection in the only Z axis constrained conditions. In the fully constrained condition the edges of the plate are not allowed to move in any X, Y, or Z direction. The force created by the gas pressure pushes on the interior walls of the target which in turn creates deflection in the Z direction. At same time the edges of the plates are attempting to move inward along the XY plane to compensate for the Z axis deflection. The fully constrained condition prevents the edges from moving in the XY plane thus limiting the amount the amount of central deflection. In the Z axis only constrained condition the edges of the plate are free to move in the XY plane. The deflection created by the gas

pressure pulls the edges of the plate toward the center thus allowing more central deflection to occur.

The deflection data in the previous plots gives the deflection of the target at its center. Figures 66, 67, and 68 show contour plots of the deflection in the Z direction where the darks areas are the greatest deflections.

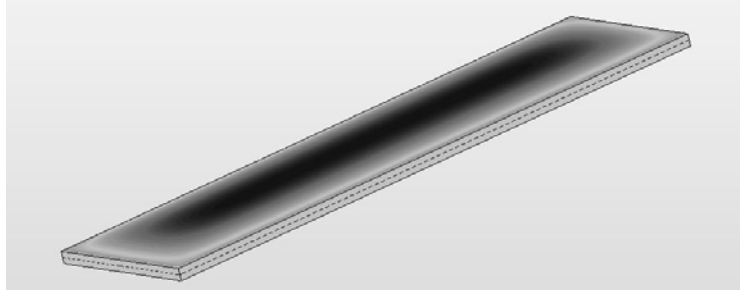


Figure 66. Fully constrained deflection in the Z direction contour plot

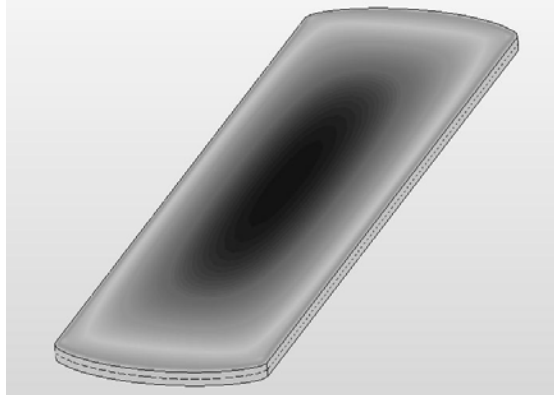


Figure 67. Partially constrained deflection in the Z direction contour plot

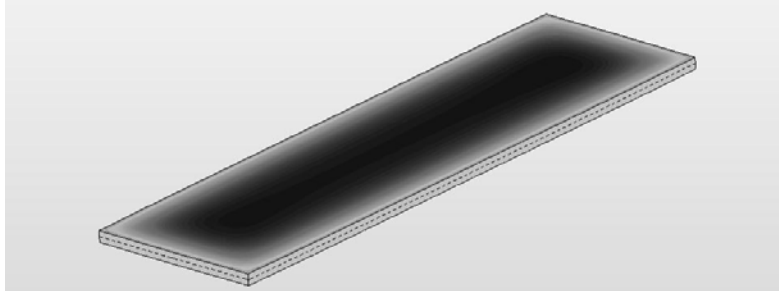


Figure 68. Z only constrained deflection in the Z direction contour plot

The figure show that the maximum deflection in the dark areas

The stress distributions from the three studies were dramatically different for each constraining condition. Figures 69 through 71 show the stress distributions for the three

different constraint conditions. The distributions are all created using the 0.5 mm plate thickness, $h=10,000$ W/mK and 50kW internal heat flux study. The dark areas correspond to the highest stress values and the light areas correspond to the lowest stress values.

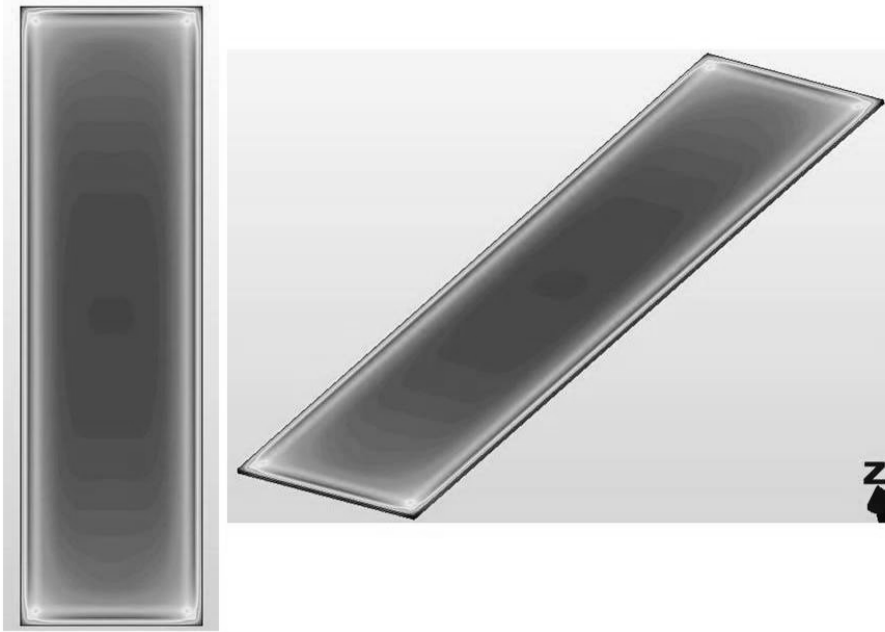


Figure 69. Fully constrained Von Mises stress gradient



Figure 70. Partially constrained Von Mises stress gradient

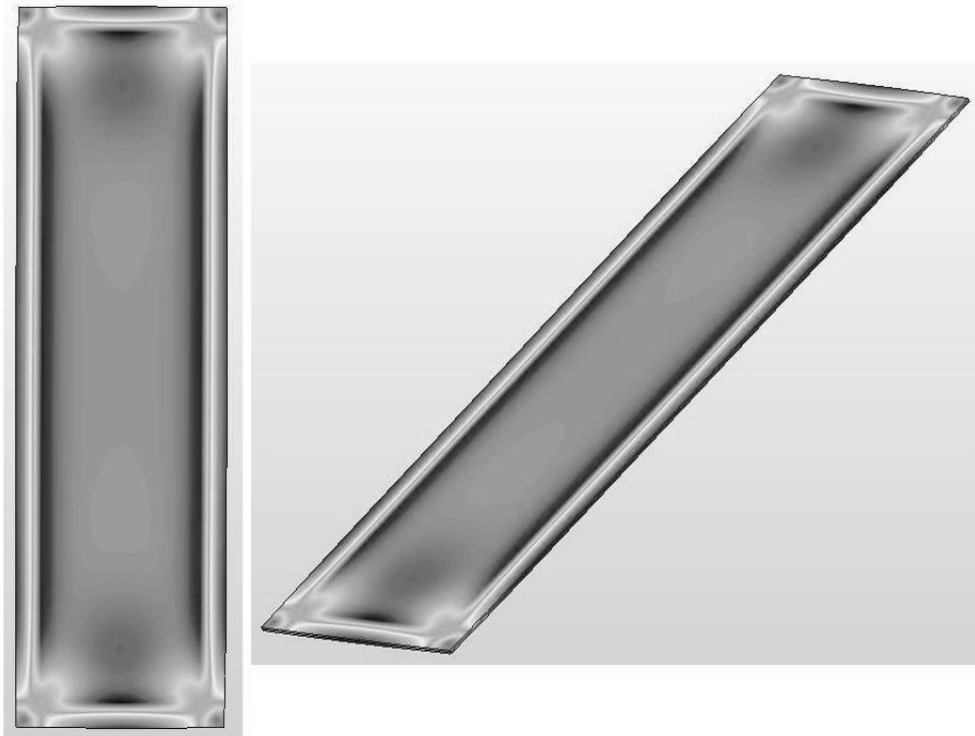


Figure 71. Only Z axis constrained Von Mises stress gradient

The fully constrained distribution indicates that the highest areas of stress are located in the central part of the target. The central area experiences the highest stresses because the fully constrained edges force all of the displacement energy into the central region.

Distributions from the partially constrained study indicate that the highest stress values are on the four corners of the plate. The corners have the highest stress values because the vertical edges of the plate are held in place thus when the top and bottom edges expand the material on the corners are stretched and pulled by the force. The only Z axis constrained distribution indicates that the highest stress values occur on the edges of the target where the two plates would be welded. Free expansion along the target edges creates a great amount of force which in turn creates a large amount of stress. The stress distributions for different internal heat fluxes and different internal gas pressures were similar to the figures above the only difference was their magnitude.

Von Mises stress was the stress type used to measure the magnitude of the stresses. Stress values in the center and edges of the target were examined for varying gas pressures, plate thickness, constraining conditions and heat fluxes. The heat fluxes applied to the target during the investigation were 50kW and 20kW. Tables 9, 10 , 11, and 12 show the maximum stresses at the center and edges of the target.

Table 9. Von Mises stress results when only constrained along the Z axis at 50kW

| | <i>P=0psi</i> | <i>P=5psi</i> | <i>P=10psi</i> |
|------------------------|---------------|---------------|----------------|
| Center Stress, L=2.0mm | 14.4 MPa | 53.3 MPa | 55 MPa |
| Edge Stress, L=2.0mm | 306 MPa | 250 MPa | 244 MPa |
| Center Stress, L=0.5mm | 7.4 MPa | 52 MPa | 55.3 MPa |
| Edge Stress, L=0.5mm | 305 MPa | 228 MPa | 229 MPa |

Table 10. Von Mises stress results when fully constrained at 50kW

| | <i>P=0psi</i> | <i>P=5psi</i> | <i>P=10psi</i> |
|------------------------|---------------|---------------|----------------|
| Center Stress, L=2.0mm | 651 MPa | 649 MPa | 648 MPa |
| Edge Stress, L=2.0mm | 110 MPa | 167 MPa | 181 MPa |
| Center Stress, L=0.5mm | 660 MPa | 660 MPa | 660 MPa |
| Edge Stress, L=0.5mm | 130 MPa | 131 MPa | 150 MPa |

Table 11. Von Mises stress results when only constrained along the Z axis at 20kW

| | <i>P=0psi</i> | <i>P=5psi</i> | <i>P=10psi</i> |
|------------------------|---------------|---------------|----------------|
| Center Stress, L=2.0mm | 27 MPa | 27 MPa | 30 MPa |
| Edge Stress, L=2.0mm | 129 MPa | 129 MPa | 131MPa |
| Center Stress, L=0.5mm | 29 MPa | 29 MPa | 29 MPa |
| Edge Stress, L=0.5mm | 130 MPa | 131 MPa | 130 MPa |

Table 12. Von Mises stress results when fully constrained at 20kW

| | <i>P=0psi</i> | <i>P=5psi</i> | <i>P=10psi</i> |
|------------------------|---------------|---------------|----------------|
| Center Stress, L=2.0mm | 291 MPa | 291 MPa | 290 MPa |
| Edge Stress, L=2.0mm | 92 MPa | 92 MPa | 92 MPa |
| Center Stress, L=0.5mm | 297 MPa | 298 MPa | 298 MPa |
| Edge Stress, L=0.5mm | 45 MPa | 45 MPa | 45 MPa |

The tables indicate that the stresses in the target are heavily dependent on the constraining conditions and the heat flux. The center and edges stresses for the fully constrained condition and Z axis only constrained show completely opposite trends. Tables 10 and 12 indicate that gas pressure does not affect the stress in the target when fully constrained. Tables 9 and 11 however show that gas pressure can affect the stress but only when the internal heat flux is high. A comparison of the stresses from the 50kW and 20kW tables indicate that heat flux plays a substantial role in the magnitude of the stresses that develop.

Table 13 gives the yield and tensile strengths, with a factor of safety of 1.2, of several materials that could possibly be used as cladding in the real target. It should be noted that the strength of the weld was not taken into account when examining the target in the numerical model.

Table 13. Yield and tensile strengths of possible cladding at factor of safety of 1.2
(Budynas, Mischke, Shigley, 2004)

| <i>Material</i> | <i>Yield Strength (MPa)</i> | <i>Tensile Strength (MPa)</i> |
|---------------------|-----------------------------|-------------------------------|
| Al-3300 | 40.8 | 108 |
| Al-6061 | 66 | 148.8 |
| Al-1100 | 126 | 132 |
| 302 Stainless Steel | 246 | 618 |
| 403 Stainless Steel | 330 | 582 |

Experimental Setup

The experimental setup discussed in chapter 4 collected data on the heater voltage, the 1 milliohm shunt resistor voltage, and the voltage outputs of the five internally placed thermocouples. Excelinx and DMM system were used to collect the various voltages. Currently there have been a total of six different plates created and tested in the flow loop of those six only four yield useable results. All have failed to reach the desired 5kW thermal load but there has been a substantial increase in thermal load since the beginning of testing.

Temperature data collected at the maximum power for each respective experiment can be seen in table 14 and plots of the power versus temperature during experimentation can be seen in appendix 3.

Table 14. Maximum power and maximum temperature reached before failure

| <i>Experiment Number</i> | <i>Maximum Power (W)</i> | <i>TC 1 (°C)</i> | <i>TC 2 (°C)</i> | <i>TC 3(°C)</i> | <i>TC 4(°C)</i> | <i>TC 5(°C)</i> |
|---------------------------------|---------------------------------|-------------------------|-------------------------|------------------------|------------------------|------------------------|
| 3 | 1208 | 27.4 | 30.2 | 34.7 | 34.2 | 30.9 |
| 4 | 1289 | 27.3 | 26.5 | 32.5 | 25.5 | 27.6 |
| 5 | 2318 | 35.8 | 33.4 | 44.3 | Failure | 32.7 |
| 6 | 1565 | 34.7 | 33.9 | 41.2 | 31.5 | 35.2 |

The temperature distribution in the target is what would be expected. Higher temperatures are located in the central part of the plate and lower temperatures are located on the edges. The table also shows that an increased thermal load will produce an increase in the overall temperature distribution.

The test plate thermal resistance was investigated for its possible use as a design tool in future test plates. Thermocouple number three's thermal resistance was investigated because its central location would produce the greatest amount of thermal

resistance. The thermal resistance as function of varied heat flux for thermocouple three in experiments 3, 4, 5, and 6 can be seen in figures 72, 73, 74 and 75 respectively.

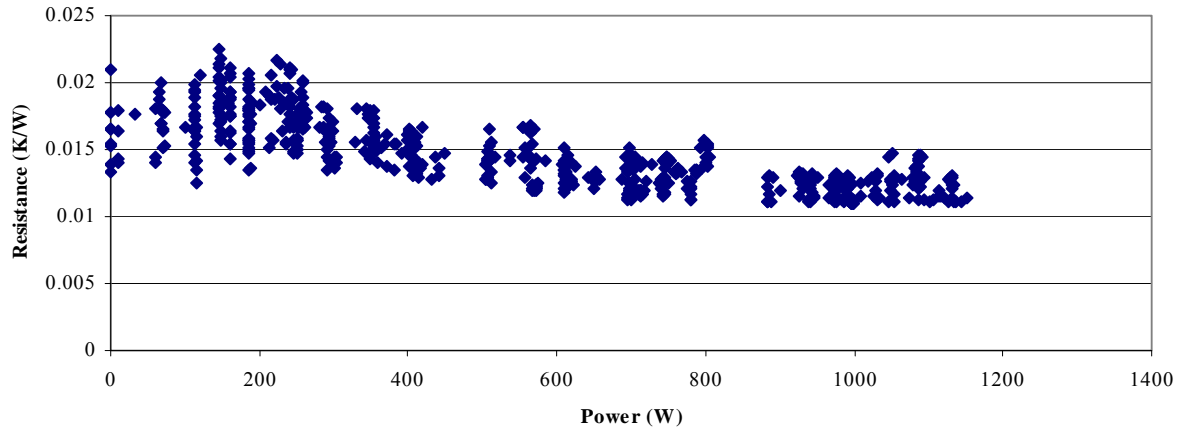


Figure 72. Experiment three thermocouple three thermal resistance

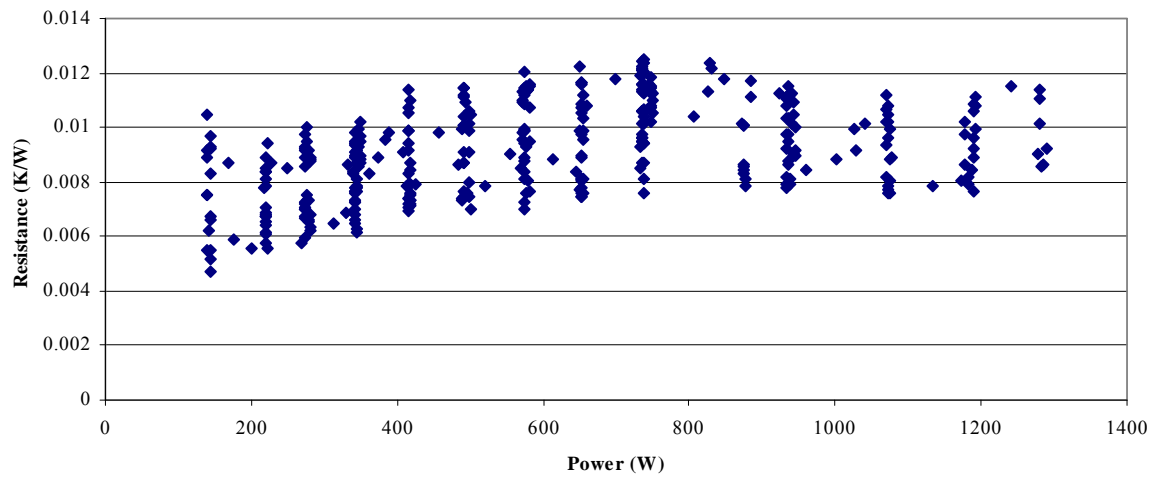


Figure 73. Experiment four thermocouple three thermal resistance

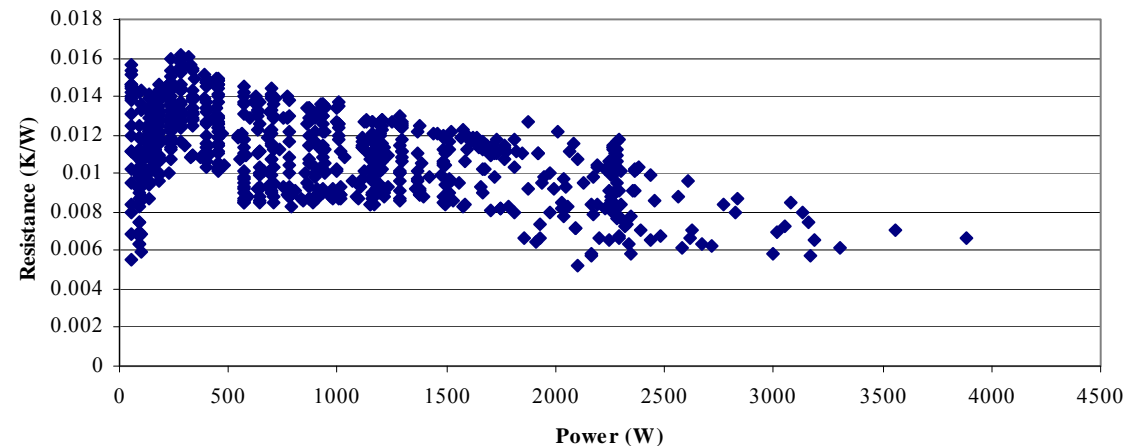


Figure 74. Experiment five thermocouple three thermal resistance

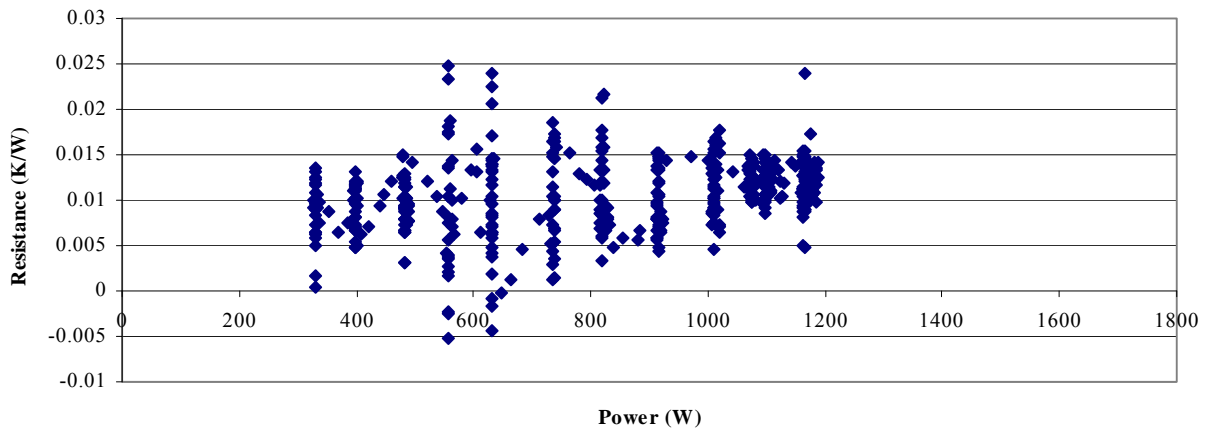
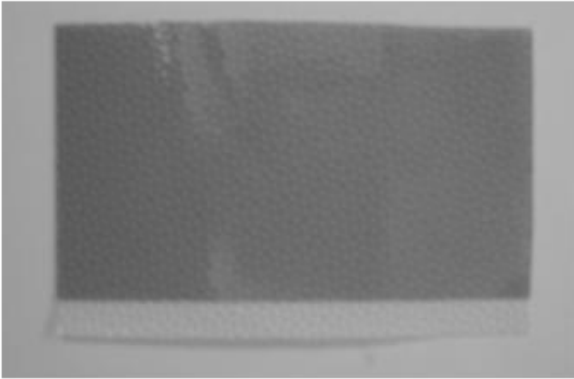


Figure 75. Experiment six thermocouple three thermal resistance

The figures indicate that thermal resistance resides within a range centered around 0.01 K/W. The maximum value recorded during testing was approximately 0.02 K/W. The figures also show that thermal resistance in the test plate rises to a maximum and then begins to decrease as a function of thermal load.

The decrease in the thermal resistance occurs because the Kapton film and its adhesive backing undergo a physical change. An increase in the temperature of the Kapton film causes it to become more pliable thus contouring to both the plate and the heater wire. The increased temperature also softens the Kapton's adhesive backing which helps eliminate any air pockets that maybe in the heater. Figure 76 shows the difference in the Kapton before heating and testing and after.



Before heater use: notice the bumps in the Kapton.



After heater use: notice the smoothness of the Kapton

Figure 76. Kapton before and after testing

Figure 76 shows that there is pattern indented on the Kapton produced during the manufacturing process. The patterned indentation creates a surface on the Kapton that creates area with air pockets which would decrease the thermal resistance. Figure 76 also indicates that the patterned indentation on the Kapton has disappeared after heating and that it is now a totally smooth surface. The smoothing of the Kapton along with the physical changes in the adhesive are the driving factors behind the decrease in the thermal resistance.

Plate Target Numerical and Experimental Comparison

A comparison of the temperature results from the experimental test plates and the numerical temperature gradients was done to help add validity to the numerical model. A heat transfer coefficient was estimated using the mass flow rate of the flow through the system and Fluent. A mass flow rate equal to 2.6 kg/s was used as the flow rate through the system which is equal to 1.26 m/s test section entrance velocity. The velocity along

the vertical length of the target was averaged with a value of 3.86 m/s which translates to a heat transfer coefficient of 9918.3 W/mK.

The temperature distribution from experiment five was used as a comparison for Algor model. The boundary conditions applied to the Algor model were an external heat transfer coefficient of 9918.3 W/mK, a 1.5mm thickness plate and a 2300W internal heat flux. Figure 77 shows the temperature distributions created by the Algor model.



Figure 77. Algor simulation of the experimental test plates

The greatest temperatures are the gray areas in the center, equal to 38.6 °C and the dark areas on the corners represent the lowest temperatures, equal to 24.8 °C. Table 15 compares the temperatures of the test plate to the numerical results.

Table 15. Comparison of experimental and numerical experiments of the plate

| | <i>TC 1 (°C)</i> | <i>TC 2 (°C)</i> | <i>TC 3 (°C)</i> | <i>TC 4 (°C)</i> | <i>TC 5 (°C)</i> |
|-----------------------------|------------------|------------------|------------------|------------------|------------------|
| Experimental Results | 35.8 | 33.4 | 44.3 | Failure | 32.7 |
| Numerical Results | 34.2 | 34.2 | 38.6 | 34.2 | 34.2 |

The table comparison indicates that temperature gradients in the experimental test plate and the numerical model are close but not exactly the same. Averaging the heat transfer coefficient over the length of the target, preexisting wrapping in the plate, potential unknown air gaps and initial fabrication could have contributed the discrepancies.

Chapter 7: Conclusions

The purpose of the research performed in this thesis was to evaluate the thermal mechanical behavior of several LEU based molybdenum-99 processing geometries. An examination of the targets using analytical, numerical and experimental studies was performed to estimate the thermal contact resistance and to assess the risk of failure. The data collected from the studies was compared and summarized to examine trends.

The cylindrical target investigation aimed to develop a correct testing methodology to evaluate the thermal contact resistance in the target. The data indicated that an internally applied heat flux would be put the target in an overly optimistic state leading to a low thermal contact resistance. An externally applied heat flux creates a tensile force at the cylinder's interface. The tensile force at the interface will increase the thermal contact resistance and decrease the contact pressure. The results indicate that the procedure used by Areva-Cerca to characterize the thermal contact resistance is questionable and the externally applied heat flux should be used to characterize the thermal contact resistance correctly.

The plate target investigation examined the thermal mechanical behavior during simulated LEU heating. An analytical model was developed to investigate the natural tendencies that develop in the target when subjected to a thermal gradient. The analytical model found that a un-weld plate will not display pillowing during heating. The numerical model examined the behavior of the target during internal heating and developed a performance map. The study found that edge boundary conditions will play a significant role in the deflections and stress that develop. The deflection and stress also depend heavily on the internal heat flux and fission gas pressure. There are also certain

conditions that will create a deflection greater than $35\mu\text{m}$. An experimental setup was developed in conjunction with the other models to test simulation plates. Temperatures collected inside the target at a 2.4kW thermal load indicate no signs of separation thus far. Comparison of the temperature data to the numerical results showed that the temperature distributions are similar. All results collected were organized into a performance map which will be used in future studies

Chapter 8: Recommendations

Several limiting factors controlled the results of the various investigations. In the cylindrical target numerical model an increase in the convergence was attempted. This however increased the amount of computational power required for the analysis. The computer facilities that were available could not handle the increased complexity of the problems. In future studies a computer with greater memory and speed should be used.

The experimental setup of the plate target was limited to only 5kW because of the electrical voltage available in the laboratory. The current voltage available is only 240V limiting the thermal load that can be applied to the target. A larger voltage source such as a 480V line should be utilized in future investigations to help investigate the possibility of internal separation. The wire used in the Kapton heaters sent to Y-12 for processing should be used when it returns. An increase in the surface area of wire should help counteract the previously seen heat spreading issues. Work should continue on improving the ability of the external wire leads to expel their energy. These two adjustments should increase the thermal load to the desired 5kW thermal load.

Appendix 1: Matlab code

A. Analytical code for the cylindrical target

Inner Surface Heating

```
clear
clc
%Material Properties and conditions
E=6.8947e10; %Youngs modulus Pa
pr=0.3; %posions ratio
alp=2.34e-5; %coeffiecent of thermal exspansion
k=180.073; %W/mK Thermal conductivity
h=21740; %heat transfer coeffient
tinf=323; %temperature of the room K

%Cylinder Deminsions
a=0.01321; %inner radius
b=0.015075; %outer radius
%r=0.01411;
radius=linspace(0.01321,0.015075);

i=1;
while i<=length(radius)

r=radius(i);
%Heat flux
qflux=1000000; %Per unit area

%Mathmatica solution
tr1=((-a*b*log(qflux*a))/k)-((a*qflux*a^2)/(2*b*h))-
((tinf*a^2)/2)+((a*b*log(qflux*r))/k)+((a*qflux*r^2)/(2*b*h))+((tinf*r^
2)/2);
tr2=((-a*b*log(qflux*a))/k)-((a*qflux*a^2)/(2*b*h))-
((tinf*a^2)/2)+((a*b*log(qflux*b))/k)+((a*qflux*b^2)/(2*b*h))+((tinf*b^
2)/2);

stress_r_math=(E/(1-pr))*((-alp/r^2)*tr1+((r^2-a^2)*alp)/(r^2*(b^2-
a^2)))*tr2);

%Solbrekken solution

qbar=(qflux*a)/k;
inv_bi=k/(h*b);
tr11=(tinf+qbar*log(b)+qbar*inv_bi+(qbar/2))*((r^2-a^2)/2)-
(qbar/2)*log((r^(r^2))/(a^(a^2))); %Temperature from the innner radius
to the desired position
tr22=(tinf+qbar*log(b)+qbar*inv_bi+(qbar/2))*((b^2-a^2)/2)-
(qbar/2)*log((b^(b^2))/(a^(a^2))); %Temperature from the inner radius
to the outer radius

stress_r(i)=(E/(1-pr))*((-alp/r^2)*tr11+((r^2-a^2)*alp)/(r^2*(b^2-
a^2)))*tr22);
```

```

strain_r(i)=(1+pr)*alp*(tinf+qbar*log(b/r)+inv_bi)-
(((tinf+qbar*log(b)+qbar*inv_bi+(qbar/2))*((r^2-a^2)/2)-
((qbar/2)*log((r^r^2)/(a^a^2))))/r^2);

Temp_yo(i)=tinf+(qbar*(log(b/r)+inv_bi));

i=i+1;

end

figure(1)
plot(radius, stress_r);
xlabel('Radius (mm)')
ylabel('Stress (Pa)')
title('Inner Surface Heating Condition Stress')

figure(2)
plot(radius, strain_r);
xlabel('Radius (mm)')
ylabel('Strain ')
title('Inner Surface Heating Condition Strain')

figure(3)
plot(radius, Temp_yo);
xlabel('Radius (mm)')
ylabel('Temperature (K)')
title('Inner Surface Heating Condition Temperature')

fid=fopen('inner.txt','w');
for i=1:length(stress_r)
fprintf(fid, '%g %g \n', stress_r(i), radius(i));
end
fclose(fid)

```

Outer Surface Heating

```

clear
clc
%Material Properties and conditions
E=6.8947e10; %Youngs modulas Pa
pr=0.3; %posions ratio
alp=2.34e-5; %coeffiecent of thermal exspansion
k=180.073; %W/mK Thermal conductivity
h=29306; %heat transfer coefficient
tinf=323; %temperature of the room K

%Cylinder Deminsions
a=0.01321; %inner radius
b=0.015075; %outer radius
r=0.01411;
radius=linspace(0.01321,0.015075);
%Heat flux
qflux=1000000; %Per unit area

```

```

%Stress and Strain
i=1;
while i<=length(radius)

r=radius(i);

qbar=(qflux*b)/k;
inv_bi=k/(h*a);

tr11=(tinf+qbar*log(a)+qbar*inv_bi+(qbar/2))*((r^2-
a^2)/2)+(qbar/2)*log((r^(r^2))/(a^(a^2)));
tr22=(tinf+qbar*log(a)+qbar*inv_bi+(qbar/2))*((b^2-
a^2)/2)+(qbar/2)*log((b^(b^2))/(a^(a^2)));

stress_r(i)=(E/(1-pr))*((-alp/r^2)*tr11+((r^2-a^2)*alp)/(r^2*(b^2-
a^2)))*tr22);

%stress_z(i)=((alp*E)/(1-pr))*(2/(b^2-a^2))

strain_r(i)=((1+pr)*alp*(tinf+qbar*log(b/r)+inv_bi)-
((tinf+qbar*log(b)+qbar*inv_bi+(qbar/2))*((r^2-a^2)/2)-
((qbar/2)*log((r^r^2)/(a^a^2))))/r^2));

Temp_yo(i)=tinf+(qbar*(log(r/a)+inv_bi));

i=i+1;

end

figure(1)
plot(radius, stress_r);
xlabel('Radius (mm)')
ylabel('Stress (Pa)')
title('Outer Surface Heating Condition Stress')

figure(2)
plot(radius, strain_r);
xlabel('Radius (mm)')
ylabel('Strain ')
title('Outer Surface Heating Condition Strain')

figure(3)
plot(radius, Temp_yo);
xlabel('Radius (mm)')
ylabel('Temperature (K)')
title('Outer Surface Heating Condition Temperature')

fid=fopen('outer.txt','w');
for i=1:length(stress_r)
fprintf(fid, '%g %g \n', stress_r(i), radius(i));
end
fclose(fid)

```

B. Matlab m-file used to find stress values for Madhusudana

```
%Mad_data
clear
%Nomenclature for whole solution
a=0.009; %inner radius
b=0.010; %interface radius
c=0.011; %outer radius
k=30.5; %harmonic mean k

%Aluminum properties
Ea=70000; %Young's (MPa)
Ha=1400;%Microhard (Mpa)
aa=24*10^(-6); %Coefficient of Expansion
ka=200; %Thermal Conductivity (W/mK)
va=0.33; %Poisson's ratio

%Steel properties
Es=200000; %Young's (MPa)
Hs=2750;%Microhard (Mpa)
as=18*10^(-6); %Coefficient of Expansion
ks=16.5; %Thermal Conductivity (W/mK)
vs=0.28; %Poisson's ratio

%Air properties
kair=0.0298;%Thermal Conductivity (W/mK)

%i=-1.5; % ss->al
i=1.5; %al->ss
%i=1.5; %ss->ss
%i=2.5; %al->al

%Plot of Contact Pressure and thermal contact conductance
if -1>i ; % ss->al
    ai=as; %inner COE
    ao=aa; %outer COE
    rough=0.000003; %roughness
    ki=ks; %thermal cond. of inner
    ko=ka; %thermal cond. of outer
    vi=vs; %Poisson's ratio inner
    vo=va; %Poisson's ratio outer
    ei=Es; %Young's (GPa) inner
    eo=Ea; %Young's (GPa) outer
elseif i>1; %al->ss
    ai=aa; %inner COE
    ao=as; %outer COE
    rough=0.000003; %roughness
    ki=ka; %thermal cond. of inner
    ko=ks; %thermal cond. of outer
    vi=va; %Poisson's ratio inner
    vo=vs; %Poisson's ratio outer
    ei=Ea; %Young's (GPa) inner
    eo=Es; %Young's (GPa) outer
% elseif 1<i<2; %ss->ss
%     ai=as; %inner COE
```

```

%      ao=as; %outer COE
%      rough=0.000003; %roughness
%      ki=ks; %thermal cond. of inner
%      ko=ks; %thermal cond. of outer
%      vi=vs; %Poisson's ratio inner
%      vo=vs; %Poisson's ratio outer
%      ei=Es; %Young's (GPa) inner
%      eo=Es; %Young's (GPa) outer
% elseif 2<i<3; %al->al
%      ai=aa; %inner COE
%      ao=aa; %outer COE
%      rough=0.000003; %roughness
%      ki=ka; %thermal cond. of inner
%      ko=ka; %thermal cond. of outer
%      vi=va; %Poisson's ratio inner
%      vo=va; %Poisson's ratio outer
%      ei=Ea; %Young's (GPa) inner
%      eo=Ea; %Young's (GPa) outer
end

theta=10; %on graph
n=0.85; %assume from paper

%Constant C's
c1=(ei/eo)*(((c^2+b^2)/(c^2-b^2))+vo)+(((b^2+a^2)/(b^2-a^2))-vi);
%From the article
c2=(ai/(2*log(b/a)))*((1-((2*a^2)/(b^2-a^2))*log(b/a))-
((ao*ki)/(ai*ko))*(1-((2*c^2)/(c^2-b^2))*log(c/b)));
%From book
c2=(((1/(2*log(b/a)))*((1-((2*a^2)/(b^2-a^2))*log(b/a)))-
(((ao*ki)/(ai*ko))*(1-((2*c^2)/(c^2-
b^2))*log(c/b))*(log(c/b)/log(b/a))*(1/(2*log(c/b))))));
%my solved one from the article
c2=(((ai)/(2*log(b/a)))*((1-((2*a^2)/(b^2-a^2))*log(b/a)))-
(((ao)/(2*log(c/b)))*((1-((2*c^2)/(c^2-
b^2))*log(c/b))*(ki/ko)*(log(c/b))/(log(b/a))));
c3=0.55; %assume from paper
c4=(ai-ao);
c5=ki/(b*log(b/a));
c6=c3*(tand(theta))*(k/rough)*(1/Ha)^n;
c7=kair/(3*rough);

%Produce plot for Pressure
%First temp grad across inner cylinder
for dTi=2:2:10;
uab=dTi*c2;
ucb=0;
j=1;
for Ta=25:25:300;
Ta_1(j)=Ta;
c8=c1*ei*(uab+ucb)+c4*(Ta-dTi)*c1*ei;
%Obtain Pressure from newton raphson
[press]=mynewton(@fun_s,0.0005,100,10^-8,c8,dTi,Ta);
if press<=0 %eliminates (-) numbers
press=0;
end

```

```

    press1(j)=press;
    %Obtain h value

h(j)=((c3*(tand(theta)))*(k/rough)*(press1(j)/Ha)^n+kair/(3*rough));

    %plot pressure and h
    subplot(2,1,1);plot(Ta_1,press1);
    if i<1
        title('Max Temperature Rise vs. Contact Pressure for ss-
>al');
    elseif i>1
        title('Max Temperature Rise vs. Contact Pressure for al-
>ss');
    end
    xlabel('Max Temperature Rise (K)');
    ylabel('Contact Pressure (MPa)');
    hold all
    subplot(2,1,2);plot(Ta_1,h);
    if i<1
        title('Max Temperature Rise vs. Thermal Contact Conductance
for ss->al');
    elseif i>1
        title('Max Temperature Rise vs. Thermal Contact Conductance
for al->ss');
    end
    xlabel('Max Temperature Rise (K)');
    ylabel('Thermal Contact Conductance');
    Ta=Ta+15;
    j=j+1;
    hold all
    end
end

```

Appendix 2: Algor Plate Procedure

Modeling and analysis in Algor is similar to the process used in Pro-Mechanica. The geometry used in Algor was created in Autodesk Inventor. The geometry was created by opening Inventor and selecting the open new file button in the upper left hand corner. This will open the “open” window, select the Metric tab and scroll down to the Standard (mm). ipt or the proper unit type you want to use. When the new part drawing has opened select the Two point rectangle button on the 2D sketch panel. When selected you will be able to draw a two point rectangle, at this point is not important to have the exact dimensions on the rectangle, draw a general rectangle. Return to the 2D sketch panel and select General Dimension. This option will allow you to change the dimensions of the rectangle to the dimensions you require. When the correct dimensions are entered an extrusion can be done. Select 2D Sketch panel then select part features then extrude. Select the rectangle and enter a value of 1 then OK. The thickness of the part is not important and will be later changed in Algor. An example of the part can be seen in figure A1.

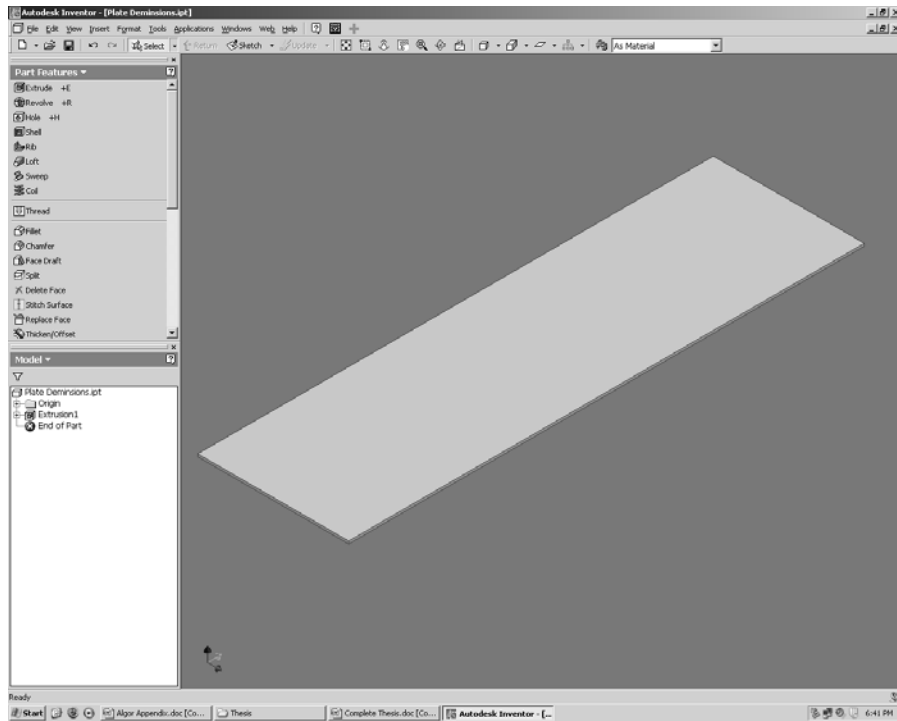


Figure A1. Part in Inventor

Save the part then go to Tools-Algor FEA-Mesh, this will open Algor and your part will automatically be imported into Algor. Note: If the analysis type is not Steady-State Heat Transfer then change it to this type.

An initial rough mesh is created by going to Mesh-Generate Mesh. The purpose of the rough mesh is to produce selection points for the creation of a two-dimensional four point mesh. The four-point mesh method is used to create a perfectly symmetric mesh. The four-point mesh is created by selecting Mesh-Structured mesh-4 point rectangular. First select the top 4 corners of the part as seen in figure A2.

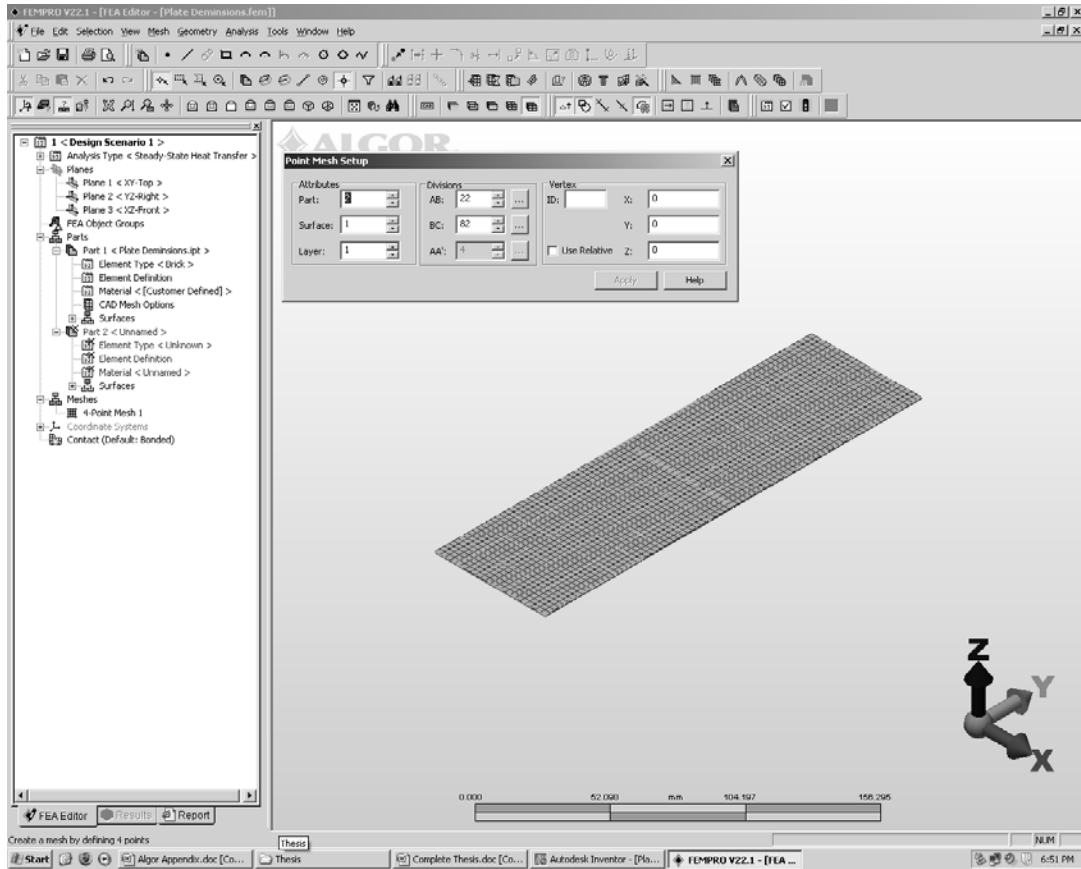


Figure A2. 2D Mesh

Change the divisions of the mesh elements to the number you require and leave the attributes alone.

When completed the four point mesh creates a single 2D surface that is the length and width of the completed plate target. The single surface must be broken into two different surfaces to apply the thermal load to appropriate interior surface area. First deactivate part 1 by right clicking on it in the model tree on the left and selecting deactivate. Now right click on the model window and click Select-Line then repeat and click Shape-Rectangle. This will allow you to select the elements that you want to use as the interior heat flux surface. Example can be seen in figure A3. Breaking the large

surface into two distinct surfaces is done by modifying the attributes of the selected mesh lines.

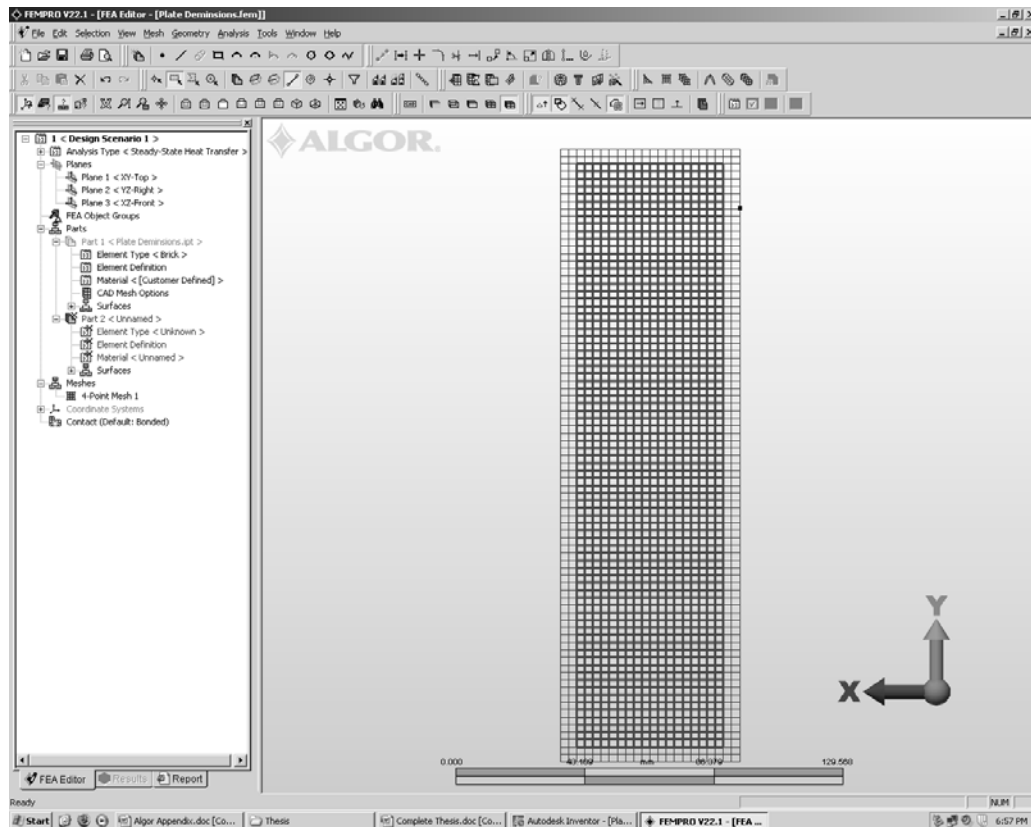


Figure A3. Heat Flux surface selection

Right click on the highlighted area and select Modify Attributes which brings up the Line Attributes window. Input the part number you just created and the next surface number available on that part.

You will now have two surfaces on the new part, as can be seen in the model tree on the left hand side of the screen. Extruding the 2D mesh into a 3D mesh is done by right clicking on the 4 point mesh icon in the model tree and selecting Move or Copy. Figure A4 shows what should be checked for an extrusion.

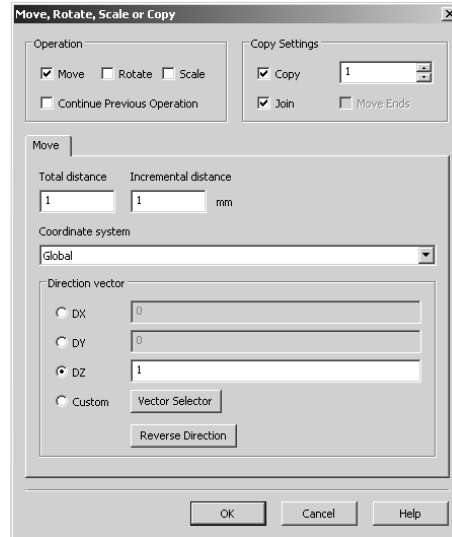


Figure A4. Mesh extrusion changes

The DZ value represents the thickness of one plate, at this point we will use a positive 1 value. When you select OK the mesh will be copied and join by new elements in to proper Z direction.

The new surfaces created need to be properly tagged. Use the view orientation buttons on the top tool bars XYZ planes views of the plate. Using the same selection settings as before and the Modify Attributes option select each surface and assign it to the proper part and surface number. Figure A5 gives an example of a surface selection in progress.

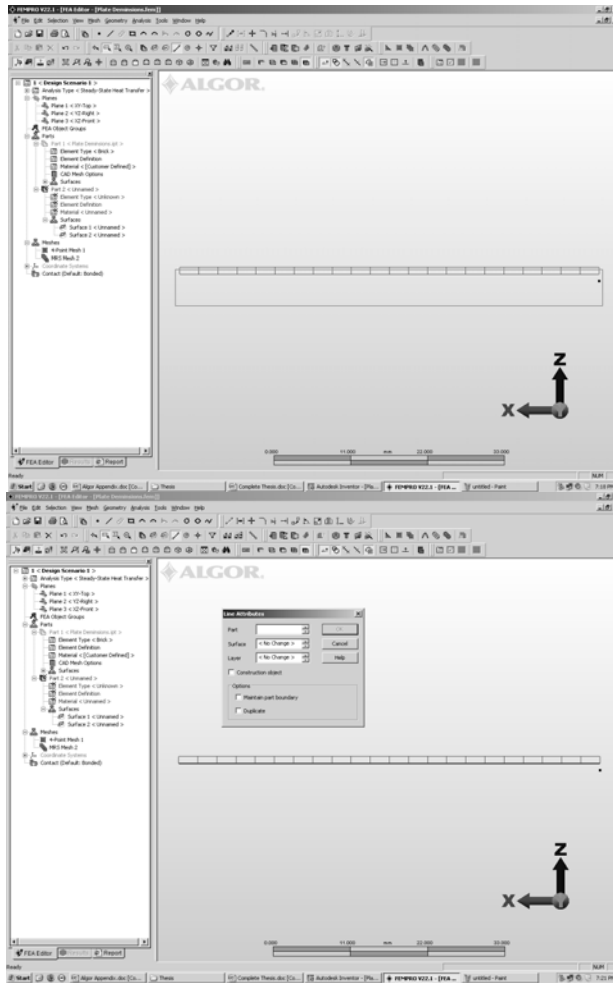


Figure A5. Mesh surface selection of bottom surface

Repeat this process for all on the surfaces on this part. When you are completed with this, right click on the element type and set it to Brick and select the proper material.

Deactivate the part you just created and reactivate the first part with the rough mesh. Repeat the previous process to create the other plate in the plate target. This time set the DZ value to the negative direction as you did the first time also when you are assigning surfaces in the new part make sure you select the Maintain part boundary in the Line Attributes window. If you do not select this then it will delete elements on the other part that is deactivated. When you are done deactivate the rough mesh part and activate

the new parts you just created. An image of the completed meshed target can be seen in figure A6

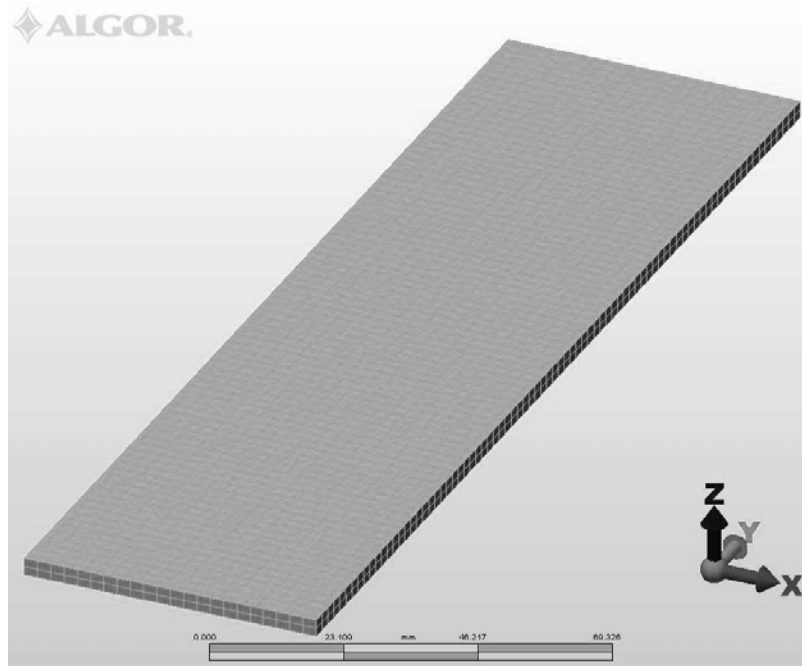


Figure A6. Completed plate target mesh in Algor

Analyzing the effects of a thermal load on the plate target is done in much of the same way as the annular target. First thermal boundary conditions are applied including the internal heat flux and the external convection coefficient. Applying the heat flux can be done by right clicking on the desired surface in the model tree then going to Add-Surface Heat Flux. The same process can be used to apply the heat transfer coefficient. The global contact condition for the static stress study was set to surface contact, which meant that the two surfaces could only move away from each other and not move into each other. The edges of the plates were set to welded meaning that they are only bonded at the point where they are in contact. Applying the individual contact conditions is done by selecting the two surfaces you want right clicking to bring up the contact conditions selection box. These will not be used in the thermal analysis but they must be applied

here for their later use in the static stress analysis. Figure A7 shows the model in the thermal mode before analysis.

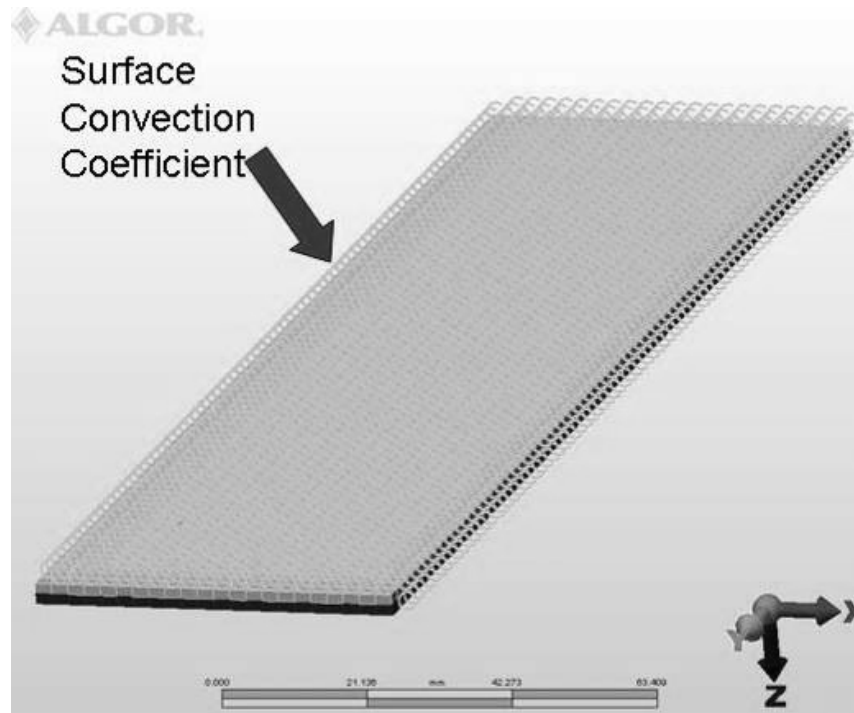


Figure A7. Plate Target model in the thermal analysis

Select Analysis-Perform Analysis to perform a thermal analysis on the model. When it is completed it will take you to the results tab. I cannot stress this enough at this point make sure to save the file in the results tab and the FEA editor tab. If you fail to do this the data will not be saved and will not get correct results in the static stress analysis.

Once it is saved return to the FEA Editor tab and right click on the Analysis Type, set it to the settings in figure A8.

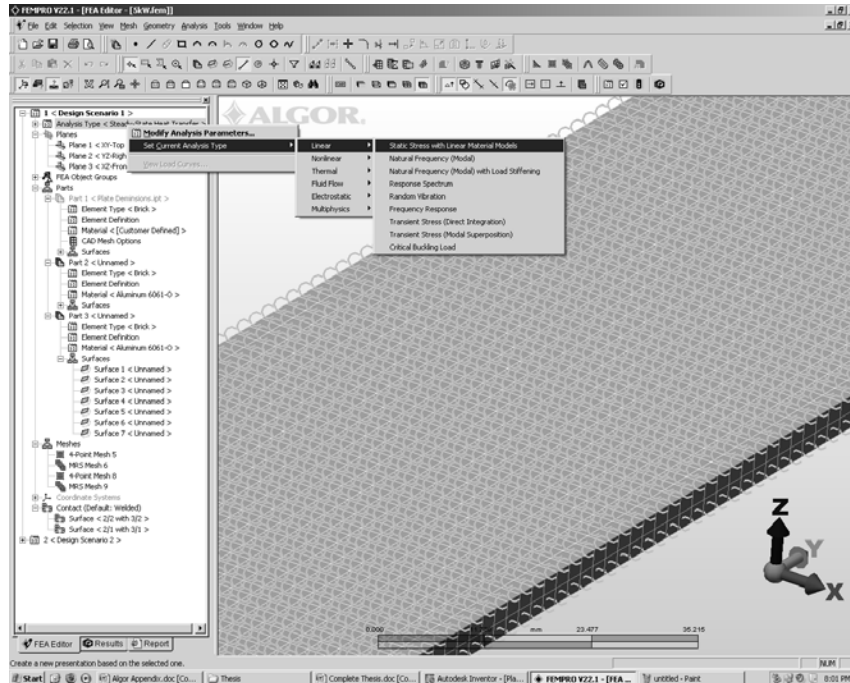


Figure A8. Changing the analysis type

This will bring up a window that will ask if you want to copy the model into a new study or not, select yes to copy the model into a new design scenario.

Apply the data from the previous thermal design study by selecting Analysis-Parameters. In the parameters window set the thermal multiplier to 1 then select the Thermal/Electrical tab. Set the default node temperature to the desired value then set the source of node temperatures to Steady State analysis. Click on the browse button to find the .to file that contains the thermal data. Note: each time you run a stress analysis you must reselect the temperature data. Select OK to exit the parameters. Apply the physical boundary conditions by right clicking on the surface and Add-Surface Boundary Condition. An example of a completed stress model can be seen in figure A9.

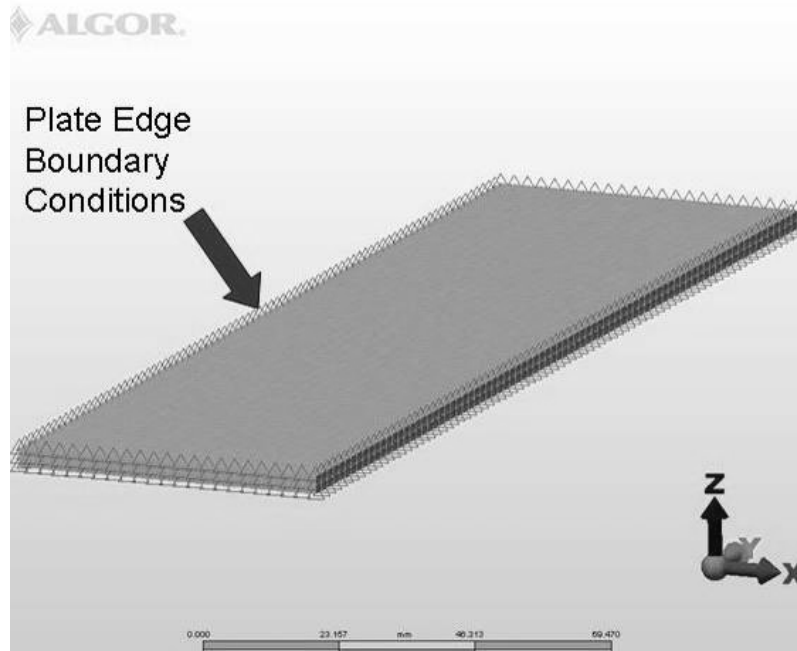
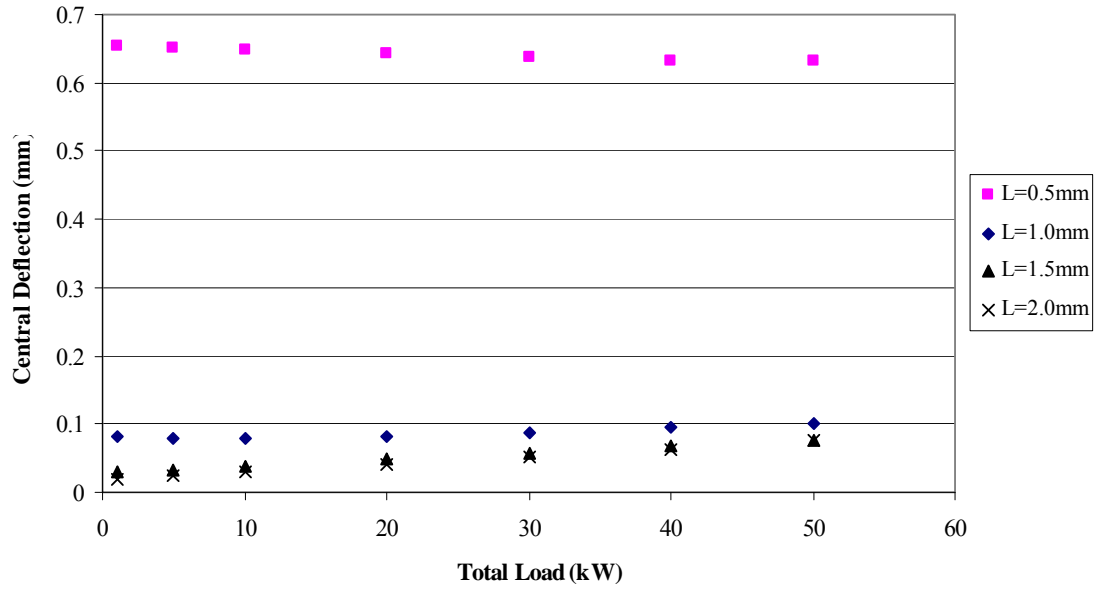


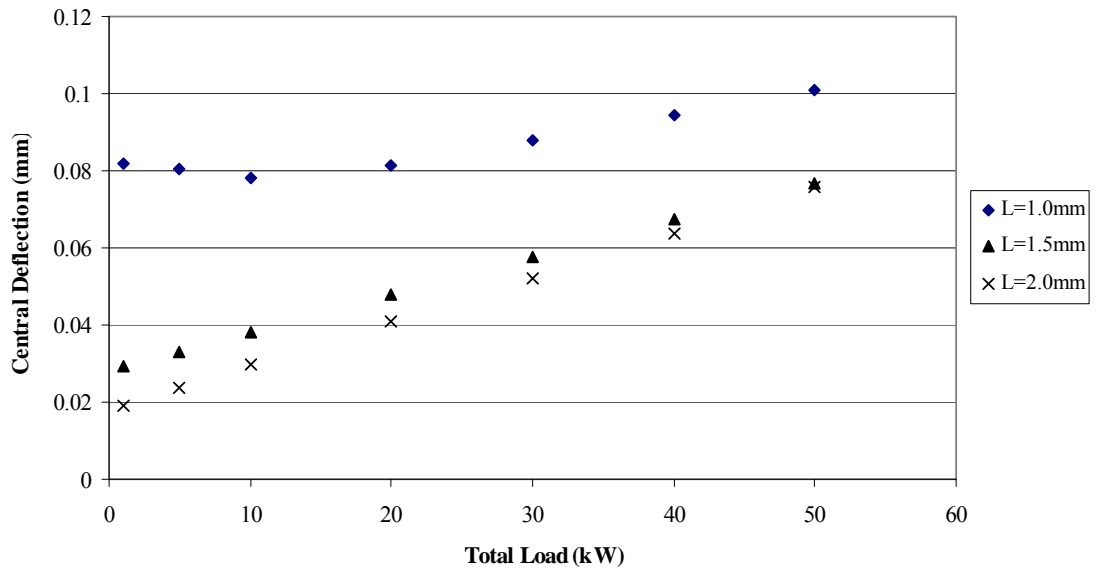
Figure A9. Plate Target model in the structural analysis

A static stress analysis with linear materials was used to find the mechanical effects of the thermal load on the target. A parametric study was done using the previously outlined procedure. The study examined the effects of varying external heat transfer coefficient, internal heat flux, thickness of the individual aluminum plates, internal fission gas pressure and the plate target edge boundary conditions.

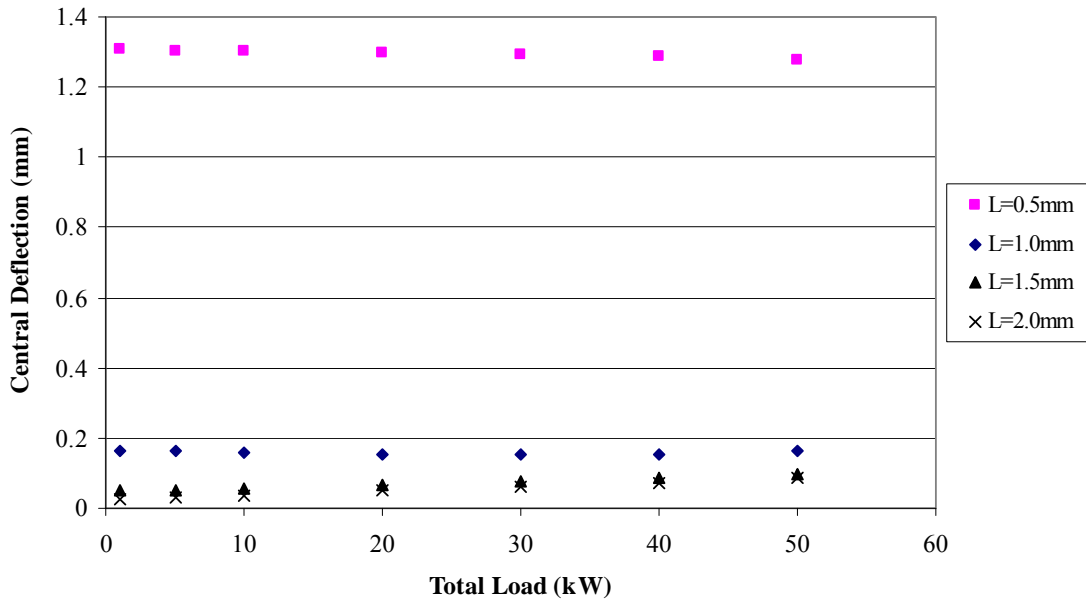
Appendix 3: Plate numerical model results partially constrained with gas pressure



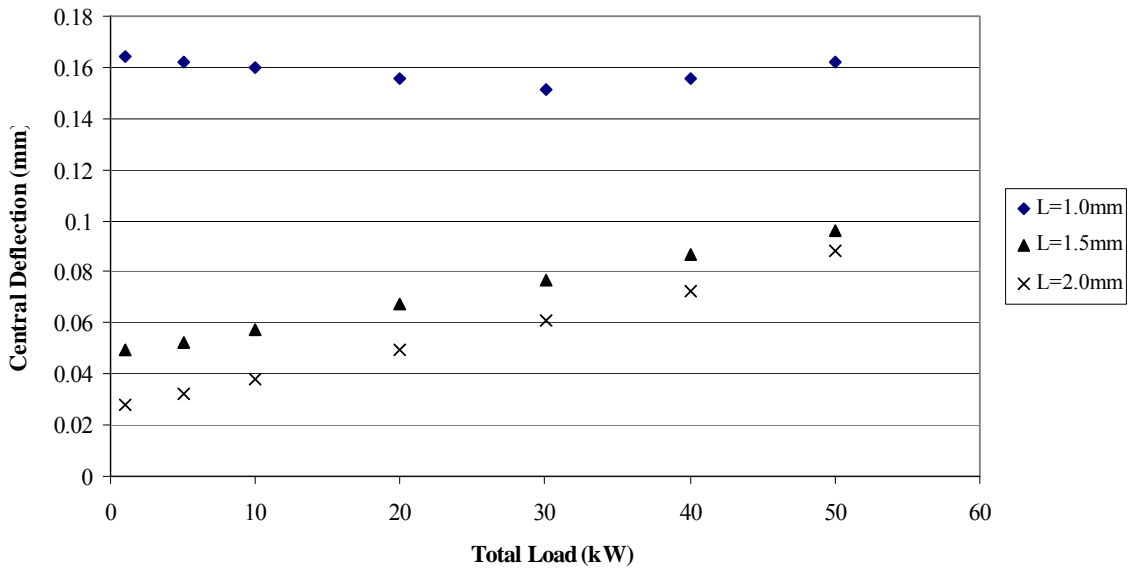
B1. Partially constrained results with a 5psi gas pressure



B2. Partially constrained results with a 5psi gas pressure and with no 0.5mm plate thickness data

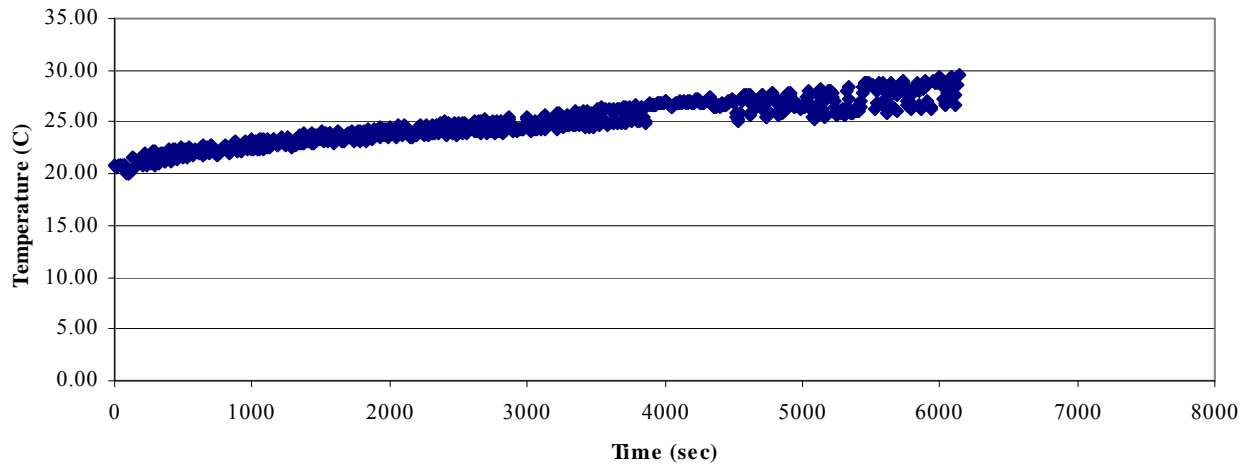


B3. Partially constrained results with a 10psi gas pressure

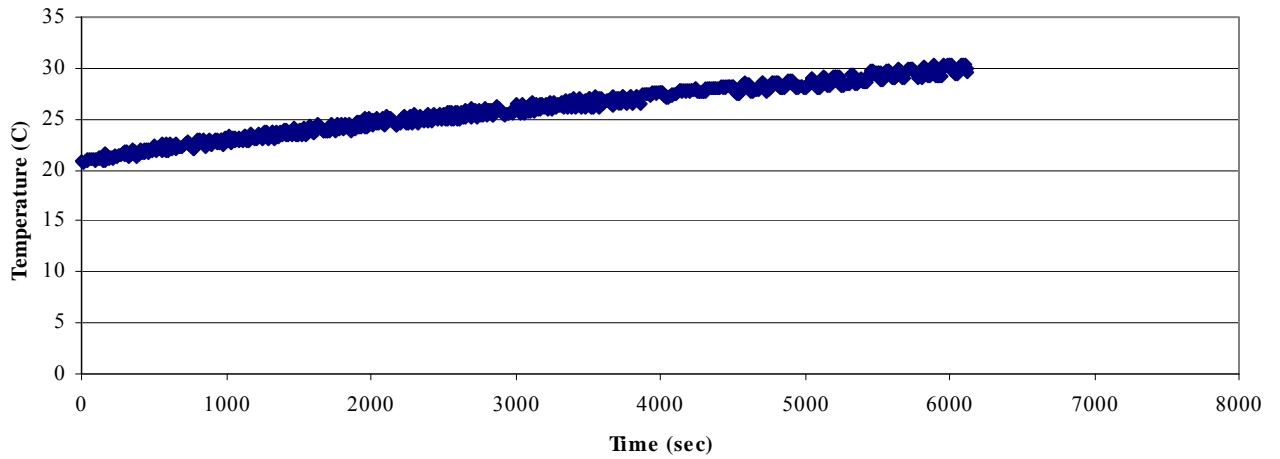


B4. Partially constrained results with a 10psi gas pressure and no L=0.5mm data

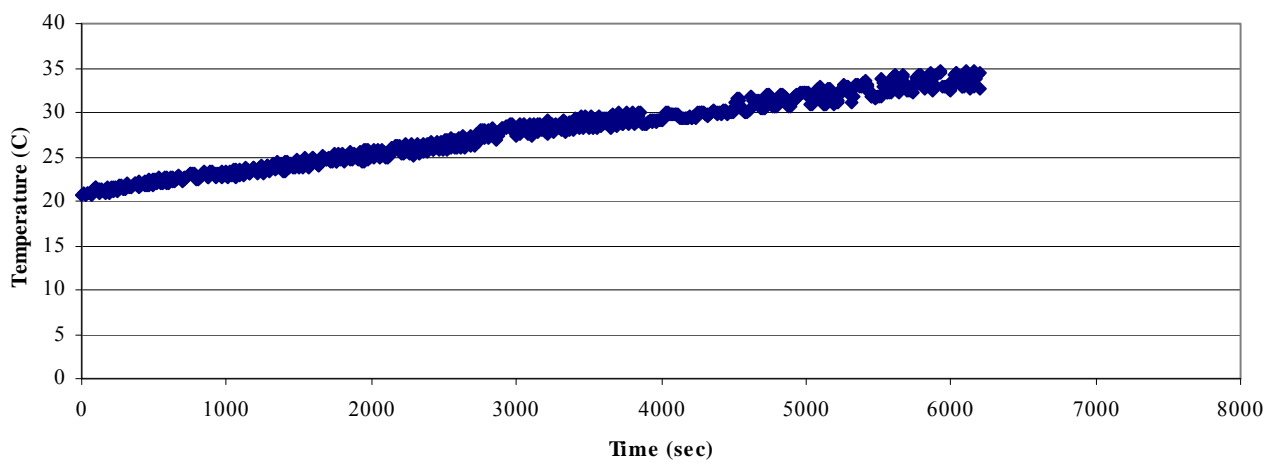
Appendix 4: Plate Experiment Results



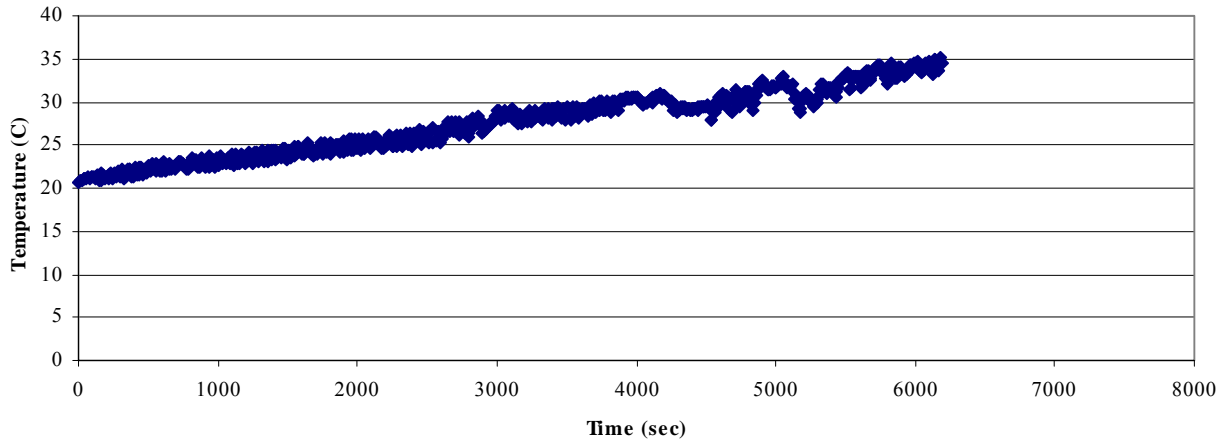
C1. Experiment 3 thermocouple 1 results



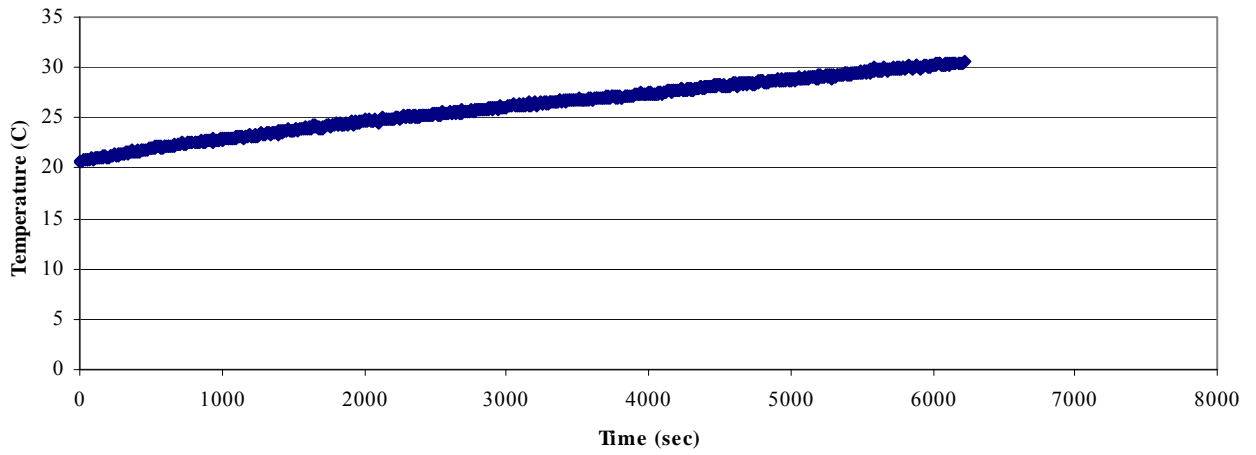
C2. Experiment 3 thermocouple 2 results



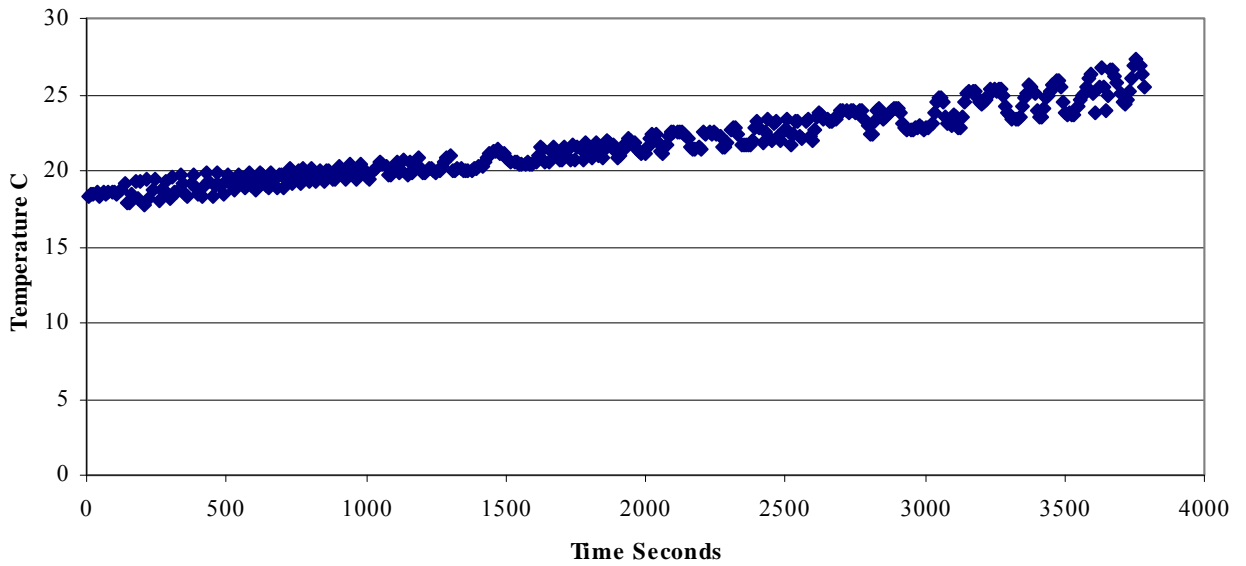
C3. Experiment 3 thermocouple 3 results



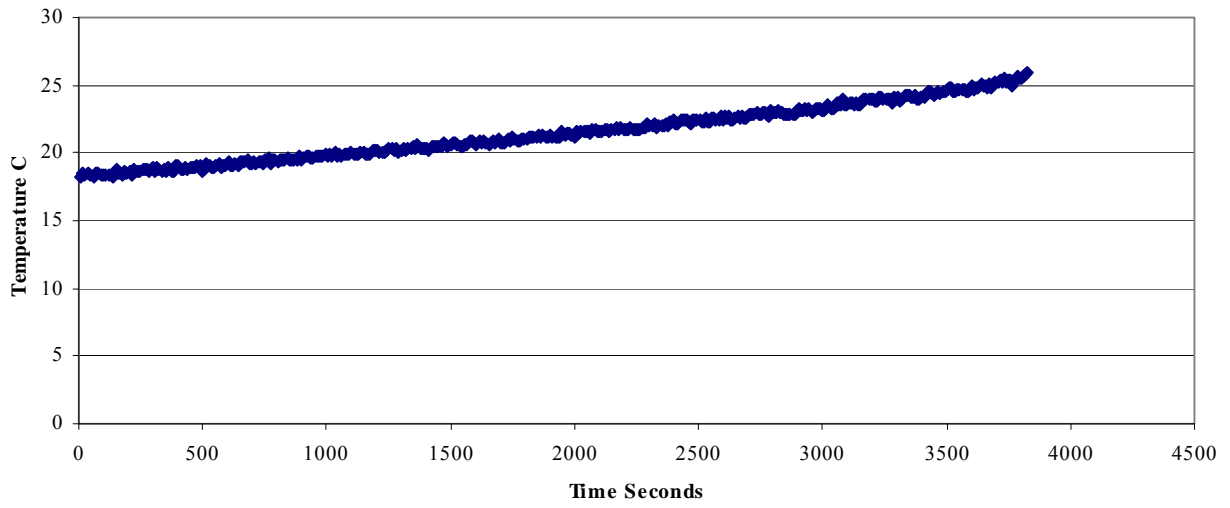
C4. Experiment 3 thermocouple 4 results



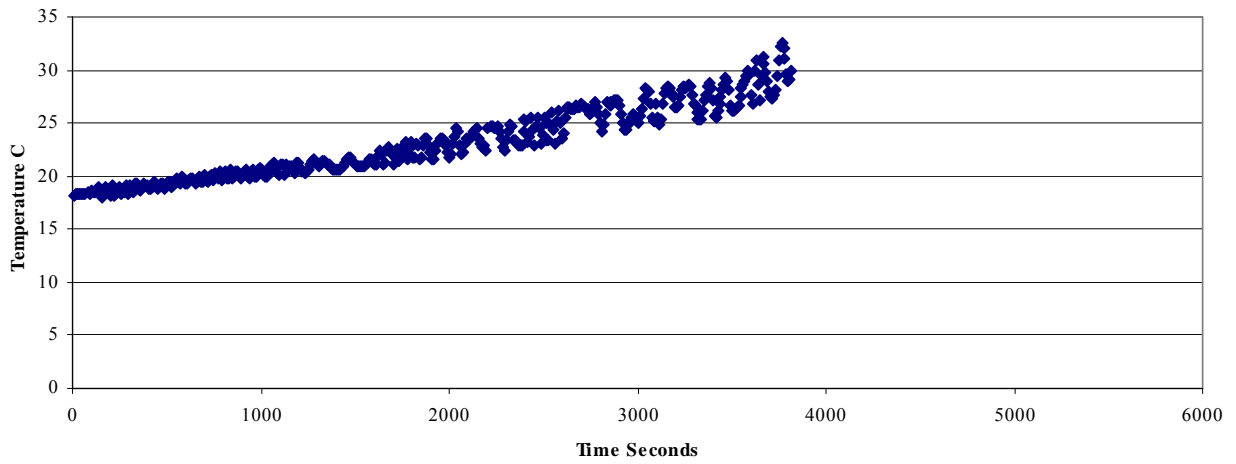
C5. Experiment 3 thermocouple 5 results



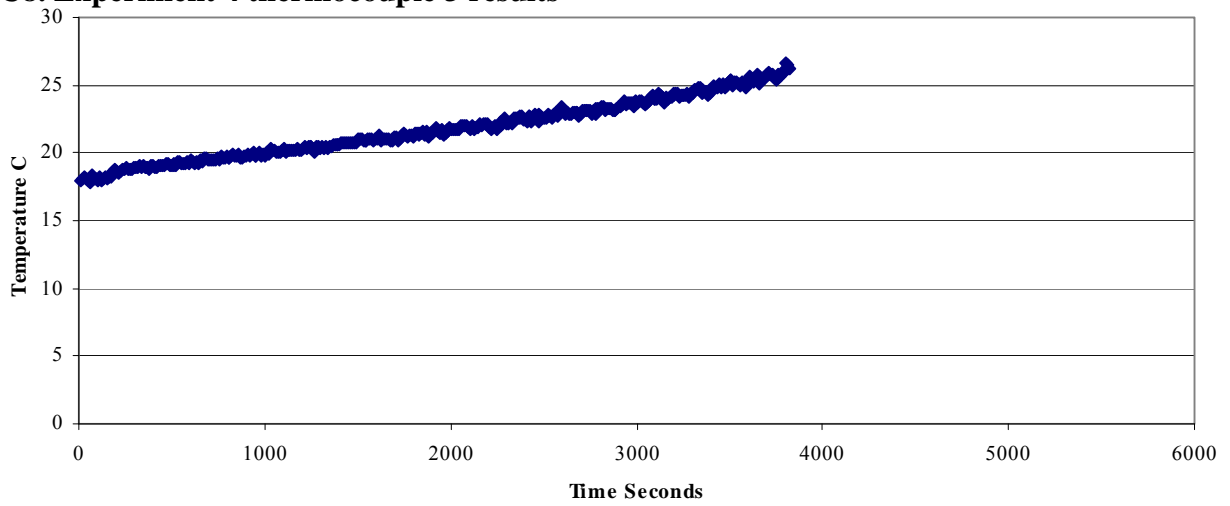
C6. Experiment 4 thermocouple 1 results



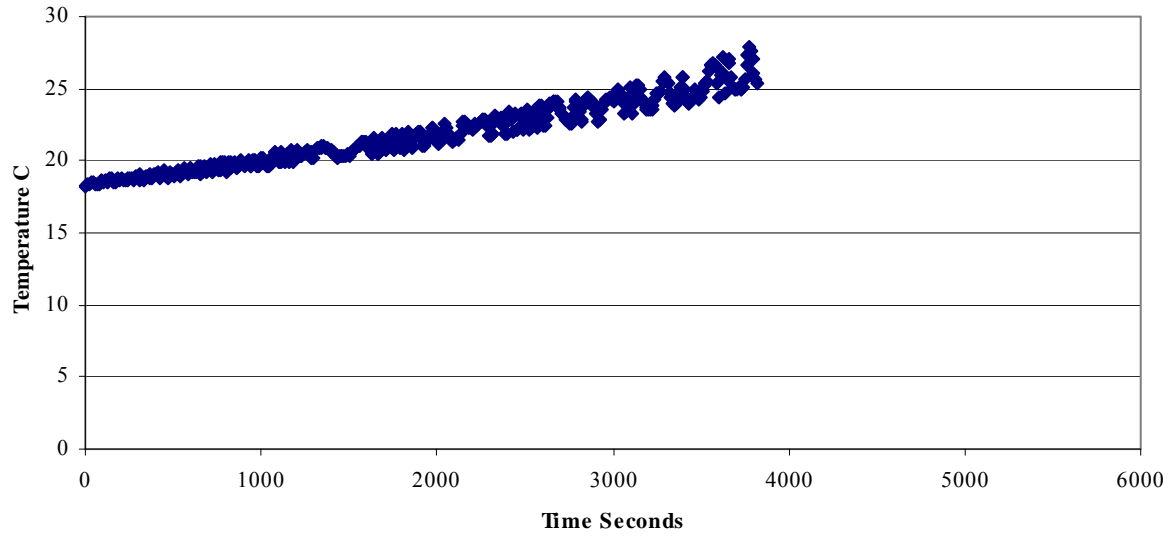
C7. Experiment 4 thermocouple 2 results



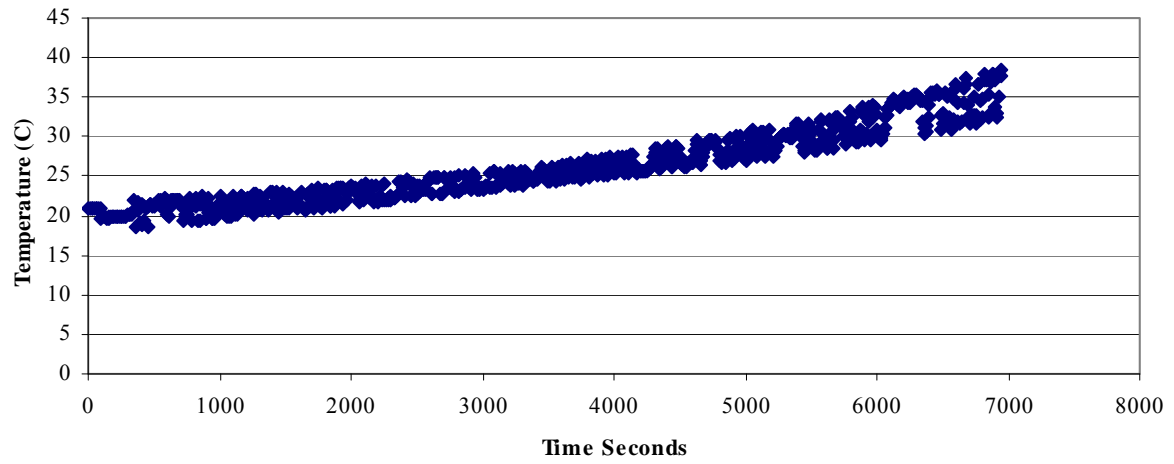
C8. Experiment 4 thermocouple 3 results



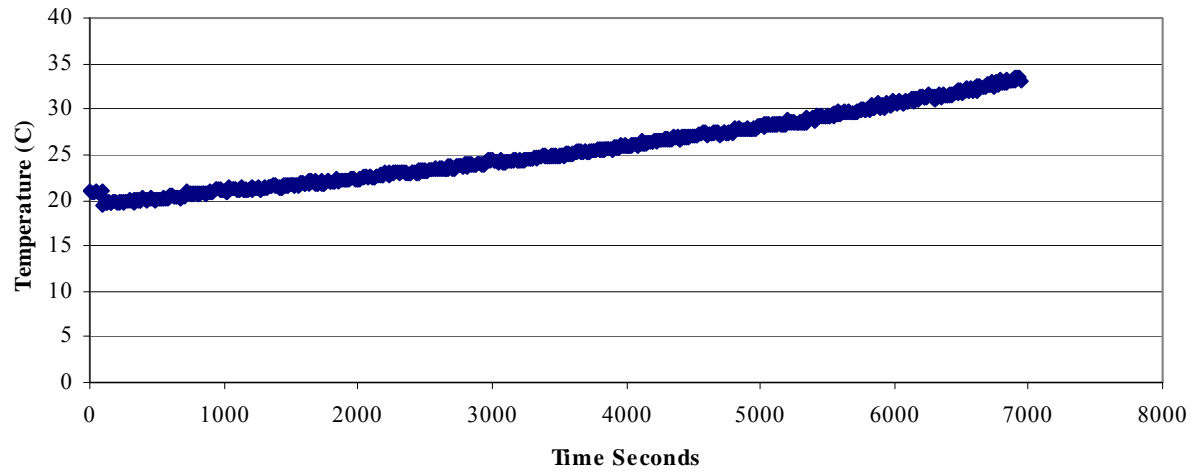
C9. Experiment 4 thermocouple 4 results



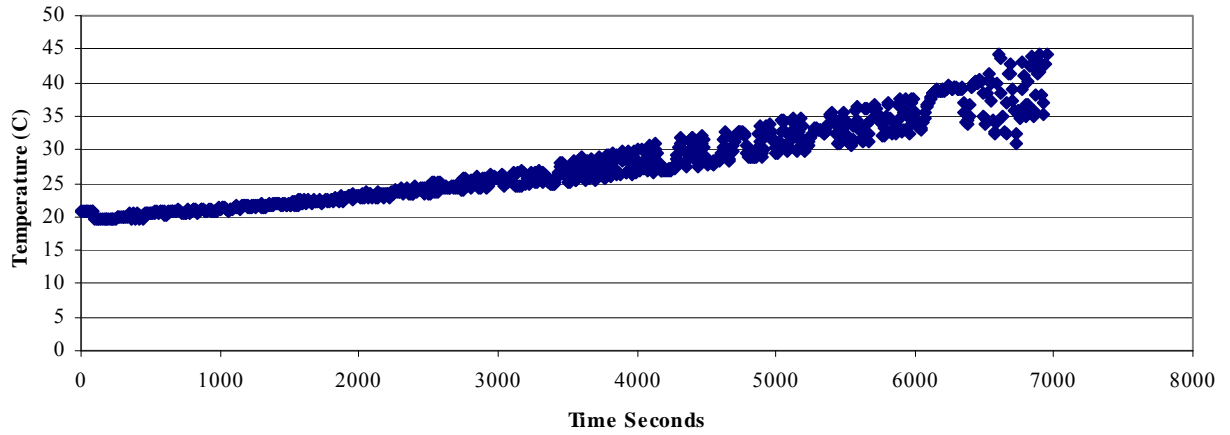
C10. Experiment 4 thermocouple 5 results



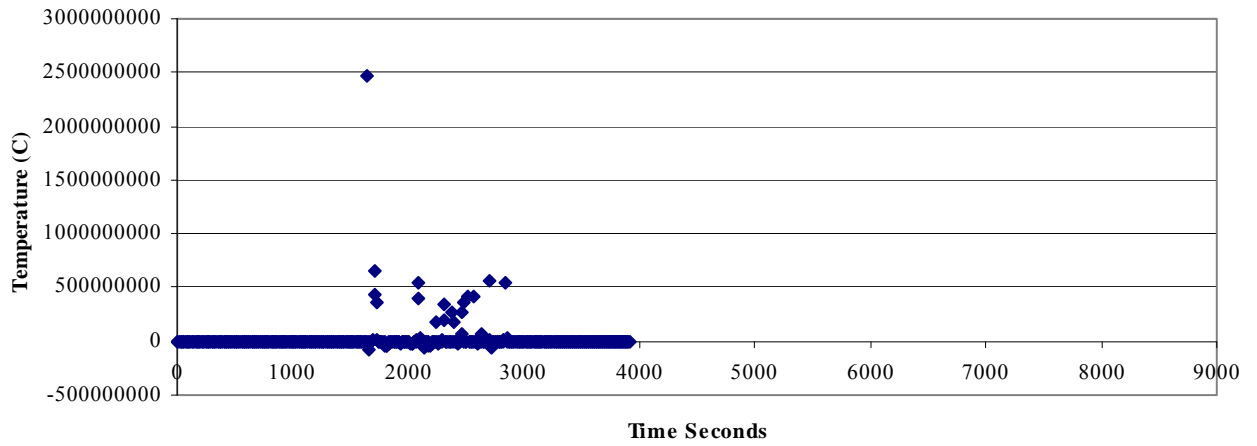
C11. Experiment 5 thermocouple 1 results



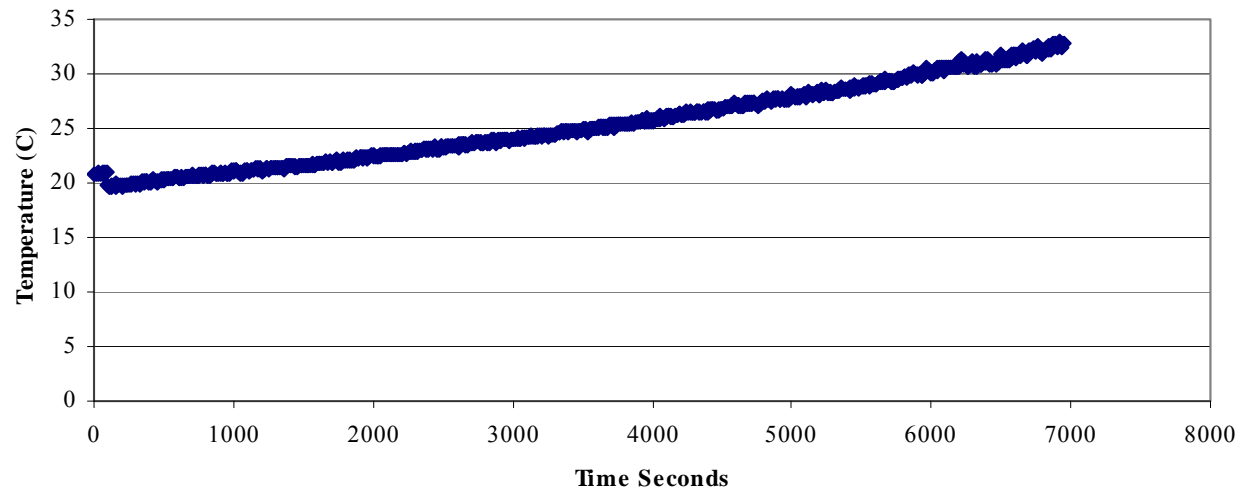
C12. Experiment 5 thermocouple 2 results



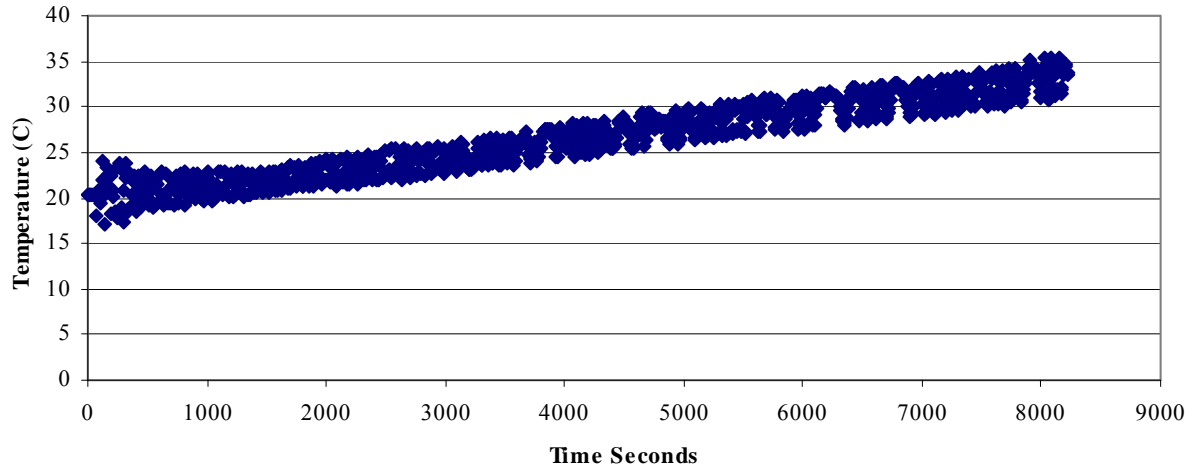
C13. Experiment 5 thermocouple 3 results



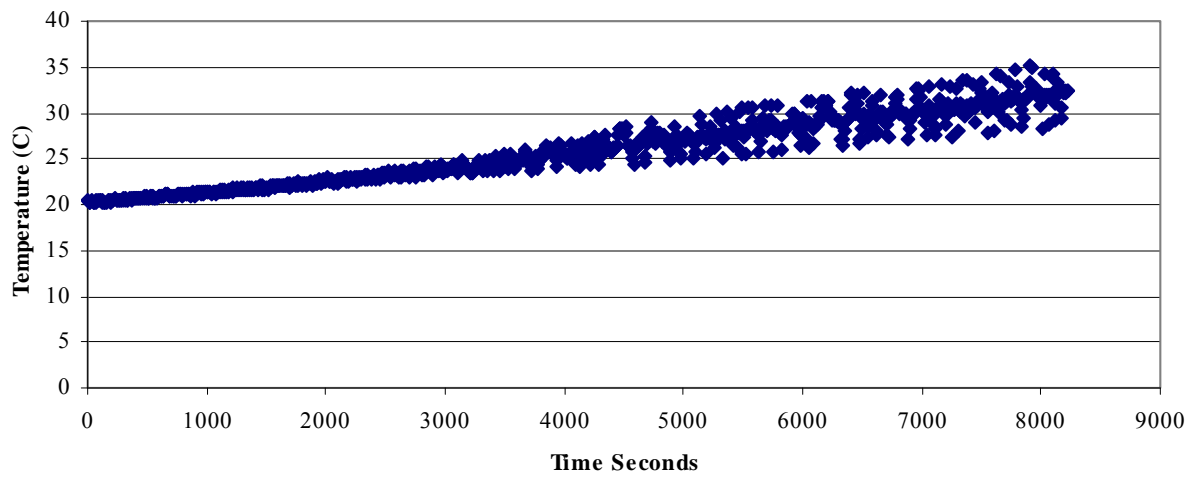
C14. Experiment 5 thermocouple 4 results failed during testing



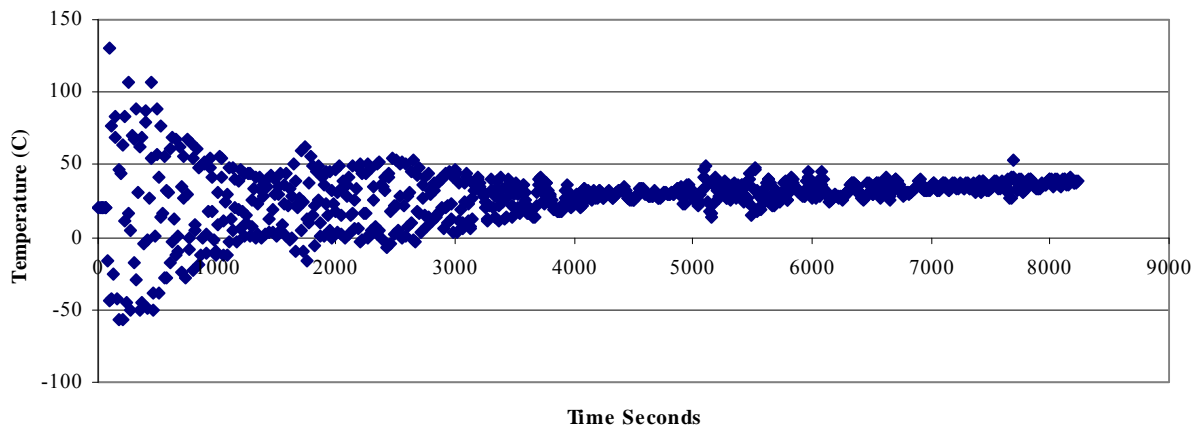
C15. Experiment 5 thermocouple 5 results



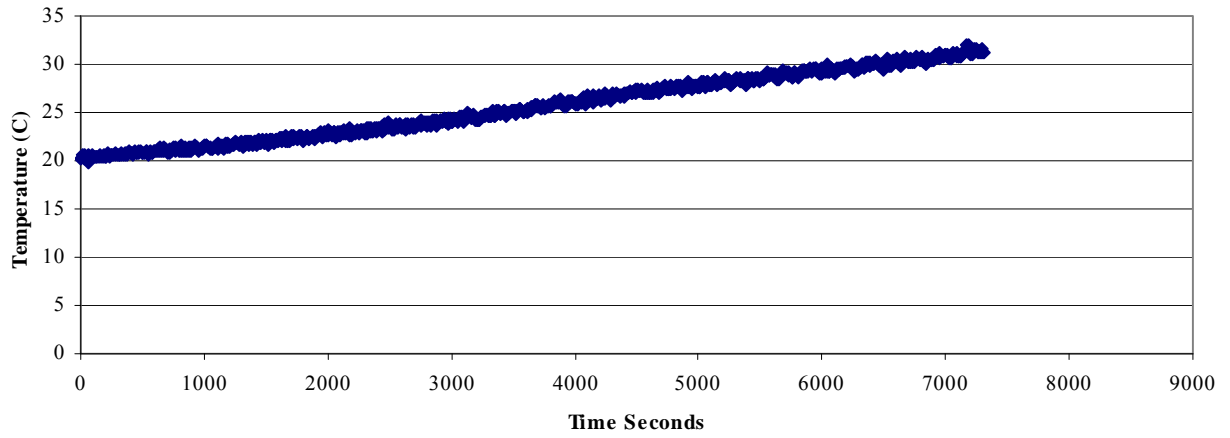
C16. Experiment 6 thermocouple 1 results



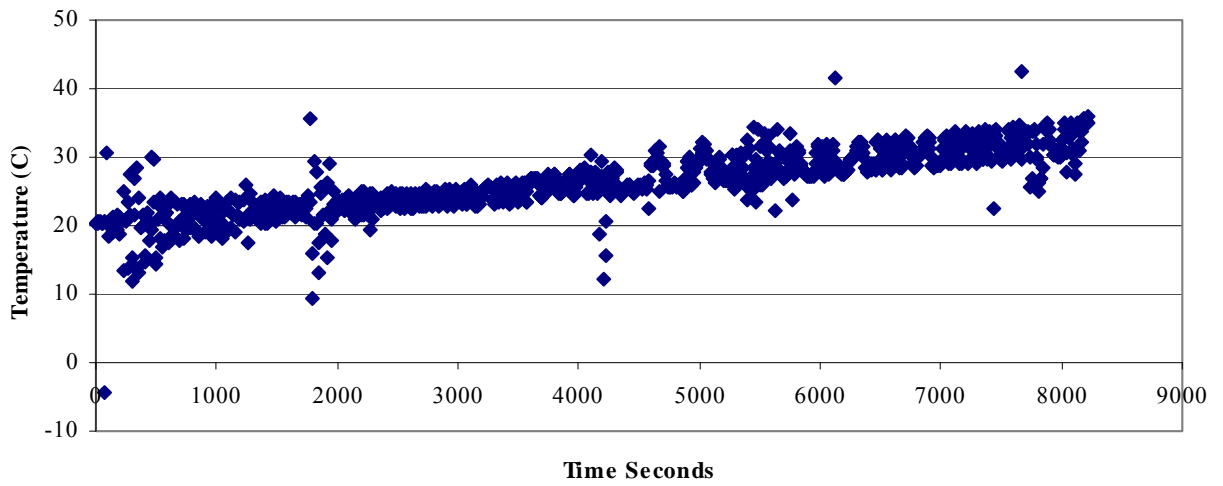
C17. Experiment 6 thermocouple 2 results



C18. Experiment 6 thermocouple 3 results



C19. Experiment 6 thermocouple 4 results



C20. Experiment 6 thermocouple 5 results

References

- Areva-Cerca , 2007, “AREVA-CERCAs Annular can target Rth measurement,” Second RCM of the CRP Bucharest
- Boley, B.A., Weiner, J.H., 1960, *Theory of Thermal Stresses*, Dover Publications Inc., New York, NY, 272 – 281.
- Budynas, R.G., Mischke, C.R., Shigley, J.E., 2004, *Mechanical Engineering Design*, The McGraw Hill companies, New York, NY,
- Incropera, F.P., Dewitt, D.P. 2005, *Fundamentals of Heat and Mass Transfer*, John Wiley & Sons, Singapore
- Madhusudana, C.V., 1998, “Thermal Conductance of Cylindrical Joints,” *International Journal of Heat and Mass Transfer*, **42**, 1273-1287.
- Madhusudana, C.V., 1996, *Thermal Contact Conductance*, Springer, New York, NY, 115 -123.
- Miller, W.H., Professor of Nuclear Engineering, Fall 2008, Columbia, MO (Radiation Safety Course Notes).
- Milosevic, N.D., Raynaud, M., Maglic, K.D., 2003, “Simultaneous Estimation of the Thermal Diffusivity and Thermal Contact Resistance of Thin Solid Films and Coatings Using the Two-Dimensional Flash Method,” *International Journal of Thermophysics*, **24**
- NNSA Office of Global Threat Reduction,
http://nnsa.energy.gov/nuclear_nonproliferation/1550.htm
- Renhart, T, Pa 2004, “Package Requirement Testing”

- Rest, J., Hofman, G.L., Konovalov, I.I., Maslov, A.A., 1998, “Experimental and Calculated Swelling Behavior of U-10 wt.% Mo Under Low Irradiation Temperatures,” <http://www.rertr.anl.gov/Fuels98/JWest-abst.html>
- Solbrekken, G.L., Assistant Professor of Mechanical Engineering, 2008, Columbia, MO (personal communication).
- Solbrekken, G.L., El-Gizawy, S., “Moly-99 Production at MURR: LEU Target Design,” Argonne National lab, **24** April 2008.
- Solbrekken, G. L., El-Gizawy, S., Allen, C., “Engineering design of LEU Foil Based Target for High Volume Production of Moly-99,” International Meeting on Reduced Enrichment for Research and Test Reactors, October 2008
- Sonzogni, A. NNDC: National Nuclear Data Center Chart of Nuclides, <http://www.nndc.bnl.gov/chart/>.
- Ugural, A.C., Fenster, S.K., *Advanced Strength and Applied Elasticity*, Elsevier, New York, NY, 261-293.
- Williams, R.W., 1976, “Technetium-99m Production from Uranium-235 Fission,” Masters Thesis, University of Missouri-Columbia, Columbia, MO.
- Yeoh, G, 2004, “Consideration of u-foil/Aluminium wall gap of 30µm for engineering specification purposes”
- Zolle, Ilse, 2007, *Technetium-99m Pharmaceuticals*, Springer, Berlin Germany, 7-21.